OTTO VON GUERICKE
UNIVERSITÄT
MAGDEBURG

Flow Design Optimization of Blood Pumps Considering Hemolysis

Dissertation
zur Erlangung des akademischen Grades

Doktoringenieur
(Dr.-Ing.)

von **M.Sc Hai Yu**
geb. am 11,Sept,1979 in Harbin, China

genehmigt durch die Fakultät für Verfahrens- und Systemtechnik
der Otto-von-Guericke-Universität Magdeburg

Gutachter:
Prof. Dr.-Ing. Dominique Thévenin
Prof. Dr.-Ing. Kitano Majidi
Prof. Dr.-Ing. Franck Nicoud

Promotionskolloquium am: 01.06.2015

Abstract

Three essential issues concerning the development of optimized blood pumps are investigated in this Thesis: 1) hemolysis models, needed to describe blood damage; 2) a proper approach for numerical simulation of hemodynamics in blood-transporting equipments using Computational Fluid Dynamics (CFD); and 3) CFD-based optimization (CFD-O) of blood pumps.

Hemolysis induced by shear stress is the primary and immediate damage of Red Blood Cells (RBC) and is found in most blood-transporting equipment. A numerical hemolysis prediction based on CFD is needed to support the initial design process and to later reduce the cost of prototype tests. The current state of the art concerning numerical models for hemolysis prediction is reviewed. Existing mathematical models and numerical solutions are discussed are compared concerning their applicability for integration as an objective function for CFD-O. New Eulerian formulations of existing models are introduced and first validations by comparison with experimental data are attempted. A general perspective for future development concerning hemolysis model is finally proposed.

In a second step, the blood flow in a nozzle involving a sudden expansion and an unconventional blood pump are investigated numerically. Both are current benchmarks proposed by the US american Food and Drug Administration (FDA) as part as the assessment program "Critical Path Initiative": based on the results, it will be decided if CFD can be officially involved in later certification steps. The numerical results obtained in our group for the blood nozzle have been already compared with experimental data, showing good agreement. Comparisons for the blood pump will be presented as soon as corresponding experimental data have been released by the FDA (which is unfortunately not yet the case when submitting this Thesis).

A general, CFD-based design optimization method for axial-flow rotary pumps has finally been developed, involving both efficiency and hemolysis as concurrent objectives. This method is first suitable for screw-type, axial-flow rotary pumps with guide-vanes. It has been implemented by coupling the optimization tool ESTECO® modeFRONTIER with the CFD package ANSYS® 14. Concerning the optimization algorithm, a new approach named "design-theory-based CFD-O" is introduced in the present work, which is a combination of design theory and CFD-O. The main purpose of design-theory-based CFD-O is to use pump design theory to reduce the huge computational cost usually associated to CFD-O. Normal optimization based on CFD requires the numerical simulation of hundreds or even thousands of designs, which is and will remain in the near future a major restriction preventing a broad usage of CFD-O. This computational load is tremendously reduced in the current work by 1) reducing the number of geometrical variables through relationships between geometrical/input variables, and by 2) avoiding evaluation of too unconventional designs.

Since it is unclear yet if a screw-type, axial-flow pump is the best technical solution, a different alternative, the Tesla pump, has been finally investigated. It features a mostly laminar flow within the rotor, which is constructed from a group of parallel flat plates. The shear stress in a Tesla-rotor is observed to be fairly low, compared with a standard rotor design. This feature makes the Tesla-pump a good candidate for blood pumps, since low shear stress leads to low hemolysis. However, the major disadvantage of a Tesla pump is its very low efficiency, which will generate high level of thermal heating in blood. In an effort to mitigate this issue, the efficiency of a Tesla pump has been optimized by relying again on a computational model supported by design theory.

Keywords

Computational fluid dynamics (CFD), pump design optimization, axial-flow blood pump, numerical hemolysis prediction, Tesla pump, FDA ”Critical Path Initiative”

Zusammenfassung

Drei wesentliche Fragen für die Optimierung von Blutpumpen werden in dieser Dissertation untersucht: 1) Hämolysen-Modelle werden benötigt, um Blutschädigungen zu beschreiben, 2) eine richtigen Ansatz für die numerische Simulation der Hämodynamik wird auf Basis der Computational Fluid Dynamics (CFD) entwickelt, 3) daraus kann eine CFD-basierte Optimierung (CFD-O) von Blutpumpen durchgeführt werden.

Hämolyse, die durch Schubspannung induziert wird, ist die primäre und unmittelbare Beschädigung der roten Blutkörperchen (Red Blood Cells: RBC) und wird in den meisten Geräten, die Blut fördern, beobachtet. Eine numerische Vorhersage der Hämolyse basierend auf CFD wird benötigt, um den Design-Prozess zu unterstützen und später die Kosten für die Prototypentests zu reduzieren. Der aktuelle Stand der Technik in Bezug auf numerische Modelle zur Vorhersage der Hämolyse wird beschrieben. Bestehende mathematische Modelle und numerische Lösungen werden hinsichtlich ihrer Eignung für die Integration als Zielfunktion für die CFD-O verglichen. Neue Eulersche Formulierungen bestehender Modelle werden vorgestellt und es werden erste Validierungen durch Vergleiche mit experimentellen Daten durchgeführt. Eine allgemeine Perspektive für die künftige Entwicklung der Hämolysenmodelle wird schließlich gezeigt.

Im zweiten Schritt wird die Durchströmung einer Düse mit einer plötzlichen Expansion und eine unkonventionelle Blutpumpe numerisch untersucht. Beide wurden als aktuelle Benchmarks von der US-amerikanischen Food and Drug Administration (FDA) als Teil eines Bewertungsprogramm ("Critical Path Initiative") vorgeschlagen: auf Basis dieser Ergebnisse wird entschieden, ob CFD offiziell in späteren Zertifizierungschritten einbezogen werden kann. Die in unserer Gruppe für die Blutdüse erhaltenen numerischen Ergebnisse wurden bereits mit experimentellen Daten verglichen und zeigen eine gute Übereinstimmung. Der Vergleich der Blutpumpen wird so bald die entsprechenden experimentellen Daten von der FDA veröffentlicht wurden, vorgestellt (leider ist dies noch nicht der Fall bei Fertigstellung der Dissertation).

Ein CFD-basiertes Optimierungsverfahren für Axial-Rotationspumpen wurde dann entwickelt, mit Effizienz und Hämolyse als konkurrierende Ziele. Diese Methode wird zunächst für Schraub-Axial-Rotationspumpen mit Leiträdern verwendet. Hierfür wurde die Kopplung des Optimierungs-Tools ESTECO Modefrontier und dem CFD-Paket ANSYS 14 vorgenommen. In Bezug auf den Optimierungsalgorithmus, wird ein neuer Ansatz mit dem Namen "Design-Theorie-basierten CFD-O" in der vorliegenden Arbeit vorgestellt. Dies besteht aus einer Kombination der Designtheorie mit CFD-O. Der Hauptzweck der Design-Theorie-basierten CFD-O ist es, die Pumpe mit der Designtheorie grob zu gestalten, um den großen Rechenaufwand der CFD-O zu reduzieren. Eine normale Optimierung basierend auf CFD erfordert die numerische Simulation von Hunderten oder sogar Tausenden von Designs, was jetzt und in naher Zukunft eine wesentliche Einschränkung darstellt; so kann keine umfassende Nutzung der CFD-O erfolgen. Diese Rechenlast wird dank Design-Theorie enorm bei den laufenden Arbeiten reduziert, indem 1) die Anzahl der geometrischen Variablen durch Beziehungen zwischen geometrischen Eingangsgrößen reduziert wird, und da 2) zu unkonventioneller Designs gar nicht betrachtet werden.

Da nicht klar ist, ob eine Schraub-Axialpumpe die beste technische Lösung ist, wurde schließlich eine andere Alternative, die Tesla-Pumpe, untersucht. Diese verfügt über eine überwiegend laminare Strömung innerhalb des Rotors, der aus einer Gruppe von parallelen flachen Platten besteht. Die Schubspannung in einer Tesla-Rotor ist ziemlich gering, verglichen mit einem Standard-Rotor. Diese Eigenschaft der Tesla-Pumpe ist für Blutpumpen gut geeignet, da eine geringe Schubspannung zu einer niedrigen Hämolyse führt. Ein großer

Nachteil der Tesla-Pumpe ist jedoch ihr sehr niedriger Wirkungsgrad, sodass eine hohe thermische Erwärmung im Blut erzeugt wird. Es wurde versucht, dieses Problem zu mindern, indem die Effizienz einer Tesla-Pumpe, erneut dank einer Kombination aus Rechenmodell und Design-Theorie, optimiert wurde.

Schlüsselwörter

Computational Fluid Dynamics (CFD), Optimierung des Pumpendesigns, Axial-Blutpumpe, numerische Hämolyse-Vorhersage, Tesla-Pumpe, FDA ”Critical Path Initiative”

Nomenclature

Roman symbols

B	Length of one of the two shorter axis of a deformed RBC, (m)
c_0	Absolute velocity for infinitely long blade ($\text{m}\cdot\text{s}^{-1}$)
$c_{()()}$	Absolute velocity, ($\text{m}\cdot\text{s}^{-1}$)
$c_{A()}$	Axial component of absolute velocity, ($\text{m}\cdot\text{s}^{-1}$)
D	Blade radial external diameter (m)
D_b	Blood damage index
d	Shaft diameter (m)
E	Young's modulus, (Pa)
EI	Red blood cell elongation index
F	Force, (N)
G	Elastic modulus, (Pa)
g	Gravity acceleration, ($\text{m}\cdot\text{s}^{-2}$)
H	Pressure head, in water volume height, (m)
H_b	Hemoglobin in red blood cell
$\triangle H_b/H_b$	Hemolysis as fraction of leaked hemoglobin versus initial total hemoglobin
H_c	Hematocrit (volume concentration of red blood cells)
H_L	Local hemolysis
H_t	Time-step for hemolysis computation
H_{th}	Theoretical pressure head, in water volume height, (m)
h	Thickness of the RBC membrane, (m)
$K_{()}$	Attack angle coefficient
L	Length of the longer axis of a deformed RBC, (m)
l	Impeller axial length, (m)
l_i	Inlet guide vane axial length, (m)
l_o	Outlet guide vane axial length, (m)
$\triangle l_i$	Distance between inlet guide vane and impeller, (m)
$\triangle l_o$	Distance between impeller and outlet guide vane, (m)
n	Rotating speed, (rotation per second)
N_q	Specific speed (same as n)
$\triangle p$	Pressure increase or pump pressure head, (Pa)
Q	Flow rate, ($\text{m}^3\cdot\text{s}^{-1}$)
R	Radius of an undeformed capsule, (m)
S	3×3 Shape/deformation tensor
s	Membrane strain, (s^{-1})
t	Time, (s)
t_c	RBC membrane relaxation time, (s)
$u_{()()}$	Circumferential velocity at impeller inlet, ($\text{m}\cdot\text{s}^{-1}$)
v	Velocity, ($\text{m}\cdot\text{s}^{-1}$)

V	Domain volume, (m^3)
$w_{()_{()}}$	Relative velocity, ($\mathrm{m}\cdot\mathrm{s}^{-1}$)
X	Position, (m)
x	Distance, (m)
Y	Potential energy, $Y = gH$, ($\mathrm{m}^2\cdot\mathrm{s}^{-2}$)
Y_{th}	Theoretical potential energy, $Y_\infty = gH_\infty$, ($\mathrm{m}^2\cdot\mathrm{s}^{-2}$)
z	Number of blades of impeller
z_i	Number of blades of inlet guide vane
z_o	Number of blades of outlet guide vane

Greek symbols

$\alpha_{()_{()}}$	Velocity angle, (°)
$\beta_{()_{()}}$	Blade angle, (°)
$\dot{\gamma}$	Shear rate, (s^{-1})
δ	Blade thickness, (m)
ϵ	Velocity gradient (or deformation) tensor, (s^{-1})
η	Efficiency, (s^{-1})
η_i	Input efficiency for optimization
λ	Relaxation time, (s)
μ	Dynamic viscosity, (Pa·s)
μ_0	Dynamic viscosity at zero shear rate, (Pa·s)
μ_{in}	Dynamic viscosity inner RBC, (Pa·s)
μ_∞	Dynamic viscosity at infinity shear rate, (Pa·s)
μ_{mb}	Dynamic viscosity of RBC membrane, (Pa·s)
ξ	Blade top clearance (non-dimensional)
τ	Shear stress, (Pa)
$\bar{\tau}$	Mean comparative shear stress, (Pa)
τ_s	Threshold of shear stress, beyond which hemolysis occurs, (Pa)
τ_{st}	Steady shear stress, (Pa)
τ_y	Yield stress, (Pa)
Ω	Velocity gradient tensor, (s^{-1})
$\psi_{()_{()}}$	Squeeze coefficient

Indices for positions within pump

$()_{()_n}$	at shaft
$()_{()_m}$	at blade middle
$()_{()_x}$	at blade top
$()_{-2_{()}}$	at inlet guide inlet
$()_{-1_{()}}$	at inlet guide outlet
$()_{1_{()}}$	at impeller inlet
$()_{2_{()}}$	at impeller outlet
$()_{4_{()}}$	at outlet guide inlet
$()_{5_{()}}$	at outlet guide outlet

Eulerian specification: all flow quantities are depicted as a function of position x and time t, for instance for velocity

$$v(x,t).$$

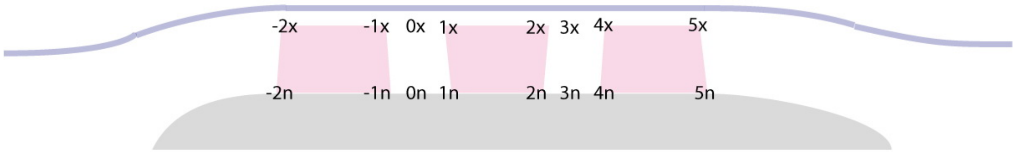

Figure 1: Index convention showing the positions within a screw-type axial-flow pump

Lagrangian specification: individual fluid parcels are followed through time. The fluid parcels are labeled by some (time-independent) vector field **a**, for instance the initial position of the fluid parcel. All flow properties are then described as a function of position of the parcel labeled **a** and time t:

$$X(a, t).$$

The relation between Lagrangian specification and Eulerian specification is:

$$v(X(a, t), t) = \frac{\partial X}{\partial t}(a, t).$$

Contents

Chapter 1

Introduction and Basic Concepts

1.1 Ventricular Assist Device

A ventricular assist device (VAD) is a mechanical support, attached to the native heart and vessels in order to assist the cardiac function of patients with heart failure (Fig. 1.1). VADs include left ventricular assist devices (LVAD, the most common solution in practice), right ventricular assist devices (RVAD), bi-ventricular assist devices (bi-VAD) and external ventricular assist devices. A blood pump (for bi-VAD, there can be more than one) plays the key role in all VAD systems.

1.1.1 Present Market Situation

In developed countries, around 2% of adults suffer from heart failure. Today, 60% of heart transplantations are urgent cases, for which donor hearts are difficult to find. VADs are used in such situations as a bridge to transplantation and/or during patient transport. The yearly number of patients receiving long-term VAD implantation is about 1700 in the United States and 430 in Europe (statistics from year 2010) [1]. In year 2009, for all the implantations with FDA-approved devices, around half of those involved pulsatile devices, the other half continuous flow devices (rotary blood pumps) as considered in the present work [2]. The total market for VADs was roughly $500 million in year 2010, and is expected to double until year 2017 [3].

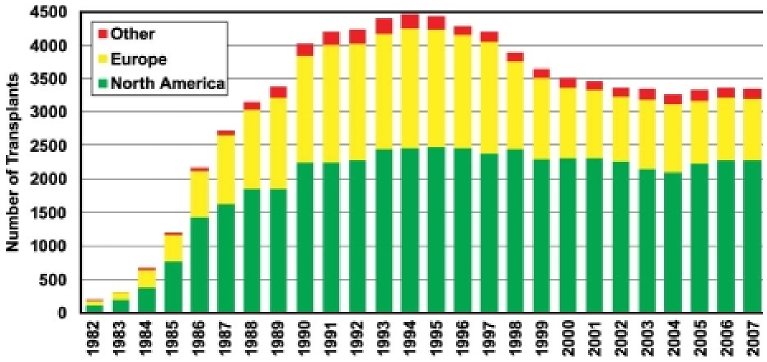

Figure 1.1: Number of heart transplants per year [1].

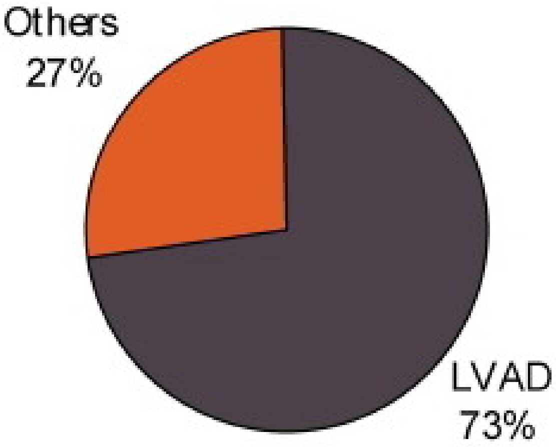

Figure 1.2: LVAD contribution in 2010 [3].

1.1.2 Types of Blood Pumps for LVADs

Different types of VADs have been developed and a large amount of research has been devoted to improve the material, structure and control strategy of these devices.

Based on the blood flow produced by the assist devices, ventricular assist devices can be classified as pulsatile assist devices and nonpulsatile assist devices. Since the flow pumped by a natural heart is pulsatile, it was first assumed that pulsatile assistance is preferred. However, clinical evidences are not conclusive at all. Long-term nonpulsatile bi-ventricular bypass is reported to produce no harmful physiological effects in animals, and nonpulsatile assist devices can function as well as pulsatile assist devices, even if 20% higher blood flow rates are pumped [4]. There is also evidence that pulsatile cardiopulmonary bypass procedure has no significant advantage compared to nonpulsatile procedures in terms of hemolysis and deformation of RBCs [5]. Even if prolonged nonpulsatile left ventricular bypass may impact arterial wall structure and vasoconstrictive function [6], nonpulsatile systems are still broadly used up to now and become even increasingly popular (Fig. 1.2).

One main reason is that, structurally, devices needed to produce a proper pulsatile flow are relatively large in size and have large contact surfaces to blood. Nonpulsatile ventricular assist devices are usually rotary blood pumps, which are smaller and simpler, and have less contact surface. Since a quite constant shear stress is produced in rotary blood pumps, a lower hemolysis level may be achieved for appropriate designs. This is the reason why this Thesis concentrates on nonpulsatile (rotary) blood pumps.

1.1.3 Surgery Issues

Typically, a pulsatile LVAD is large, and is placed outside of the body. It is connected to left atrium and left ventricle by pipes through the belly skin (as in Fig. 1.3, left). Some smaller systems can now be implanted inside the abdomen, but there is no approved commercial system available for in-chest implantation.

On the other hand, available nonpulsatile LVADs can be implanted inside the chest (as in Fig. 1.3, middle), or even inside the left atrium (as in Fig. 1.3, right), if its size is small enough. Until 2011, all existing VAD models on the market were implanted through median sternotomy, for which a vertical inline incision is made along the sternum, after which the sternum itself is divided. Future, even smaller VADs could possibly be implanted by minimally-invasive surgery, hugely reducing the complexity of the intervention.

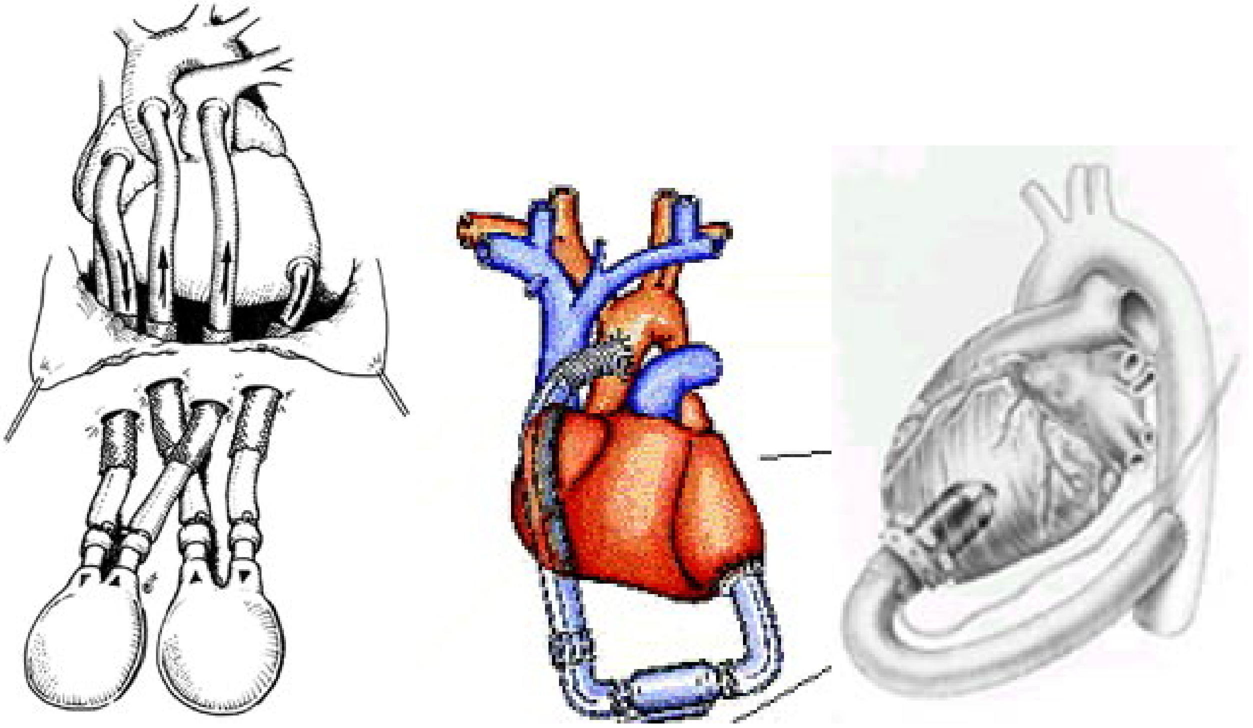

Figure 1.3: Left: Extracorporeal implantation (Berlin Heart®Excor); Center: In-chest implantation (Berlin Heart®Incor); Right: In-heart implantation: Jarvik®2000.

1.1.4 Working Condition for Rotary Blood Pumps

Corresponding to physiological constraints, most rotary blood pumps operate at a flow rate around 5 L/min, against a pressure of around 100 mmHg, with a rotating speed from 2 000 to 20 000 rpm. The hydraulic efficiency of such pump varies strongly depending on the employed design. The maximal hydraulic efficiency claimed in the literature exceeds 80%, but other systems have been associated with efficiencies below 50%. These values must be considered with caution, since independent studies are the exception, most figures being directly or indirectly provided by the company selling the corresponding pump. Obviously, a lower efficiency implies that more heat will be generated due to power loss, which could lead to negative effects concerning in-body implantation and blood damage. In that sense, the efficiency should – as usual – be maximized, but without forgetting that hemolysis is of paramount importance: increasing the efficiency by 2% makes no sense if the hemolysis is simultaneously doubled.

1.1.5 Rotary Blood Pump with Magnetic Levitation System

The third generation of rotary blood pumps is characterized by its magnetic levitation system. In such a pump, the rotor of the driving electric motor is integrated into the impeller of the pump, and the stator is integrated into the pump shell. In that way, the pump and the driving electric motor are constructed in the same block. Permanent magnet elements are assembled inside the impeller, the coils of the stator of the electric motor are assembled either in the pump shell or in the shaft of the guide blade (as in Fig. 1.4).

In a blood pump with magnetic levitation system, the impeller floats in blood. It is not driven by a transmission rod, and has no physical connection or contact with the fixed parts; thus, no bearing is needed. Mechanical friction and friction-induced efficiency losses are therefore minimized. Since mechanical friction regions are typically of major importance for hemolysis, removing such regions helps to minimize the total hemolysis. Current magnet-levitated blood pumps include two groups of magnetic coupling, for instance for the Berlin Heart Incor, Fig. 1.4. One group is inside the shafts of the guide vanes and at the front and back side of the impeller; it is used to levitate the impeller in the middle position of the pump. The other group is the stator and the rotor magnet; it serves to rotate the impeller by the magnetic flux between the two components of the group.

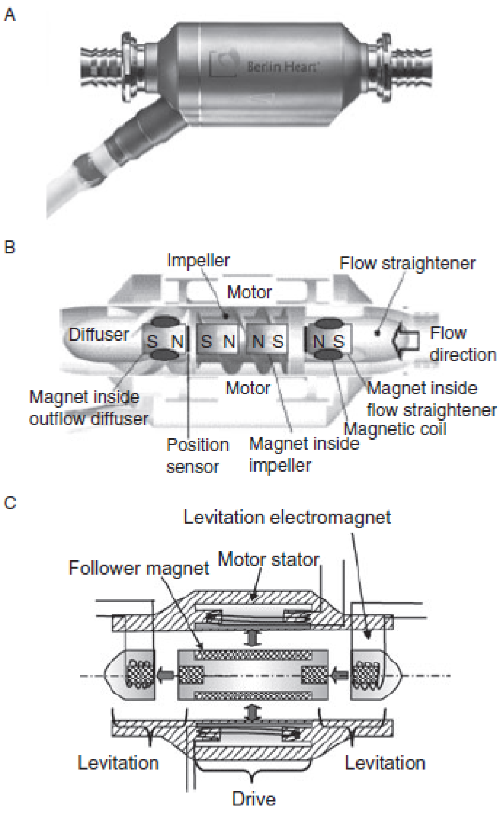

Figure 1.4: Berlin Heart®Incor [7].

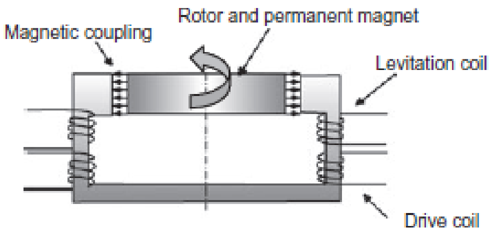

Figure 1.5: Levitation system with single magnetic coupling [7].

The magnetic coupling for levitation and the magnetic coupling for driving can also be integrated together, in order to further simplify the mechanical structure of the pump. Figure 1.5 is an example of such a solution.

1.1.6 Tesla Pump as Blood Pump

A Tesla pump is a very unconventional design [8]. There, the rotor is composed of parallel co-rotating disks. These disks are flat, thin and smooth and are spaced along the shaft with tiny gaps. The distance between disks can be determined approximately by calculating the thickness of the boundary layer of the fluid, normal to the disk surface. Friction forces between disks and liquid and within the liquid are the transportation driving force.

Compared with typical pumps involving rotor and blades, a Tesla pump shows a very low average flow-induced shear stress, which is the main cause of hemolysis. Therefore, using a Tesla pump as blood transport equipment could greatly reduce occurrence of hemolysis. This is why some scientific publications and patents exist concerning the practical usage of Tesla pumps for blood flows [9].

On the other hand, a typical Tesla pump has a very low efficiency (usually less than 20 %), which would generate massive heat transfer to the blood, which might be a problem for blood damage and patient health.

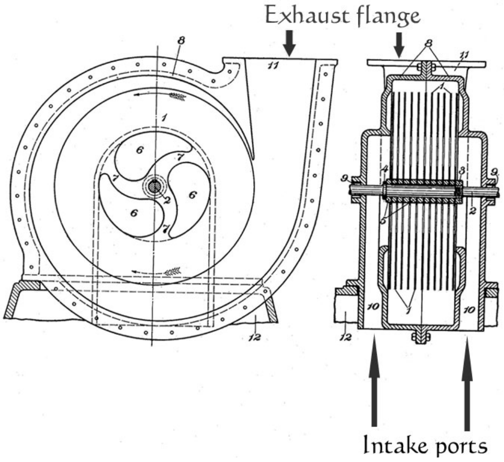

Figure 1.6: A typical Tesla pump [8]

Due to its possible practical relevance, and considering that our research group is very experienced concerning the optimization of hydraulic efficiency for turbomachines, a specific subproject has been considered during this Thesis. The suitability of a Tesla pump as a blood pump is discussed in Chapter 6. A CFD-based design optimization for the rotating disks of a Tesla-pump is discussed, and currently considered in more details in [10].

1.2 Numerical Hemolysis Prediction

Hemolysis and Thrombosis are the two major complications associated with blood pump applications. Hemolysis is the damage of red blood cells (RBCs) and the release of their content (hemoglobin) into the surrounding fluid (blood plasma). Reducing the hemolysis would result in a lower need of potentially harmful anti-hemolysis agents. It would open the door for the development of new generation VAD devices [11]. At the difference of thrombosis, hemolysis does not lead to accumulated substance on the wall of the arteries. It does not lead to a change in geometry and is thus easier to be considered in a CFD approach. Additionally, the time-scale of damages induced by hemolysis is much shorter than for thrombosis. This is why only hemolysis is considered in the present work; it is already a considerable challenge, as will be discussed later.

A simple relation between hemolysis, magnitude of shear stress and exposure time was first introduced by [12] in 1990:

$$\triangle H_b/H_b = 3.63\,10^7 \tau^{2.416} t^{0.785} \tag{1.1}$$

with $\triangle H_b/H_b$ referring to released hemoglobin in percentage, τ referring to shear stress and t referring to exposure time. This relationship was worked out by curve fitting, and is based on experimental data with constant shear stress. It was later interpreted in different numerical ways, coded in different CFD tools, and is still widely used. However, in real flows found in blood transportation equipments, the precision of this model can be very poor, results being one or two orders of magnitude different from measured values [13]...The success of this model is mostly due to its simplicity of coding, and partly due to shortcomings of other alternatives.

More complex mathematical models are also available. Some do deliver a better precision for certain applications [13], but usually only with limited generality. The difficulty for identifying new mathematical models lies in the overwhelming complexity and versatility of the hemolysis process. All existing hemolysis models are based on macroscopic blood properties; the equations are designed based upon strong assumptions, and the parameter values are fitted to experiments results. Modeling and simulation of individual RBCs would lead to unacceptable computational costs and cannot therefore be included for industrial CFD-based equipment design yet.

There are two major approaches for the numerical implementation of hemolysis models, for instance Eq.(1.1): the particle tracking (Lagrangian) approach (during post-processing), and the in-solver, additional transport equation (Eulerian approach). The former has a broad applicability, but the precision is usually limited by the imprecision in particle track and averaging, especially when there are large recirculation regions in the flow domain. The latter is only valid for a certain type of hemolysis models, but is faster and in principle more accurate [11]. It is easier to integrate into an automatic design optimization process.

A detailed discussion of numerical hemolysis prediction methods is given in Chapter 2.

1.3 CFD-Based Pump Design Optimization

1.3.1 About CFD-O

Instead of the trial-and-error manual method aiming at regional improvement, CFD-O (Optimization relying on evaluations obtained by Computational Fluid Dynamics, or CFD-based Optimization [14, 15]), means a mathematical optimization: an automatic process, revealing the relationship among all important parameters affecting the performance of a design.

A fully automatic optimization employs a shell program for the generation of design variables' value, the flow-path control, and the evaluation of the performance of the designs. In the flow-path, geometry and mesh generators, CFD solver, and pre- and post-processing tools are integrated. The integrated CFD-tools are executed in sequence based on journal (also called replay) scripts, and thus the optimization procedure is automatic without need for further human interference. The shell program repeats this sequence running in a loop, determines the value(s) of the objective(s), and ranks each design based on these objective values (Fig. 1.7).

The iterations within the optimizer loop are sorted into groups (or "generations"). Evolutionary algorithms (EA) are typically used for the production of variable values for generations, producing and evaluating one generation at a time. The newer generation is designed by evaluating the outcomes (objective values) of the earlier generations.

Genetic algorithm is the most popular type of EA (Fig. 1.8). With such an algorithm, the initial population is a set of quasi-random configurations in the domain defined by the limits imposed on the parameters. The creation of a new generation from the present one is performed by applying genetic operators to the individuals of the present generation. At each generation, the individuals are classified as a function of their corresponding objective values, leading to a rank within the population and finally to a fitness. The probability for an individual to participate in the reproduction process is determined by a probability based on its fitness value. Individuals associated with a higher fitness value have a better chance to survive and to take part in the reproduction process. In this way, better and better generations are generated step by step. The advantages of GA are a remarkable robustness, a good potential to explore the whole space and to avoid getting trapped in local optima. GA can iterate further even if some evaluations fail, and that is often the case for pump optimization, since many designs will fail to produce a certain pressure head. The disadvantage of GA lies in its large computational cost [15].

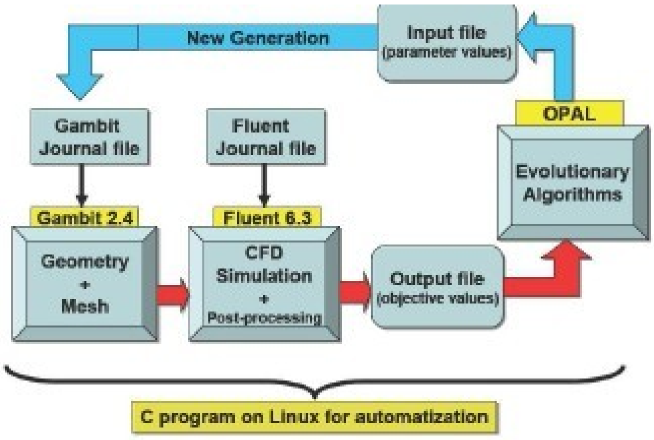

Figure 1.7: A sample optimization loop [16].

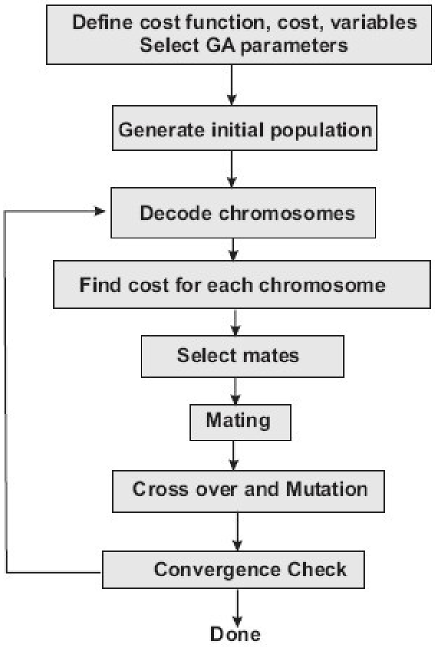

Figure 1.8: Flowchart of a genetic algorithm [16].

1.3.2 CFD-O of Axial-flow Blood Pump

The design objectives of a blood pump usually include the following aspects:

1. Higher efficiency.
2. Smaller size.
3. Lower hemolysis.
4. Lower coagulation (thrombosis).

Efficiency is typically considered as the basic and primary objective of pump optimization; a pump system with higher hydraulic efficiency consumes less power, has usually less total weight, and will lead to reduced heat fluxes. Pump size is a critical consideration for selecting the surgery method; pump size could be easily included as a secondary objective in CFD-O, since no extra computational cost has to be added; the corresponding objective is directly an arithmetic result of some of the geometrical variables. Nevertheless, it is not done in the present, purely theoretical project, since surgery is not considered. On the other hand, hemolysis, being of central importance, can be added as a secondary objective during the optimization. Thrombosis is not included in the current work, for the reasons discussed previously.

The main difficulty associated to the direct optimization of a 3-dimensional complex geometry with an unsteady flow lies in the vast computational cost associated to this problem. This has never been done previously in our group: either a 3-dimensional optimization problem was simplified into a 2-dimensional problem, such as for the wind turbines in [16]; or only steady flow conditions where considered. However, the current problem can neither be simplified to 2D nor to steady conditions.

The total time of an optimization equals in principle the evaluation time for one design times the total number of designs to be evaluated. The vast computational cost for a 3D pump optimization partly lies on the long duration for each CFD simulation of one pump design. A typical hexahedral mesh for an axial-flow pump with front and back guide-vanes possesses half a million cells, using periodical interfaces to reduce the mesh size by omitting duplicate parts (axial-symmetry). A CFD simulation for such a mesh takes typically 5 hours on a good desktop machine with an Intel®core-i5 quad-core processor. Additionally, the simulation needs to be repeated with different rotating speeds, in order to find out the right rotating speed to reach the target pressure head.

The vast computational cost lies also partly on the large number of designs to be evaluated. The number of total designs in an optimization increases with the number of design (input) variables. And the geometrical parameterization of an axial-flow blood pump requires a very large number of geometrical variables.

In Chapter 4, an innovative method with the name of "design-theory-based CFD-O" (DTB-CFD-O) is introduced for the first time. It combines the advantages of pump design theory and CFD-O, and is able to significantly reduce the total number of designs to be evaluated, compared with standard CFD-O. Design theory is used to reveal the relationship between geometrical variables; when the values of geometrical variables change in a correlated manner, the variables' variation domain can be reduced. If some geometrical variables can be expressed by a definite mathematical expression as function of other variables, the number of input variables can be immediately reduced, In this way, the total computational cost of the optimization can be significantly reduced. In our optimization, the geometrical variables are divided into two groups: the controlling group and the derived group. Only values for the first group are decided by the optimizer, the values of the derived group being determined by the pump design theory; thus, a full geometrical description is realized by using only a limited number of input variables.

1.4 Structure of the Thesis

This dissertation begins with a general review of current knowledge concerning blood, followed by a detailed review of the current state of the art for numerical hemolysis prediction methods. Different approaches for hemolysis prediction are compared and validated by comparison with the (unfortunately very limited) experimental data available. These models are then used for the numerical hemolysis prediction in the rest of this work.

The second part of the dissertation is a typical "passive" CFD, used as a validation of the developed computational chain. It involves the numerical simulation of the blood flow in two existing equipments: a nozzle with sudden expansion and a centrifugal pump, both considered in the FDA's "Critical Path Initiative" project. These test cases were selected to find out how accurately can CFD predict the blood flow in medical equipments with complex geometries, and to test the possibility of numerical hemolysis prediction. Our numerical results for the first test case have been successfully validated by comparison with experimental data. In particular, the impact of the turbulence models has been compared. The numerical results for the second test case are obtained with an hexahedral mesh involving around 10 million cells. Unfortunately, reference experimental data are not available yet for comparison.

The dissertation turns in the third part to an "active" usage of CFD: CFD-aided design. A design method for turbomachinery combining the merits of traditional pump design theory and modern computer-aided design process with CFD is introduced. A Matlab-based solution of the equations is integrated into the automatic CFD-O loop. A detailed theoretical derivation and practical numerical tools are described in this part.

In the fourth part, an alternative design for blood pump, a Tesla pump, is discussed. The main objective here is to increase the efficiency of the Tesla pump. First results are encouraging, but further investigations are required concerning this point.

Chapter 2

Numerical Hemolysis Prediction

2.1 Literature Review on Blood and RBC Properties

Human blood is a suspension of red blood cells (RBCs), white blood cells (WBCs) and platelets in plasma. Blood shows a complex behavior, including shear-thinning viscosity and cell damage. These phenomena are due to the intricate biological nature and physiological function of blood.

2.1.1 RBC

RBCs (Fig. 2.1) constitute 40% (women) or 45% (men) of blood by volume. The inner content of RBCs (90% is hemoglobin) is a Newtonian fluid with a viscosity of $6.5\,10^{-3}$ Pa·s [17]. Some key features of human RBCs are [13]:

- A RBC has 40% excess surface compared to a sphere of the same volume. This is attributed to its biconcave-disk shape (Fig. 2.2). This excess surface area allows the RBC to undergo area- and volume-preserving deformations, and increases the surface area available for the gases to diffuse across the semipermeable membrane;
- The viscoelastic membrane of a RBC can accommodate a maximal stretching of 6% [17]. The membrane starts to rupture beyond this limit. Hemolysis starts after the protruded surface (see later Figs. 2.17 to 2.19) occupies about 29% of the total surface area, i.e., a lesion area of 27±6 μm^2, based on an initial total surface of 140 μm^2 [18];
- The natural half-lifetime of RBCs is 120 days. When submitted to shear, young RBCs have a relaxation time of about 100 ms, old RBCs have a relaxation time tending to 300 ms.

Figure 2.1: Natural shape of RBC for zero shear

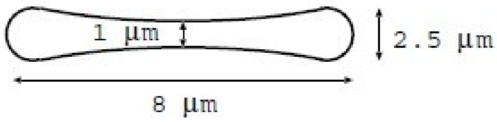

Figure 2.2: Typical dimensions of RBC [13]

2.1.2 Blood Viscosity

Blood is a shear-thinning (or viscoelastic) non-Newtonian fluid. The suspending medium (plasma) is a Newtonian fluid (viscosity of $1.1\,10^{-3}$ to $1.3\,10^{-3}$ Pa·s) [19]; its viscosity is independent from the rate of strain in the flow. The viscoelastic behavior of blood is due to the complex mechanical response of blood cells in interaction with the plasma. At zero or very low shear, RBCs aggregate into coin-stack structures; as shear increases, this coin-stack structure breaks; and at higher shear, RBCs start to deform and their orientation change. This stage-by-stage modifications of RBCs lead to the shear-thinning behavior of blood; i.e., the viscosity of blood decreases as the rate of strain in the flow increases [13]. Among many others, Thurston has introduced an equation for the relationship between shear stress and velocity gradient in blood [20]. For low velocity gradients, a constant viscosity is used:

$$\tau_{st}^{1/2} = \tau_y^{1/2} + \left(\mu \frac{\partial v}{\partial x}\right)^{1/2} \tag{2.1}$$

where τ_{st} is the flow shear stress, $\partial v / \partial x$ is the corresponding value of the velocity gradient, μ is dynamic viscosity and τ_y is the yield stress. This equation shows that blood can sustain a static stress without flowing, as long as it is below the yield stress. However, reported values of τ_y are quite low. This first relationship between stress and velocity gradient is only valid for small velocity gradients, as long as RBCs are unperturbed and remain in the fully aggregated state. With increasing velocity gradients the structures become disrupted, at which level shear-thinning appears [20].

Measured shear-dependent viscosity data for a human blood sampled with 45% hematocrit is shown in Table 2.1 [21]:

Shear rate (s^{-1})	0.01	0.06	0.12	0.53	5.99	58.1	11.4	118	230
Viscosity (mPa·s)	158	99.7	74.3	36.2	11.2	8.62	5.44	4.61	4.04

Table 2.1: Measured shear-dependent viscosity of human blood [21]

Leuprecht and Perktold used the Carreau-Yasuda model (Eq. 2.2) to model blood behavior in a stenosed artery [22]:

$$\mu(\dot{\gamma}) = \mu_\infty + \frac{\mu_0 - \mu_\infty}{(1 + (\lambda\dot{\gamma})^b)^a} \tag{2.2}$$

where $\mu_0 = 1.6\,10^{-1}$ Pa·s, $\mu_\infty = 3.5$ mPa·s, $a = 1.23$, $b = 0.64$, $\lambda = 8.2$ s.

The hematocrit level, the volume fraction of RBCs in blood, influences the viscosity of blood. Oldroyd considered the suspension behavior of spherical drops that are surrounded by a film with viscoelastic behavior, and gave the relationship between hematocrit and viscosity as [23, 24]:

$$\frac{\mu_{susp}}{\mu_0} = 1 + KH_c \frac{(\mu_i + \mu_m)/\mu_0 + 0.4}{(\mu_i + \mu_m)/\mu_0 + 0.6} \tag{2.3}$$

where μ_0 is the viscosity of the continuous phase, μ_i is the viscosity of the dispersed phase, μ_m is a function of the rheological properties of the membrane and H_c is the volume concentration of the spherical drops.

However, as done in almost all published CFD studies concerning blood pumps, a constant viscosity (Newtonian model) will be employed in the rest of this Thesis. For this specific application, only small differences are expected when using a more realistic, non-Newtonian description.

2.1.3 RBCs' Elongation, Tank-treading and Tumbling

The behavior of RBCs in a shear flow is characterized by elongation, tank-treading and tumbling. When blood is at rest, the RBCs aggregate into coin-stack-shaped structures (also called rouleaux); these structures break as the shear stress in blood increases, and RBCs become individually dispersed. In the flow the RBCs behave as neutrally buoyant droplets with high deformability but small areal stretchability [25, 26]. Schmid-Schoenbein and Wells found that the dispersed RBCs preserve their biconcave shape and tumble in a flow for a shear stress below 0.1 Pa [25]. The tumbling gradually reduces and the cells begin to align with the flow around 0.2 Pa (Fig. 2.3). The RBCs deform into ellipsoidal shape, orient with the flow and show tank-treading of membrane at shear stress larger than 1 Pa. Tank-treading is a phenomenon in which the cell membrane rotates around the encapsulated fluid [13].

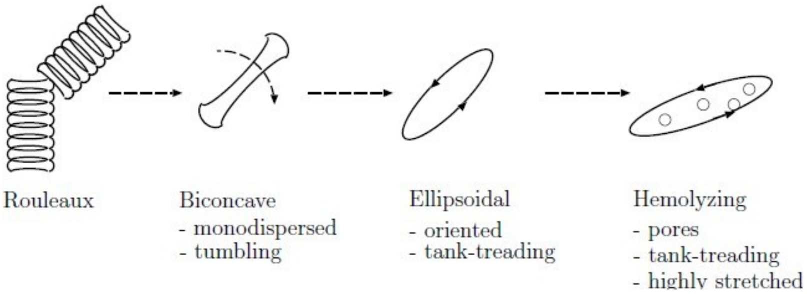

Figure 2.3: Qualitative RBC behavior as shear increases [13]

2.1.3.1 Steady-state Investigations on Elongation

The Elongation Index EI is used to measure the elongation of a microcapsule or a RBC:

$$EI = \frac{L - B}{L + B} \tag{2.4}$$

where L is the longer axis of the RBC and B is one shorter axis of the (ellipsoidal) RBC. The elongation of an initially spherical microcapsule in linear shear flow can be described by the ratio of deforming and restoring forces, as in Eq.(2.5) [27]:

$$EI \approx \frac{25\mu\dot{\gamma}R}{4Eh} \tag{2.5}$$

where μ is the viscous resistance of the solvent phase, $\dot{\gamma}$ is the applied shear rate, R is the radius of the undeformed capsule, E is the bulk Young's modulus and h is the thickness of the membrane.

Bronkhorst studied experimentally the relation between RBC rheology and the various stages of the deformation curve with blood flow in a stationary cylinder. His results are shown in Fig. 2.4 [28].

The Lineweaver-Burke method gives a relation between shear stress τ and EI [29]:

$$\frac{1}{EI} = \frac{\tau_{1/2}}{EI_{max}}\frac{1}{\tau} + \frac{1}{EI_{max}} \tag{2.6}$$

where $\tau_{1/2}$ is the shear stress that causes half-maximal RBC deformation $EI_{max}/2$. In this method $1/EI$ is first plotted against $1/\tau$. Then, the relationship is described with a linear regression (as in Fig. 2.5). However, this reciprocal plot deviates from a straight line. The

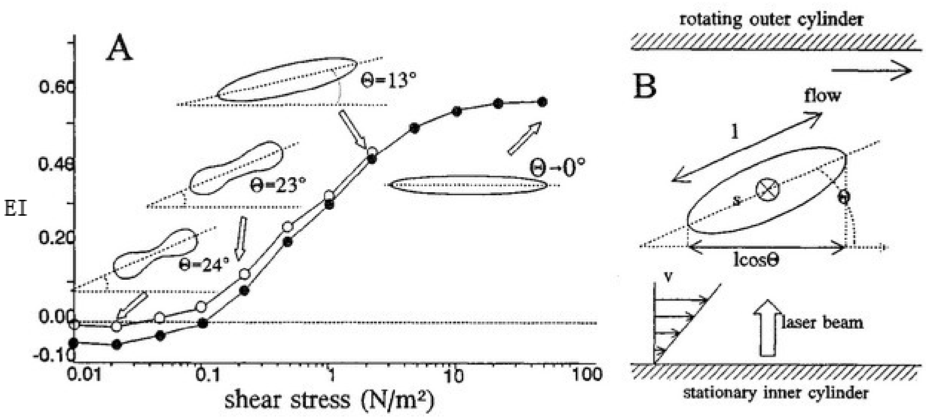

Figure 2.4: RBC deformation in shear flow [28]

least squares method used for regression minimizes the absolute difference between the measurement points and the fitted line. The difference causes merely a small relative difference at high $1/\tau$ and high $1/EI$, but causes a huge relative difference at low values of $1/\tau$ and $1/EI$ [30].

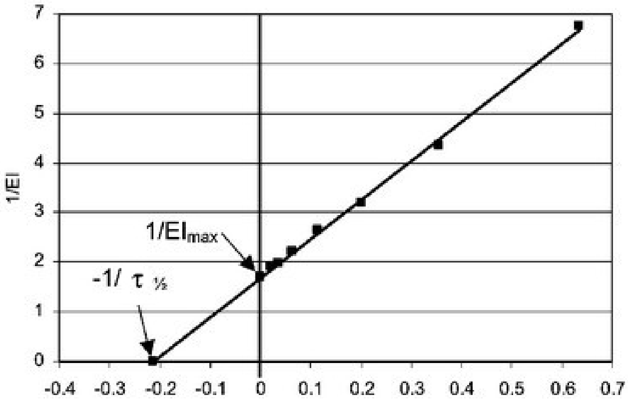

Figure 2.5: Lineweaver-Burke transformation showing $1/EI$ vs. $1/\tau$ [31]

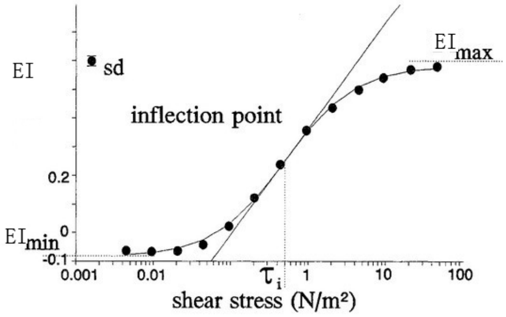

Figure 2.6: Streekstra-Bronkhorst transformation showing τ vs. EI [28]

The Streekstra-Bronkhorst model (Eq. 2.7), on the other hand, is based on a S-shaped curve. For this purpose, the shear stress in plotted on a logarithmic scale (see Fig. 2.4) [28],

$$EI = (EI_{max} - EI_{min}) \frac{\left(\frac{\tau}{\tau_{1/2}}\right)^m}{\left(\frac{\tau}{\tau_{1/2}}\right)^m + 1} + EI_{min} \tag{2.7}$$

where, m is a constant. In order to remove the variable EI_{min} in Eq. (2.7), an approximate form has been proposed in [32]:

$$EI = EI_{max} \frac{\left(\frac{\tau}{\tau_{1/2}}\right)^m}{\left(\frac{\tau}{\tau_{1/2}}\right)^m + 1} \tag{2.8}$$

Ookawara measured the influence of temperature on plasma viscosity (Fig. 2.7) and RBCs' EI (Fig. 2.8) [33]. Result shows that the kinetic heating in artificial blood devices – somewhat surprisingly – tends to reduce hemolysis. This partly explains why many numerical hemolysis models over-predict hemolysis in commercial blood pumps. However, it is still unclear why this phenomenon is observed; to what extent kinetic heating impacts hemolysis prediction still has to be clarified.

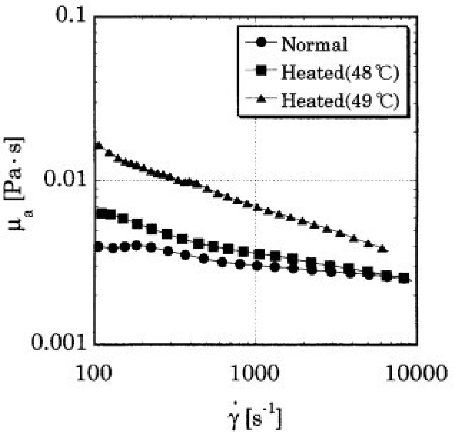

Figure 2.7: Dependence of plasma viscosity on temperature [33]

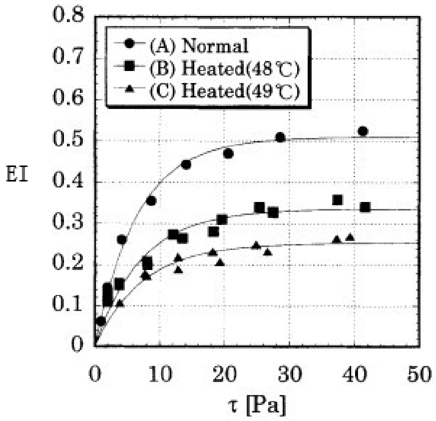

Figure 2.8: Dependence of RBCs' EI on temperature [33]

2.1.3.2 Transient Investigations on Elongation

The investigations on the relation between τ and EI in Section 2.1.3.1 are all based on measurements with time-constant shear stress. However, the deformation of RBCs is a time-dependent process; a time delay exists between a rise in shear stress and the time at which RBCs reach steady-state of EI .

Watanabe measured the deformation of RBCs under oscillation of shear stress. The first experiment is at a frequency of 3 Hz and a peak shear stress of 220 Pa (Fig. 2.9) [34]. The second experiment is at a frequency of 2 Hz, a peak of shear stress of 128 Pa, and with shear stress pre-loading of 64 Pa (Fig. 2.10) [35]. A clear time delay between the minimum value of shear stress and the minimum value of deformation is observed. However, a time delay between the peak value of shear stress and the peak value of deformation is not obvious.

Maffettone and Minale used a tensor-based ellipsoidal drop model to portray the behavior of RBC under transient shear stress. Equation (2.9) is the original formation for a simple deformable ellipsoidal drop [36]:

$$\frac{dS}{dt} - a[\Omega \cdot S + S \cdot \Omega] = -f_1[S - g(S)I] + af_2[\epsilon \cdot S + S \cdot \epsilon] \tag{2.9}$$

Arora later modified this equation with additional consideration for membrane tank-treading effect, dsee etails in Section 2.3.3.1.

Hochmuth introduced an exponential function for the relaxation of RBC after cessation of stress [37]:

$$\frac{EI(1 + EI_{max}^2)}{(1 + EI^2)EI_{max}} = \exp\left(-\frac{t}{t_c}\right) \tag{2.10}$$

where t_c is the characteristic time of relaxation.

In addition, Yoon's measurements for single RBC under stretching force shows a power-law decay of the stress in time (Eq. 2.11) [38]:

$$F(t)/\triangle L(t) = k(t) = k_\infty + \triangle k_0(t/t_0)^{-\alpha} \tag{2.11}$$

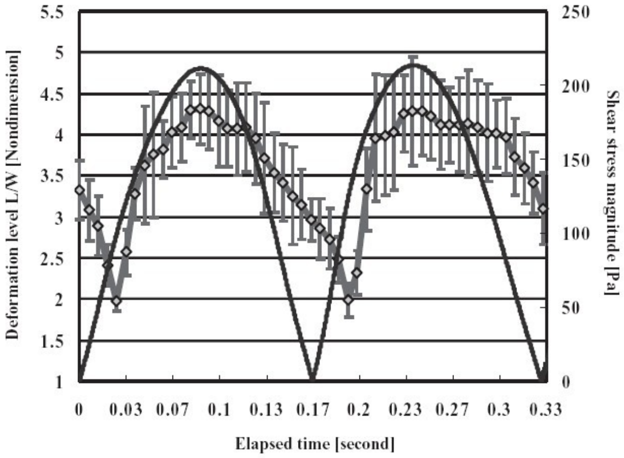

Figure 2.9: L/B of porcine blood under oscillation of shear stress [34]

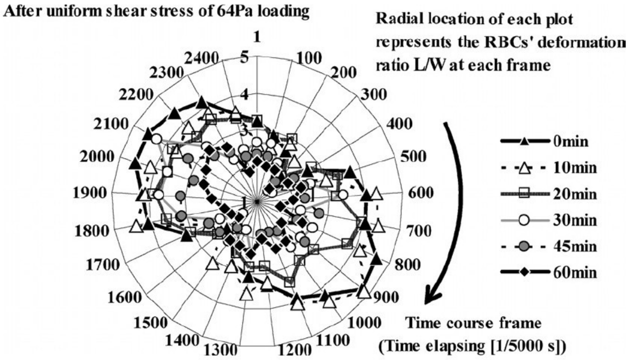

Figure 2.10: L/B under uniform shear stress of 64 Pa amplitude for varying exposure time [35]

where F is force, L is length, k is stiffness, t is time, α is a constant.

2.1.3.3 Tank-treading

The notion of "Tank-treading", first mentioned by Fischer et al. in [39], refers to the fact that the membrane is driven into a motion around the RBC, generating a shear flow in the cytoplasm. This phenomenon occurs when the RBC is in a suspension and encounters a shear rate above a certain threshold, and is consequently oriented and elongated. The angle and tank-treading frequency generally decrease with increasing elongation of RBC. The range of the predicted angles and tank-treading frequencies and their behavior with increasing elongation are in agreement with experimental observations on human RBC [40].

This issue has been broadly discussed. Many former investigations [40–44] were focused on kinetic models, while [45] focused on membrane energy dissipation; recent investigations [46–52] try to find general flow conditions for tumbling and tank-treading, and the trigger for the change of state between both.

According to Noguchi's mathematical model, besides tumbling and tank-treading, there exists another state for RBC, the swinging state. A tank-treading mode occurs with a constant inclination angle θ at low viscosity of the internal fluid μ_{in} or low membrane viscosity μ_{mb}; a tumbling mode occurs at high μ_{in} or μ_{mb} with low shear rate $\dot{\gamma}$; and a swinging motion occurs at middle μ_{in} or μ_{mb} with high $\dot{\gamma}$ [51].

Although much progress was already achieved in modeling tank-treading and tumbling behavior, the existing mathematical models are not really helpful for CFD-based hemolysis prediction, since they are very complex but of limited generality. Each model is usually dedicated to one single aspect, such as membrane kinetics in steady state, deformation or transient state. There is at present no general model able to describe at the same time membrane tension (generation of mini-holes), deformation and change of state.

2.1.4 RBC Membrane and Shear-induced RBC Alteration

The deformation of a RBC is dominated by the membrane rather than by cytoplasmic properties (internal viscosity) [18]. Hence, a deeper understanding of the RBCs' deformation and hemolysis requires the knowledge of the properties of RBC membrane.

Rand introduced a transient relation between shear stress and strain in RBC membrane [53]:

$$s = \tau \left[\frac{1}{G_2} + \frac{1}{G_1}(1 - e^{-(G_1/\mu_1)t}) + \frac{1}{\mu_2} t \right] \tag{2.12}$$

where s is membrane strain, G is elastic modulus and μ is viscosity. This equation is used in the hemolysis model discussed in Section 2.3.3.2.

Arwatz and Smits [54] modified Rand's model into:

$$s = \tau \left[\frac{1}{G_1}(1 - e^{-(G_1/\mu_1)t}) + \frac{1}{G_2}(1 - e^{-(G_2/\mu_2)t}) + \frac{1}{\mu_3} t \right] \tag{2.13}$$

where $\mu_1/G_1 = 0.1$ s and $\mu_2/G_2 = 20$ s. Both Rand's model and Arwatz's model can be used directly for hemolysis prediction using $\triangle H_b/H_b = Cs$ [54], where C is a constant. These two models, like the models discussed in Section 2.1.3.3, are based on the following assumptions: 1) the elastic constant of the RBC membrane is more than four orders of magnitude larger than the shear rigidity modulus of the cell; 2) the membrane can be treated as a simple, homogeneous substance built from a two-dimensional, incompressible material (i.e., with a fixed area); 3) the maximum fractional area expansion required to produce hemolysis is around 3%, when uniformly distributed [55].

Watanabe et al. numerically simulated the deformation of RBC under oscillation of shear stress, with a membrane stretch-based model. In a cyclically reversing unsteady flow at 5 Hz, the simulation results of L/B were consistent with experimental results of [34], as shown in Fig. 2.11. In a steady flow, the maximum principal strain is well correlated with the fluid shear stress, as demonstrated in Fig. 2.12. In a more complex, unsteady flow, the relation between shear stress and maximum of area-averaged strain (and thus hemolysis) became chaotic (Fig. 2.13), since the shape of a RBC was then determined not only by the fluid force acting on it at that moment but also by its deformation history [56].

The RBC membrane shows complex mechanical properties. The decreasing deformability of RBC, as a result of membrane hardening, is under certain conditions irreversible. Membrane hardening, being one aspect associated to RBC damage, can be induced by a long-time exposure to low or medium level of shear-rate, and can happen before, after or simultaneously to hemolysis. It can also influence the occurrence and level of hemolysis. However, a clear picture connecting membrane hardening and hemolysis is missing yet.

The deformability of a RBC is often measured by the shearing ratio:

$$(EI_{un} - EI_{pre})/EI_{un} \times 100\% \tag{2.14}$$

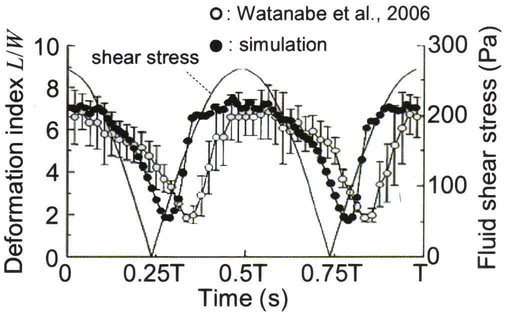

Figure 2.11: L/B under oscillation of shear stress [56]

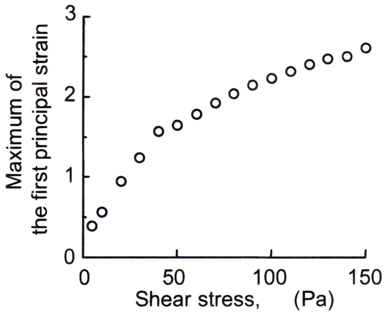

Figure 2.12: First principle strain vs. shear stress [56]

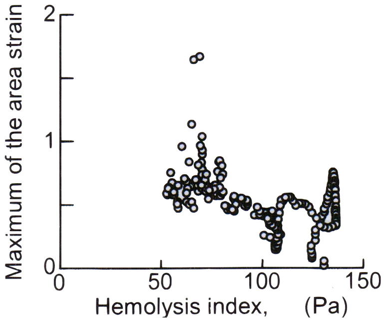

Figure 2.13: Maximal area-averaged strain vs. shear stress [56]

which is used a standardized measure to quantify the effect of shear, and is a difference of EI values between unsheared (EI_{un}) and pre-sheared (EI_{pre}) cells.

Mizuno's experiment shows that there are at least two different processes underlying structural changes of the RBC membrane under shear stress loading. One is caused by intense stress, with RBCs being promptly destroyed without noticeable alteration in the membrane skeleton; the other is caused by lower stress levels (in the experiment, shear rate of 420 s^{-1}) acting over a longer time and leading to strong alteration in the RBC membrane skeleton [57].

Kameneva's measurement showed that the RBC Deformation Index (DI),

$$DI = \frac{RBC\ suspension\ viscosity}{Suspension\ medium\ viscosity} \tag{2.15}$$

decreases after exposure to mechanical stress [58].

Lee's measurement shows that the threshold shear stress leading to RBC damage is approximately 30 Pa (after 120 s of pre-shearing), as shown in Fig. 2.14 [59]. Unfortunately, the RBC damage depends on both the magnitude and duration of shearing. The characteristic time of RBC relaxation is also influenced by pre-shear, as demonstrated in Fig. 2.15 [60].

Yokoyama's experiment shows a correlation between the fragility of RBCs, which is quantified by hemoglobin in plasma H_b, and deformability measured by L/B (the ratio of the RBC's long axis divided by its short axis), as shown in Fig. 2.16. The fragility of RBCs is showed to be as expected in a negative correlation with L/B [61].

Zeitz did more fundamental investigations concerning the irreversible alteration of the microscopic structure of RBC. The transient polymerization of protein fibers inside the cell, as found in sickle cell anemia, or a transient external force can trigger the formation of a

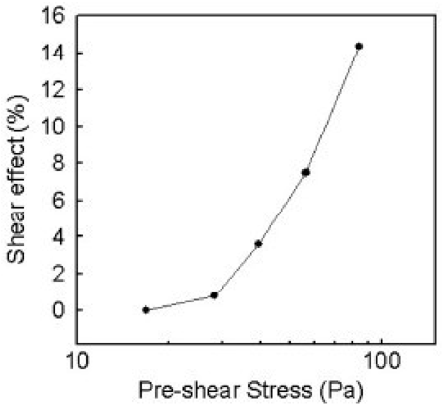

Figure 2.14: Shear effect as a function of pre-sheared stress [59]

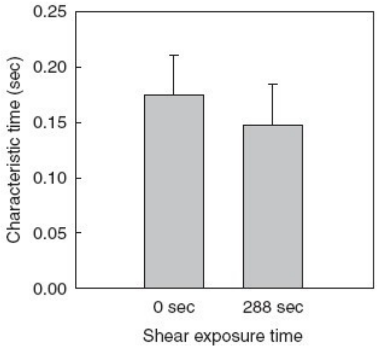

Figure 2.15: Characteristic time of RBC with and without pre-shear [60]

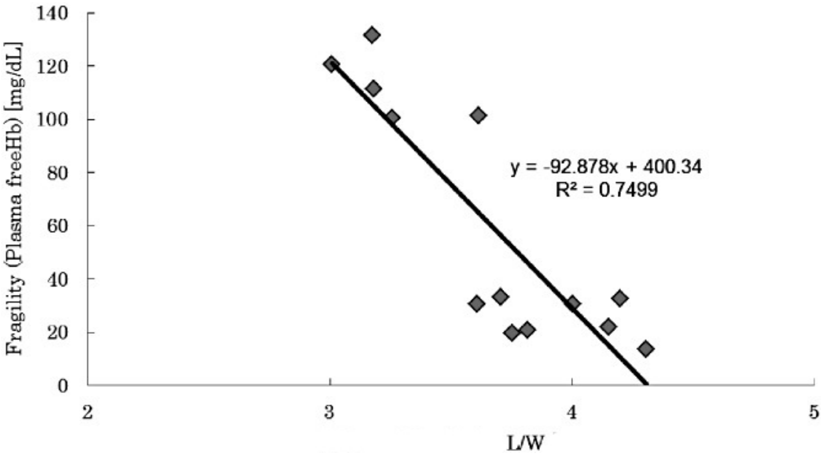

Figure 2.16: Relation between L/B and fragility of RBCs [61]

cytoskeleton-free membrane protrusion of μm dimensions. The complex relaxation kinetics of the cell shape is responsible for selecting the final state once the perturbation is removed, thereby controlling the reversibility (or not) of the deformation. In some cases, tubular protrusions are found to relax via an unusual ”pearling instability” [62].

Figure 2.17 shows three possible final states of a RBC with protrusion after removing the perturbation. The strongly deformed RBC shows a long, cytoskeleton-free membrane tube filled with hemoglobin, created by an internal or external force. Upon force removal, the cell may relax to its initial shape if the tube completely retracts (a), or to a different state where some membrane area remains outside the cell body and forms a spherical bulge (b). In (c), the tube might exhibit pearling during relaxation [62].

Figure 2.18 shows the region where a (meta)stable protrusion can exist, in the parameter space determined by K_c/σ (elastic ratio) and ϵ_0 (the cytoskeleton pre-stress). Figure 2.19 is the critical initial protrusion volume beyond which a transient protrusion always fails to retract inside the cell body. Case (a) is for a protrusion created by an external force, which is a function of ratio of the volume to area exchange times (here for $K_c/\sigma = 10$ and $\epsilon_0 = 0.25$), while Case (b) is for a protrusion created by a bundle of protein fibers (4 nm in size) [62].

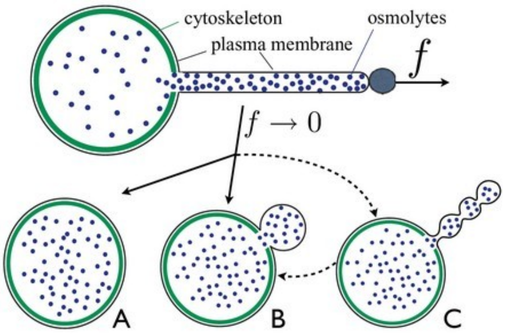

Figure 2.17: Three possible evolutions of a protrusion after removal of perturbation [62]

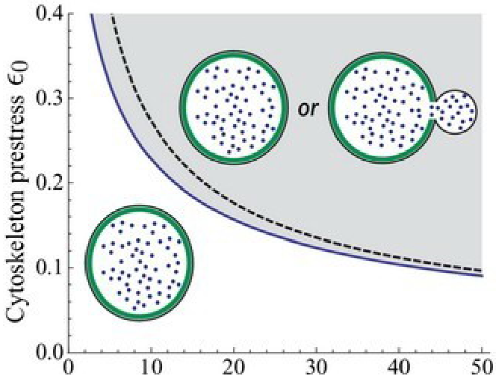

Figure 2.18: Condition for the existence of a protrusion as function of K_c/σ and ϵ_0 [62]

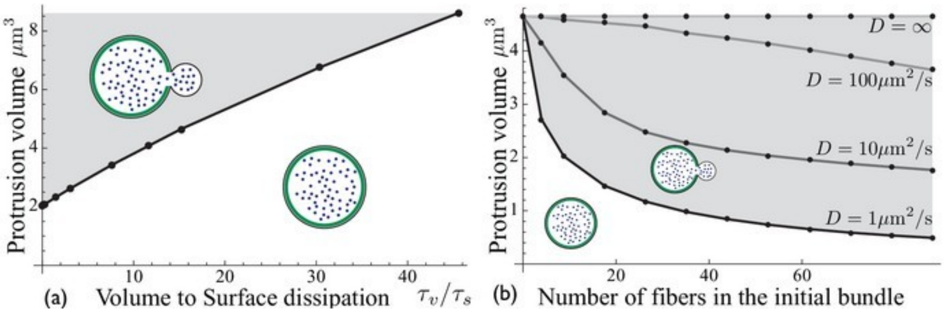

Figure 2.19: Limit conditions leading to complete retraction of a protrusion [62]

2.1.5 RBC Diffusion

Srivastav et al. studied the diffusion coefficient of a RBC suspension by injecting a jet of RBCs in a microfluidic channel. Results show that the diffusion coefficient of a RBC suspension is comparable to that of a suspension of drops, since RBCs are usually in tumbling motion and can thus be considered as symmetric when averaging over one rotation period, as long as no deformation occurs. On average, there should therefore be no diffusion, as for spheres. Since the cells meet each other over a time interval shorter than one rotation period and encounter deformation, averaging does not rule out all asymmetries and some diffusion is expected. However, it should still be lower than the diffusion of drops that are elongated and flow with their main axis constantly inclined with a given non-zero angle relatively to the flow direction [63].

Tan et al. studied numerically the hydrodynamic diffusion coefficients of a suspension of elastic capsules of viscosity ratio unity and volume fraction up to 20%, and found that the coefficient does not increase monotonously with elastic capillary number. Instead, it drops when the capsules become sufficiently soft [64].

RBC diffusion is one possible reason for the over-prediction often encountered when using numerical hemolysis methods, since the highest shear stress usually occur near walls. However, due to RBC diffusion and to the resulting inhomogeneous concentrations, RBCs are less often found near walls than in the main stream. Till now, no numerical hemolysis method has been proposed to take into account this effect in CFD.

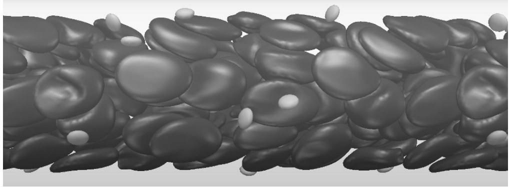

Figure 2.20: Lower RBC concentration near walls, as induced by diffusion [65]

2.1.6 Other Factors Influencing Hemolysis

Leverett's measurement shows that an air-blood interface may be responsible for hemolysis, but that RBC-RBC interactions are not an important mechanism for erythrocyte destruction. A temperature exceeding 49°C causes significant hemolysis and fragmentation [66].

Hashimoto carried out complex experimental measurements concerning hemolysis under periodically fluctuating shear stress [67]. One particularly interesting result is that hemolysis increases linearly with shear stress fluctuation frequency. This effect cannot be reproduced by any of the current hemolysis models discussed in Section 2.2.

2.1.7 Direct Microscopic RBC Simulations

Direct RBC simulations lead to extremely high computational requirements. Pozrikidis simulated a single RBC with a surface grid of 512 quadratic elements for 4000 time steps on a single-core 2.4GHz CPU. The simulation lasted 1 week [68].

Dupin simulated 200 RBCs, each with a surface grid of 800 tetrahedral elements, under a shear rate of 10 s^{-1} for 4000 time steps. The volume fraction of RBCs was 30%. The total simulation time was 150 hours using 15 AMD-Opteron CPUs. The simulation considered RBC deformation, relaxation, tank-treading and tumbling, but did not account for any interaction between neighboring RBCs [69].

Liu carried out a simulation with a finer surface grid of 4567 tetrahedral elements, but a smaller number of RBCs. The simulation considered RBC-RBC interaction and RBC-wall interaction [70].

As already discussed in Section 2.1.3.3, such simulations are very interesting to investigate some particular aspect, but do not cover all important processes and cannot be coupled with a full CFD model within the next years.

2.1.8 Intermediate Conclusion

Since a comprehensive mathematical model describing RBC behavior from microscopic observations is not available yet, it is not possible to derive a proper macroscopic model describing cell damage and hemolysis. For this reason, all hemolysis prediction models currently employed in CFD try to connect hemolysis directly or indirectly to macroscopic flow properties (stress or strain), without considering any microscopic effects.

2.2 Literature Review on Numerical Hemolysis Prediction

When considering hemolysis in a CFD simulation, blood is usually simulated as a homogeneous non-Newtonian fluid instead of being treated as multiphase suspension, in order to reduce the computational cost, as explained in the previous sections.

Most existing hemolysis codes are typically in a one-way coupling with the CFD-solver. Flow-induced shear stress functions as the exchange quantity between flow simulation and RBC behavior. One-way coupling means that the variables describing RBC deformation and hemolysis only exist in the hemolysis code, but not in the main flow simulation; the velocity gradient influences the deformation of RBC and thus hemolysis, but the RBCs and their deformation have no influence whatsoever on the velocity/pressure/turbulence equations solved by CFD.

2.3 Computing strain and stress

One difficulty common to all models discussed in this section is how to transform in an appropriate manner a tensor $\underline{\tau}$ (involving 9 components, but, due to symmetry, only 6 free parameters) into a single scalar value τ. This is not so straightforward, since the components of τ are associated to different directions in space but also to different effects (shear stress or normal stress, corresponding to two very different forces acting on the RBC). For instance, in order to compute the scalar shear stress τ appearing later in Eq. (2.22), [71–73] use following equation:

$$\tau = \left[\frac{1}{6}\sum_{i,j}(\tau_{ii} - \tau_{jj})^2 + \sum_{i,j}\tau_{ij}^2\right]^{\frac{1}{2}} \tag{2.16}$$

with

$$\tau_{ij} = \mu\frac{\partial v_i}{\partial x_j} \tag{2.17}$$

where v_i refers to the velocity component in i direction.

However, alternative definitions for τ are also found in other publications. For instance, extremal values are used in [74]:

$$\tau = \frac{1}{2}\max\left[|\epsilon_1 - \epsilon_2|, |\epsilon_2 - \epsilon_3|, |\epsilon_1 - \epsilon_3|\right] \tag{2.18}$$

as well as in [75] (where ϵ_i refers to the principal stress):

$$\tau = \frac{1}{2}\left\{\max\left[(\epsilon_1 - \epsilon_2)^2, (\epsilon_2 - \epsilon_3)^2, (\epsilon_1 - \epsilon_3)^2\right]\right\}^{\frac{1}{2}} \tag{2.19}$$

In [13], all terms of the tensor are taken into account:

$$\begin{aligned}\tau = \Bigg[&\frac{1}{3}(\tau_{11}^2 + \tau_{22}^2 + \tau_{33}^2) - \frac{1}{3}(\tau_{11}\tau_{22} \\ &+\tau_{11}\tau_{33} + \tau_{33}\tau_{22}) + \frac{1}{3}(\tau_{12}^2 + \tau_{13}^2 + \tau_{23}^2)\Bigg]^{\frac{1}{2}}\end{aligned} \tag{2.20}$$

To our knowledge, no study has been published concerning the possible impact of these different definitions on the hemolysis prediction. This is why, in the rest of this Thesis, we will always follow the original method proposed in the literature for a corresponding model.

2.3.1 Stress-based Model (Power-law Equation)

If local hemolysis is assumed in a direct ratio (especially in a power-law relationship) to local shear stress, the model is named a stress-based model (Fig. 2.21).

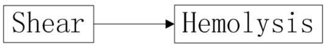

Figure 2.21: (Shear) stress-based model

The reference model in this category reads

$$\triangle H_b/H_b = 3.63\,10^{-7}\tau^{2.416}t^{0.785} \tag{2.21}$$

and was already given as Eq. (1.1). This model and the obtained parameters have been obtained from fitting measurement data discussed in [76, 77]. The underlying experiments correspond to submitting RBC to a shear stress constant in time, with values of τ up to 255 Pa and an exposure time t up to 700 ms. The power values are obtained by curve fitting. Equation (2.21) has been later implemented following different numerical approaches. The formulation seems adequate for predicting hemolysis at constant shear stress with intermediate values of τ and of exposure time t. This configuration is, however, not found in many practical applications. When considering varying shear stress in a higher range (300 to 1500 Pa) but with a shorter exposure time (10 to 100 ms), it has been observed that the hemolysis rate predicted by Eq. (2.21) overestimates hemolysis by at least an order of magnitude [13, 78, 79]. Unfortunately, these parameters are typical of those found in blood pumps and most blood supply equipments. Therefore, and in spite of its very attractive simplicity, this model does not appear suitable for our purpose (optimizing blood pumps). However, it is still a very good alternative as long as the considered applications fulfill the underlying hypotheses (constant and not too high value of τ, intermediate exposure time). It is also still widely used outside of such conditions, though, mostly due to the shortcomings of alternative models, as discussed in what follows.

Another group of power values for Eq. (2.21) is found in [71]:

$$\triangle H_b/H_b = 3.63 \times 10^{-6}\tau^{1.991}t^{0.765} \tag{2.22}$$

Note that the factor 10 difference in the pre-factor term in Eq. (2.22)compared to Eq. (2.21) is not a typing mistake, but appears as such in [71].

2.3.1.1 Considering a threshold in shear stress

Experiments with RBC discussed in the first part of this chapter have shown that, below a certain level for τ, no hemolysis is observed at all. In order to take into account this observation, a shear-stress threshold τ_s below which hemolysis is inactive was introduced in later versions of the power-law model and of all further models. Combined for instance with the power-law equation, this leads to Eq. (2.23):

$$\begin{aligned} &\triangle H_b/H_b = 3.63\;10^{-7}\tau^{2.416}t^{0.785} && (\text{for } \tau > \tau_s) \\ &\triangle H_b/H_b = 0 && (\text{for } \tau \leq \tau_s) \end{aligned} \tag{2.23}$$

One obvious shortcoming of this straightforward threshold approach is that, when reaching the threshold τ_s, the hemolysis will jump for Eq. (2.23) in a discontinuous way from 0 to $3.63\;10^{-7}\tau_s^{2.416}t^{0.785}$. To avoid this problem, a ramp function could be built into the model, for instance based on an hyperbolic tangent. However, such an approach has apparently never been published.

Different values for τ_s are found in the literature, varying between 100 and 250 Pa [80]. Looking back at the experiments [76, 77] leading to Eq. (2.21), it is somewhat disturbing to see that the *maximal* shear stress imposed in these experiments (255 Pa) is for some other authors nearly identical to the threshold *below which* no hemolysis at all is observed ($\tau_s = 250$ Pa). This contradiction is a first indication that it is extremely complex to design suitable experiments for a proper estimation of hemolysis in RBC, and this is due to four main reasons:

1. Deformation and shearing of RBC involve a tensor τ, while all models rely at the end on a single scalar τ;

2. RBC do not react identically to different flow solicitations. For instance, shearing and elongation are known to lead to completely different behaviors for animal cells [81, 82];

3. RBC are not inert particles, but react to the perturbation induced by the flow with their own time-scale. As a consequence, the experiment attempts to measure a quantity that is changing due to the experiment itself;

4. The level of shear stress and the exposure time (or frequency) are not independent quantities for the RBC, explaining why different experimental procedures might lead to contradictory conclusions.

From these observations, it is clear that the experiments needed to develop suitable hemolysis models are extremely challenging, sometimes even impossible. It is nevertheless useful to further compare the results obtained with different published hemolysis models, as done in the rest of this chapter.

In an attempt to take into account the fourth observation listed previously, several authors have introduced the threshold in shear stress as a function of the exposure time. For instance, Nerem introduced the time-dependent threshold equation [83]:

$$\tau_s = 88.905\, t^{-0.3372} \tag{2.24}$$

as the condition for hemolysis to occur.

Sharp and Mohammad introduced another formulation for a shear-stress threshold function of the exposure time [84]:

$$t(\tau_s/1500 - 1)^2 = 0.01 \tag{2.25}$$

An underlying assumption for all models is that the hemolysis process starts with a healthy RBC (100% hemoglobin content) without any previous hemolysis history. From this simple fact and looking back at the power-law models (Eqs. (2.21) and (2.22)), it is possible to draw an important conclusion: when submitted to a constant shear stress exceeding the threshold, the relative hemolysis potential of a RBC is decreasing with time, since the power for time t in the models (time being now directly equivalent to the exposure duration) is around 0.77, noticeably smaller than 1. This means that, when submitted to a constant shear stress $\tau \geq \tau_s$, and considering the same lapse of time $\triangle t$, the lysis potential starting from time t ($t > 0$) is lower than at the beginning of the process $t = 0$. Considering for instance Eq. (2.21), this is obvious, since:

$$(\triangle t)^{0.785} > (t + \triangle t)^{0.785} - t^{0.785} \tag{2.26}$$

This observation is directly a consequence of the third observation listed previously. Biological reasons can be proposed to explain this fact:

- Former hemoglobin leakage reduces the hemoglobin quantity within the RBC, thus reducing its volume and lowering membrane tension;

- Irreversible changes in RBC membrane (membrane hardening) when submitted to stress, reduces the potential of mini-holes formation and thus reduces hemoglobin leakage [55, 57, 58, 60–62].

In order to obtain correct predictions, a numerical hemolysis model should take into account this effect. However, the fact that time appears with a non-unity exponent leads to difficulties during the numerical integration. This important fact must be taken into account for hemolysis modeling. Suitable approaches have been developed to solve this problem and are discussed in what follows.

2.3.2 Practical Solution Methods for Stress-based Model

2.3.2.1 Method A

In order to implement the power law method into a CFD solver, a derived formulation is far more practical. The process begins by rewriting the original Eq. (2.21) (the same treatment is obviously possible as well for Eq. (2.22)) into the following form [80, 85–87] :

$$\triangle H_b/H_b = \left[(3.63\ 10^{-7})^{(1/0.785)}\tau^{(2.416/0.785)}t\right]^{0.785} \tag{2.27}$$

Then, the part within the square brackets is linear in time, and can be recast as a complete differential form:

$$\frac{dH_L}{dt} = (3.63\ 10^{-7})^{(1/0.785)}\tau^{(2.416/0.785)} \tag{2.28}$$

where H_L refers to the local hemolysis taking place within a CFD grid cell. Equation (2.28) is then rewritten as a standard transport equation, as found in any common CFD-solver:

$$\begin{aligned}\frac{\partial H_L}{\partial t} + \mathbf{v}.\nabla H_L = \\ \delta(3.63\ 10^{-7})^{(1/0.785)}\tau^{(2.416/0.785)}(1-H_L)\end{aligned} \tag{2.29}$$

with

$$\delta = \begin{cases} 0 & \text{if}\quad \tau < \tau_s \\ 1 & \text{if}\quad \tau \geq \tau_s \end{cases} \tag{2.30}$$

Multiplying the right-hand side with $(1-H_L)$ has been done to assure that the hemolysis rate measured by H_L reduces with time at constant shear stress, as discussed previously. The hemolysis value corresponding to the whole CFD domain is finally collected along domain outlet by computing a mass-flow-average. The obtained value for each pathline (or streamline for steady simulations) is finally transformed back to real time thanks to a power of 0.785:

$$\frac{\triangle H_b}{H_b} = \frac{\sum_{\text{outlet cells}} {H_L}^{0.785}\dot{m}_{\text{cell}}}{\sum_{\text{outlet cells}} \dot{m}_{\text{cell}}} \tag{2.31}$$

2.3.2.2 Method B

Though it looks partly quite similar to the power-law method in its structure, Method B is a purely empirical, macroscopic formula, originally developed for blood pumps [73]:

$$\triangle H_b/H_b = 3.8\tau^{-1.9}t^{1.5}V^{0.25}(\triangle p)^{1.4} \tag{2.32}$$

It is based on a regression analysis from experimental data, as discussed in [73]. The variable V refers to volume and $\triangle p$ refers to pressure head of blood pump.

2.3.2.3 Method C

In this alternative method the blood damage index D_b is computed as a function of the lysis induced in each grid cell [72, 88, 89]:

$$D_b = \tau^{b/a}\, t \tag{2.33}$$

For each integration step the cumulative mechanical dose contributes to a damage increment, yielding finally the discrete formulation along each streamline (corresponding to a total residence time t_i between inflow and outflow of the CFD domain):

$$\begin{aligned}&\triangle H_b(t_i)/H_b = \\ &\sum_{\text{inlet}}^{\text{outlet}} a\, c \left[\sum_{j=1}^{i} \tau(t_i)^{b/a} \triangle t_j + D_b(t_0)\right]^{a-1} \tau(t_i)^{b/a} \triangle t_i\end{aligned} \tag{2.34}$$

where $D_b(t_0)$ is the mechanical dose already accumulated by the cell at the integration start time and a, b, c are empirical parameters. The term in the square brackets represents the whole mechanical dose acting on the cell moving along the pathline from the starting observation time until the ith instant, whereas $\tau(t_i)^{b/a} \triangle t_i$ is the elementary mechanical dose received by the RBC in the ith interval [72]. The parameter values finally proposed by [89] read:

$$(a_1, b_1, c_1) = (0.77, 3.075, 3.31\ 10^{-6}) \tag{2.35}$$

Another group of values are given by [90]:

$$(a_2, b_2, c_2) = (1.3198, 0.6256, 10^{-5}) \tag{2.36}$$

These two widely different parameter sets highlight again the difficulty of obtaining proper validation data from experiments, and are an indication of a poor generality.

Following [11], it is possible to reformulate Eq. (2.34) as a transport equation, see Eq. (2.37). However, this equation unfortunately cannot be directly coded into any major CFD solver due to its structure:

$$\begin{aligned}&\frac{d(\triangle H_b/H_b)}{dt} + \nabla.(\mathbf{v}(\triangle H_b/H_b)) - \nabla.(D_b \nabla(\triangle H_b/H_b)) \\ &= a\, c \left(dt + \left(\frac{\triangle H_b/H_b}{C\tau^b}\right)^{1/a}\right)^{a-1} \tau^b\end{aligned} \tag{2.37}$$

Compared with Method A, this method C appears to be more sensitive to the employed discretization in space and time.

2.3.2.4 Method D

As another alternative, Gu and Smith propose following equation [91]:

$$\begin{aligned}\triangle H_b/H_b = \left(\frac{t_{i,j}}{t}\right) \sum_j \sum_i 1.8\ 10^{-6} \tau_{i,j}^{1.991} (t_{i+1,j} \\ - t_{i,j})^{0.765} \left(\frac{t}{t_{i,j}}\right)^{0.71}\end{aligned} \tag{2.38}$$

where t is the total time for traveling along a pathline, i is pathline number, j is timestep number.

This is a purely arithmetic modification of Eq.(2.22). The obtained hemolysis result depends again on the discretization, due to the non-unity exponent in time.

2.3.3 Strain-based Models

If local hemolysis is not a direct result of local shear stress, but is instead associated to an intermediate variable (such as the membrane surface extension, or RBC deformation), the model is typically named a strain-based model (Fig. 2.22).

Figure 2.22: Strain-based model

2.3.3.1 Method E: a Strain-tensor-based Lagrangian Model

In this model, the deformation of RBCs is due to accumulation of shear stress in the past history, and hemolysis is due to instantaneous deformation [13, 78].

A red blood cell is modeled as a deformable droplet in a flow. Its shape and orientation are represented by a symmetric, positive-definite 3rd-order morphology tensor S. The evolution of S occurs subject to four effects:

1. resistance to deformation and rotation: $-(S - g(S)I)$;
2. shear-induced deformation: $\tilde{\varepsilon}.S + S.\tilde{\varepsilon}$;
3. shear-induced rotation: $\tilde{W}.S + S.\tilde{W}$;
4. rotation of the surrounding frame: $\Omega.S + S.\Omega$.

Combining all four items together with factors f_1, f_2, f_3 for the first three terms, the equation for deformation is obtained:

$$\begin{aligned}\frac{dS}{dt} =& \frac{\partial S}{\partial t} + \mathbf{v}.\nabla S \\ =& -f_1[S - g(S)I] + f_2[\tilde{\varepsilon}.S + S.\tilde{\varepsilon}] \\ &+ f_3[\tilde{W}.S + S.\tilde{W}] + [\Omega.S + S.\Omega]\end{aligned} \tag{2.39}$$

where, $\tilde{\varepsilon} = (1/2)(\nabla\mathbf{v} + \nabla\mathbf{v}^T)$ is the (symmetric) strain tensor of the flow; $W = (1/2)(\nabla\mathbf{v} - \nabla\mathbf{v}^T)$ is the (antisymmetric) vorticity tensor of the flow. Then,

$$\tilde{W} = W - \Omega \tag{2.40}$$

is the vorticity really encountered by the droplet in its own frame of reference. Finally, $g(S)$ is given by:

$$g(S) = 3\; III/II \tag{2.41}$$

with $III = (\mathrm{tr}(S))^2 - \mathrm{tr}(S^2)$, $II = \det(S)$, the invariants of tensor S. The rotation rate of the frame of reference Ω is given by:

$$\Omega = \tilde{e}_i \left(\frac{\partial \tilde{e}_i}{\partial t} + \mathbf{v}.\nabla \tilde{e}_i \right) \tag{2.42}$$

where (e_i) refers to the eigenvectors of S. Finally, hemolysis is calculated by:

$$\frac{\triangle H_b}{H_b} = 3.63\ 10^{-7} \left(\mu \sqrt{\frac{f_1^2 \varphi^2}{(1-\varphi^2) f_2^2}} \right)^{2.416} t^{0.785} \tag{2.43}$$

where $\varphi = (L-B)/(L+B)$ is the instantaneous aspect ratio of the droplet, denoting L the longer length contained within the droplet ellipsoid, and B its shorter length.

Equations (2.39) and (2.42) are discretized in a Lagrangian manner with a first-order explicit approximation:

$$\frac{dS_{n+1}}{dt} = \frac{S_{n+1} - S_n}{\triangle t} \tag{2.44}$$

$$\Omega_n = (e_i)_n \frac{\partial (e_i)_n}{\partial t} = (e_i)_n \frac{(e_i)_n - (e_i)_{n-1}}{\triangle t} \tag{2.45}$$

Inserting these last two equations into Eq. (2.39), it comes:

$$\begin{aligned} &\frac{S_{n+1} - S_n}{\triangle t} = -f_1[S_n - g(S_n)I] \\ &+ f_2[\tilde{\varepsilon}_n.S_n + S_n.\tilde{\varepsilon}_n] + f_3[\tilde{W}_n.S_n + S_n.\tilde{W}_n] \\ &+ \left[(e_i)_n \frac{(e_i)_n - (e_i)_{n-1}}{\triangle t} \right].S_n + S_n.\left[(e_i)_n \frac{(e_i)_n - (e_i)_{n-1}}{\triangle t} \right] \end{aligned} \tag{2.46}$$

Then, inserting Eqs. (2.40) and (2.41) into Eq. (2.46), S_{n+1} at the next step is calculated explicitly based on the former two time steps:

$$\begin{aligned} S_{n+1} = &S_n + \left(-f_1 \left[S_n - \frac{0.5((\mathrm{tr}(S_n))^2 - \mathrm{tr}(S_n^2))}{\det(S_n)} I \right] \right. \\ &+ f_2[\tilde{\varepsilon}_n.S_n + S_n.\tilde{\varepsilon}_n] \\ &+ f_3 \left[(W_n - (\mathrm{eigv}(S_n)) \frac{\mathrm{eigv}(S_n) - \mathrm{eigv}(S_{n-1})}{\triangle t}).S_n \right. \\ &\left. +S_n.(W_n - (\mathrm{eigv}(S_n)) \frac{\mathrm{eigv}(S_n) - \mathrm{eigv}(S_{n-1})}{\triangle t}) \right] \\ &+ \left[(\mathrm{eigv}(S_n)) \frac{\mathrm{eigv}(S_n) - \mathrm{eigv}(S_{n-1})}{\triangle t} \right].S_n \\ &\left. +S_n.\left[(\mathrm{eigv}(S_n)) \frac{\mathrm{eigv}(S_n) - \mathrm{eigv}(S_{n-1})}{\triangle t} \right] \right) \triangle t \end{aligned} \tag{2.47}$$

where eigv() solves for all eigenvectors.

Such a backward discretization is numerically unstable. The resulting numerical diffusion depends on the total number of points on each pathline, and on the interpolation between pathline points. Once again, the result of this method depends on the underlying discretization, since the term involving t is not linear in Eq. (2.43).

2.3.3.2 Method F: a Strain-scalar-based Lagrangian Model

As shown in Fig. 2.23, this model introduces a scalar s for the area-averaged strain of the RBC membrane and $s_c = 0.064$ 1/s as the critical strain for membrane failure. From the

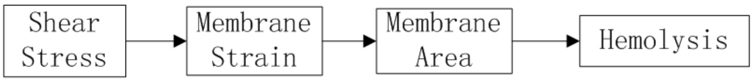

Figure 2.23: Strain-scalar-based model.

strain, a membrane deformation can be computed, and finally hemolysis can be deduced. Equation (2.48) is the relation between s, shear stress and exposure time [92, 93]:

$$\frac{s}{s_c} = \frac{4a\,b}{5}(\tau - \tau_e)[C_0 + C_1(1 - e^{-C_2 t}) + C_3 t] \tag{2.48}$$

where $\tau_e = 150$ Pa is the stress required to elongate the cell to an iso-area ellipsoid, t is the exposure time, $a = 39.01$ is an empirical constant, $b = 1.7$ μm is the minimum radius of a deformed RBC, $C_0 = 35$ m/N and $C_1 = 39$ m/N are related to the Young's moduli of the membrane, while $C_2 = 8$ s^{-1} and $C_3 = 0.15$ m/N were obtained by curve fitting of experimental data.

Equation (2.48) can be rewritten in a total differential form:

$$\begin{aligned}\left(\frac{s}{s_c}\right)_i = \sum_{j=0}^{m} \Bigg\{ & \frac{4\,a\,b}{5}\left[C_0 + C_1(1 - e^{-C_2 t_{i,j}})\right. \\ & \left.+ C_3 t_{i,j}\right](\tau_{si,j} - \tau_{si,j-1}) \\ & + \frac{4\,a\,b}{5}(\tau_{si,j} - \tau_e)\left[C_1 C_2 e^{-C_2 t_{i,j}} + C_3\right](t_{i,j} - t_{i,j-1}) \Bigg\}\end{aligned} \tag{2.49}$$

where i refers to the number of a pathline, j refers to the steps along this pathline. At any j, if $(\tau_{si,j} - \tau_{si,e}) < 0$, it is reset to $(\tau_{si,j} - \tau_{si,e}) = 0$, inactivating the last term in Eq. (2.49). On the left-hand side of this equation, $(s/s_c)_i$ is the normalized strain value along pathline i. If along a particular pathline $(s/s_c)_i > 1$, then the RBCs traveling along this pathline are predicted to rupture, leading to 100% hemolysis. As long as $(s/s_c)_i \leq 1$, the corresponding value is used to determine the hemolysis ratio (Fig. 2.23). Unfortunately, the detailed equations used to compute hemolysis are not given in [92, 93]... The only useable information is that the aspect ratio of RBC is calculated from s by:

$$V = \frac{4}{3}\pi L B^2 \tag{2.50}$$

$$A = 2\pi\left[B^2 + \frac{L^2 B}{\sqrt{L^2 - B^2}} \arcsin\sqrt{1 - \frac{B^2}{L^2}}\right] \tag{2.51}$$

$$\frac{A}{A_0} = 1 + s \tag{2.52}$$

where A refers to surface area, V refers to cell volume, L and B are long axis and short axis of RBC.

Finally, let us note that this model does not consider the recovery of the membrane strain when the shear is released.

2.4 Choosing an Hemolysis Model for Blood Pump Optimization

2.4.1 Lagrangian vs. Eulerian Methods

In Lagrangian methods, hemolysis is calculated along pathlines (flow trajectories). Obviously, a given pathline depends on its origin in space and time. When steady CFD computations are involved, time is not an issue any more; in that case, pathlines are identical with streamlines. The starting points retained for the pathlines are typically chosen at the inlet (inflow boundary condition) of the CFD domain. This is sufficient for simple flow topologies without noticeable recirculation regions. However, in more complex geometries (indeed often found in practice), recirculation regions and large stable vortical structures are often encountered in certain regions of the flow. Since such structures appear stable in a steady simulation, pathlines released from the inlet may not cover the whole flow domain, impacting hemolysis prediction in an unacceptable manner. For steady CFD simulations, coding a Lagrangian-type hemolysis model can be done in a post-processing step, after completing the CFD simulation, resulting in a completely separate, and hence quite flexible and simple, hemolysis prediction. In this sense, Lagrangian models can save memory. However, they often lead to a lower accuracy and, as explained previously, they depend on (sometimes arbitrary) user-defined choices concerning the pathlines. They are far less attractive when unsteady flows are involved, as is the case for our target application. Additionally, many commercial software are unable to track pathlines through moving grid interfaces, as often needed for practical pump simulations. In such a case, Lagrangian methods cannot be used at all. Since particles used to track pathlines should only be released after the flow is fully developed in the domain, Lagrangian methods usually involve one flow-through time more compared to an Eulerian approach. Finally, depending on the software, continuous particle release might be needed to determine pathlines, implying at the end a huge amount of pathlines.

An Eulerian method uses additional transport equations within the CFD solver to describe hemolysis and, if needed, intermediate and related variables. The hemolysis calculation is then typically carried out simultaneously while solving continuity, Navier-Stokes and (possibly) turbulence equations. No additional post-processing step is needed. Eulerian methods are better for blood pump CFD-O than Lagrangian method, since they lead to far lower computational costs. The numerical procedure is simplified by avoiding any extra post-processing step.

Table 2.2 is a first classification of the families of hemolysis models that have been and will be discussed in this chapter. The absence of any strain-based Eulerian method is mostly due to the inherent difficulties associated to this approach, as discussed later: first, the employed equations usually do not allow any temporal variable in the source term; additionally, considering existing commercial and open-source CFD codes, it is either impossible to code a tensor as the transported variable (ANSYS, STAR-CCM+) or it is impossible to code dot or eigenvector operations acting on the transported tensor (OpenFOAM). Though these difficulties can in principle be solved, and in spite of the interest of a strain-based Eulerian approach, this has prevented any such development yet. At the end of this chapter, the equations corresponding to such a model are introduced as a preparatory step for future projects.

Before discussing the details of the involved comparisons, a first summary of the advantages and disadvantages associated to all hemolysis models is proposed in Table 2.3.

A strain-based model is a priori better than a stress-based model, since the former can take into account more complex steps and physical properties of RBC. However, it does not mean that strain-based models automatically lead to a more accurate prediction.

	Lagrangian Method	Eulerian Method
Stress-based	Section 2.3.2.3 Section 2.3.2.4	Section 2.3.2.1
Strain-based	Section 2.3.3.1 Section 2.3.3.2	

Table 2.2: Classification of reviewed and generally applicable hemolysis models

Model in Section	Advantage	Disadvantage
2.3.2.1	Fully Eulerian, source term includes no t, accounts for hemolysis history	Physically too simple
2.3.2.2	Easy coding	Empirical formula, only for blood pumps
2.3.2.3	Accounts for shear history, partially ”strain-based”	Fundamentally still ”stress-based”
2.3.2.4	Quite easy coding	Physically too simple, no simple transport equation
2.3.3.1	Account for deformation history and relaxation	tensor-based with dot and eig() operations, no simple transport equation
2.3.3.2	Accounts for deformation history	No simple transport equation, no treatment of $\tau < \tau_e$

Table 2.3: First comparison of hemolysis models

All existing stress-based models have been derived from the basic power-law equation, Eq. (2.21), even if the obtained results may differ by orders of magnitude depending on the employed parameter sets.

The model in Section 2.3.3.1 is the only one fully accounting for a relaxation of the deformation, through the term $-(S - g(S)I)$.

The model in Section 2.3.3.2 partly accounts for RBC relaxation to its original shape. However, the proposed treatment for $\tau < \tau_e$ is not satisfactory.

2.4.2 A Simple 1D Validation

First, a simple one-dimensional configuration is considered to discuss the hemolysis level predicted by different models. Numerical results are compared with experimental data presented in [67]. In the experiment, a heparinized sample of beagle blood is filled between a stationary convex circular cone and a rotating concave circular cone (rheometer). The rotor-convex is driven to rotate with sinusoidal speed, thus generating a sinus-oscillating shear rate in the blood. The maximum shear rate value is set to 250, 600 and 1000 s^{-1} respectively, while the oscillation frequency is fixed to 0.5 Hz, with a total exposure duration of 7200 s.

A Matlab code has been written to deliver the results corresponding to the different numerical models. Blood viscosity is taken constant at 0.0035 Pa.s. Method A (see Section 2.3.2.1) is implemented without shear stress threshold ($\tau_s = 0$). Method B (see Section

2.3.2.2) is not included in this comparison, since it has been especially developed for blood pumps; in the present experiment, there is no pressure build-up and thus no value for $\triangle p$. Method C (see Section 2.3.2.3) has been coded using the first group of constants, Eq. (2.35). The second group of constants for method C (Eq. (2.36)) leads to values of $\triangle H_b/H_b$ larger than 1 for all 3 values of shear rate. For this reason, the results are not depicted in Fig. 2.24, in which the comparison between all models is presented

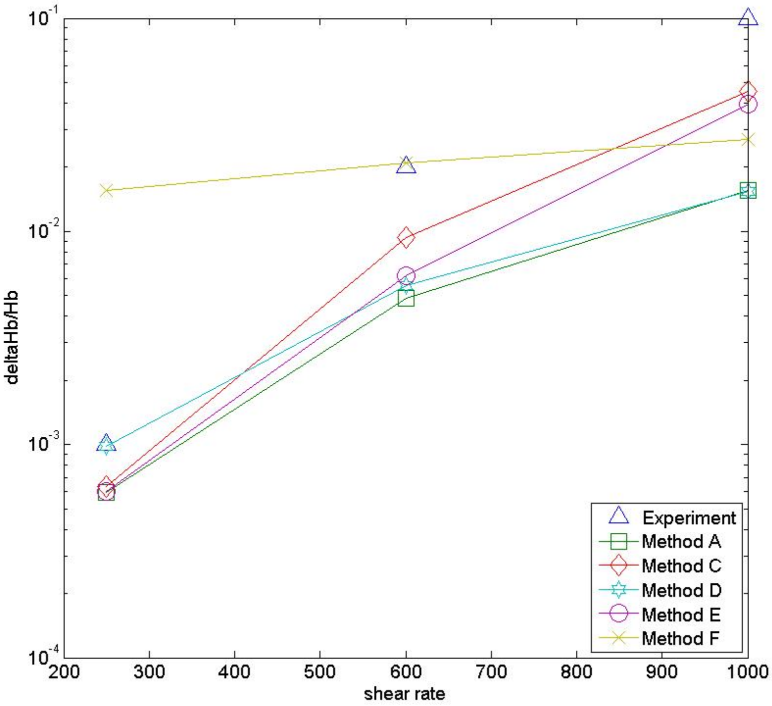

Figure 2.24: Numerically predicted relative hemolysis $\triangle H_b/H_b$ as a function of maximum shear rate. Blue triangles: experiments; symbols with lines: models, see legend. All results are shown for an exposure duration of 7200 s.

Methods A and D (see Section 2.3.2.4 for the latter) strongly under-estimate the measured hemolysis value, increasingly so for higher shear rate. A possible reason is that the power-law equation has been derived from experimental data with much shorter exposure time. Anyway, both methods do not predict correctly the experimental observations, with almost an order of magnitude difference for a peak shear rate of 1000 s^{-1}.

Results of Method C with constants from Eq. (2.35) lie clearly below the experimental data. However, the discrepancy is typically only a factor 2, and the slope of the curve follows closely the experimental curve. From all models tested, Method C is clearly the winner for this comparison. Taking for the constant c a value of 7 10^{-6} instead of 3.31 10^{-6}, an almost perfect agreement with those measurements could be achieved.

Method E (see Section 2.3.3.1) is by far the most complicated one. It shows a curve slope second close to the experimental data, and lies only slightly below the results of Method C. However, in addition to its numerical complexity, method E leads also to a high level of numerical diffusion, in particular due to the underlying first-order discretization. When taking into account complexity and numerical cost in addition to the accuracy of the results, Method C is clearly to be preferred over Method E for this simple test-case.

Method F (see Section 2.3.3.2) is also relatively complex, but shows only a very weak dependence of hemolysis as function of the shear rate, in direct contradiction with the experiments. The overall order of magnitude is acceptable, and the prediction of Method F happens even to be the best of all for a shear rate of 600 s^{-1}, falling exactly on top of the measured value. However, the poor trend demonstrates that Method F will not perform well in general.

These first tests show that published models lead to considerably different predictions concerning hemolysis. At the lowest shear rate (250 s^{-1}), there is a factor of almost 20 between the lowest and the highest prediction. No model falls directly on top of the experimental points. Nevertheless, two of them show the right slope and are relatively close to the experimental measurements (underpredicting the results by a factor of 2 to 3, which should be considered as very good for such a complex process). The best model in this case is a relatively simple power-law model, Method C with the constants from Eq. (2.35). Very close to it lies a much more complex model, Method E. This first test is obviously not sufficient to generalize, and further comparisons are needed before choosing an optimal model category and model formulation. In particular, it is unclear yet how much physical complexity must be included in the model in order to obtain a good accuracy for a variety of different relevant conditions.

For practical CFD computations, and in particular when considering unsteady flows, Eulerian hemolysis models would be much easier to integrate into the flow solver, since all major flow solvers rely on an Eulerian description of the flow equations. However, as can be seen in Table 2.2, there is only one single published Eulerian model, Method A. As shown previously, Method A performed very poorly in the first test. This is why we decided to concentrate on an Eulerian version of the two best models, Method C and Method E, in what follows.

2.4.3 Open Questions

The first open question on the path toward an highly accurate model is the real relation between membrane strain and hemolysis, which could not be uniquely answered in the scientific literature up to now. As sketched in Fig. 2.25, Relations $A/B/C/D$ are currently available in the scientific literature, but an essential link is missing, shown as ?, for which no publication can be found. An alternative solution for relation "?" might be to derive it indirectly from C and D. However, this might induce large uncertainties.

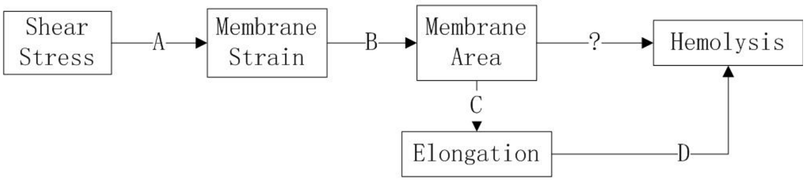

Figure 2.25: Clear and unclear relationships between shear and hemolysis in the published scientific literature

When trying to progress toward a better model, more and more questions are found on the way. Can strain be assumed to be distributed equally distributed over the RBC membrane? If not, is it possible to average, or should a statistical approach (Probability Density Function) be included? What is the exact influence of membrane harding on hemolysis? Are lung and body circulation of RBC sufficient to relax membrane hardening before rejoining again the pump? What is the impact of RBC diffusion, leading to non-homogeneous concentrations, and thus to RBC depletion in high-shear regions? What are the proper diffusion coefficients for real human blood (all existing results in the literature are based on diluted blood and/or the solvent is not real plasma)? The impact of heat transfer on hemolysis should also be quantified. For this, the cooling potential of blood in the human body needs to be determined.

Finally, when developing improved hemolysis models, it must be kept in mind that those models should be compatible with CFD (or they will be useless for this project). And the largest problem is certainly the missing reference experiments, with a proper description of process parameters and boundary conditions, deeply needed to validate such models.

2.4.4 Toward a Strain-based Eulerian Model

As explained previously, Eulerian hemolysis models are much more suitable for coupling with CFD, in particular when considering unsteady flows as found in a real rotary blood pump. Additionally, strain-based models are more complex but also open the door for a more accurate and general description of hemolysis in realistic flows. Therefore, an Eulerian strain-based model would combine both advantages, but has unfortunately never been published in the scientific literature yet (Table 2.2). Such a model should if possible include following features:

1. Account for membrane hardening: In the 120-day life circle of a RBC, each cell will pass the blood pump for 200 000 times. If the average residence time in the blood pump is assumed to be 0.05 s, then the total residence time in the blood pump during life cycle is more than 2 hours. For such a duration, it is well possible that membrane hardening plays a noticeable role;

2. Account for accumulation of strain in the membrane;

3. Account for relaxation of membrane strain if shear stress is reduced from a former high value.

Ideally, further improvements would be:

1. Account also for shear-induced RBC diffusion: the non-homogeneous concentration of RBC due to diffusion may greatly impact hemolysis. This might explain the over-prediction of most existing hemolysis models in commercial blood pumps;

2. Account for hemolysis induced by heating: the heat generation in a blood pump with an hydraulic efficiency of 60% is about 70 W, which might have a non-negligible impact on hemolysis.

The Lagrangian strain-based hemolysis model from Arora (see Section 2.3.3.1) has the potential to be modified into an Eulerian strain-based model. Being derived from Method E, the new model would be called E_E in what follows.

When Eq. (2.39) is transformed into an Eulerian formulation, the corresponding equation to Eq. (2.46) becomes:

$$\begin{aligned}\frac{\partial S_n}{\partial t} + (\mathbf{v}.\nabla)S = {} & -f_1\left[S_n - \frac{0.5((\mathrm{tr}(S_n))^2 - \mathrm{tr}(S_n^2))}{\det(S_n)}I\right] \\ & + f_2[\tilde{\varepsilon}.S_n + S_n.\tilde{\varepsilon}] + f_3[\tilde{W}.S_n + S_n.\tilde{W}] \\ & + \left[(\mathrm{eigv}(S_n))\frac{\partial(\mathrm{eigv}(S_n))}{\partial t} + (\mathbf{v}.\nabla)\mathrm{eigv}(S_n)\right].S_n \\ & + S_n.\left[(\mathbf{v}.\nabla)\mathrm{eigv}(S_n) + (\mathrm{eigv}(S_n))\frac{\partial(\mathrm{eigv}(S_n))}{\partial t}\right]\end{aligned} \tag{2.53}$$

Inserting Eq. (2.40) into Eq. (2.53):

$$
\begin{aligned}
\frac{\partial S_n}{\partial t} + (\mathbf{v}.\nabla)S = -f_1 &\left[S_n - \frac{0.5((\mathrm{tr}(S_n))^2 - \mathrm{tr}(S_n^2))}{\det(S_n)} I\right] \\
&+ f_2[\tilde{\varepsilon}.S_n + S_n.\tilde{\varepsilon}] \\
&+ f_3 \left[(W - (\mathrm{eigv}(S_n))\frac{\partial(\mathrm{eigv}(S_n))}{\partial t} + (\mathbf{v}.\nabla)\mathrm{eigv}(S_n)).S_n\right. \\
&\left.+ S_n.(W - (\mathrm{eigv}(S_n))\frac{\partial(\mathrm{eigv}(S_n))}{\partial t} + (\mathbf{v}.\nabla)\mathrm{eigv}(S_n))\right] \\
&+ \left[(\mathrm{eigv}(S_n))\frac{\partial(\mathrm{eigv}(S_n))}{\partial t} + (\mathbf{v}.\nabla)\mathrm{eigv}(S_n)\right].S_n \\
&+ S_n.\left[(\mathbf{v}.\nabla)\mathrm{eigv}(S_n) + (\mathrm{eigv}(S_n))\frac{\partial(\mathrm{eigv}(S_n))}{\partial t}\right]
\end{aligned}
\tag{2.54}
$$

This last equation can be then recast into its final form:

$$
\begin{aligned}
\frac{\partial S_n}{\partial t} &+ (1 - f_3)\mathrm{eigv}(S_n).\frac{\partial(\mathrm{eigv}(S_n))}{\partial t}.S_n \\
&+ (1 - f_3)S_n.\mathrm{eigv}(S_n).\frac{\partial(\mathrm{eigv}(S_n))}{\partial t} \\
&+ (\mathbf{v}.\nabla)S_n + (1 - f_3)\mathrm{eigv}(S_n).(\mathbf{v}.\nabla)\mathrm{eigv}(S_n).S_n \\
&+ (1 - f_3)S_n.\mathrm{eigv}(S_n).(\mathbf{v}.\nabla)\mathrm{eigv}(S_n) \\
&= f_1 \left[S_n - \frac{0.5((\mathrm{tr}(S_n))^2 - \mathrm{tr}(S_n^2))}{\det(S_n)} I\right] \\
&+ f_2\left[\varepsilon(\mathbf{v}).S_n + S_n.\varepsilon(\mathbf{v})\right] + f_3\left[W(\mathbf{v}).S_n + S_n.W(\mathbf{v})\right]
\end{aligned}
\tag{2.55}
$$

Equation (2.55) includes the inner-product of three transported tensor-related items eigv(S), $\partial(\mathrm{eigv}(S))/\partial t$ and S in the time-derivative, diffusion and convection terms. By these operations, the nine elements of the deformation tensor S are no longer formulated in a segregated manner. Unfortunately, such an element-coupled tensor transport equation cannot be implemented in any commercial flow solver. It is also not supported in the currently available versions of the open-source CFD code OpenFOAM, even if OpenFOAM appears as the best candidate for coding this equation in a future version.

In order to be compatible with the current requirements for OpenFOAM, one possible simplification would be to approximate in an explicit manner the time derivative term, releasing the condition on the inner product:

$$
\frac{\partial(\mathrm{eigv}(S_n))}{\partial t} = \frac{\mathrm{eigv}(S_{n-1}) - \mathrm{eigv}(S_{n-2})}{\triangle t} \tag{2.56}
$$

However, this would obviously strongly impact the stability and accuracy of the estimation. Therefore, the only acceptable solution seems to be a very deep-level implementation of model E_E in OpenFOAM. This could not be achieved before end of this Thesis, and is left for future projects.

2.4.5 An Eulerian Formulation of Model C

As a practical alternative, an Eulerian formulation of Model C has been derived in this project. Depending on the original version, it might be very complex or even impossible in practice to develop an Eulerian formulation based on an originally Lagrangian model. Fortunately, this is not the case for Method C, which can be relatively simply rewritten in an Eulerian framework. For this purpose, Eqs. (2.33) and (2.34) are directly rewritten in an Eulerian form:

$$\frac{\partial D_b}{\partial t} + (\mathbf{v}.\nabla) D_b = \tau^{b/a} \tag{2.57}$$

$$\frac{\partial H_L}{\partial t} + (\mathbf{v}.\nabla) H_L = a\,c\,D_b^{a-1} \tau^{b/a} \tag{2.58}$$

The obtained model, being directly derived from Method C, is denoted C_E in what follows.

The resulting transport equations are similar to any flow conservation equation and can be immediately coded in any standard CFD solver. For the following comparisons, theses equations have been implemented in Ansys® Fluent using User-Defined Functions (UDF). Equation (2.16) has been retained to compute τ.

Experimental measurements involving three cannulas with different inner tube diameters (Fig.2.26, [79]) are now used for comparing further the two only available Eulerian models, Method A and C_E. This is a much more complex validation step since it involves now a realistic flow configuration, relevant for practical purposes. All flow simulations in this section rely on Ansys® Fluent, using an axis-symmetrical setup. The boundary conditions for CFD are set following [80]. The three different cannulas are simulated with the same inlet flow rate, outlet (right boundary) flow rate, and inner tube reversed flow rate.

Note that this configuration is particularly challenging, since CFD reveals that Case 13G has the lowest peak value for τ, but the highest average value; while the opposite is observed for Case 16G, with the highest peak but the lowest mean value for τ.

The numerical prediction of hemolysis obtained with Method A and Method C_E are compared in Table 2.4 with the experimental measurements from [79].

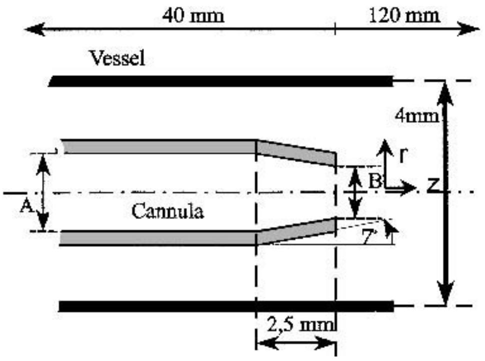

Figure 2.26: Geometrical configuration considered for the second validation step

Method A gives hemolysis values not too far from the experimental values concerning order of magnitude, but fails completely to predict the trend: while the hemolysis increases steadily from Case 13G to 14G to 16G, Method A predict a slightly decreasing level.

Method C_E can successfully predict the trend, but gives values much larger than the experimental values... By changing the value of constant c, Method C_E would be in principle able to give a much better fit to the experimental values. However, considering that fitting model parameters by comparison with a single experiment would be too limited, the default set of model parameters has been kept in the rest of this Thesis.

Case	A	B	$\triangle H_b/H_b$ Method A	$\triangle H_b/H_b$ Method C$_E$	$\triangle H_b/H_b$ Experimental
13G	1.105 mm	0.8 mm	7.06e-7	1.04e-5	7.35e-8
14G	0.955 mm	0.65 mm	5.13e-7	1.34e-5	2.55e-7
16G	0.725 mm	0.6 mm	5.10e-7	1.86e-5	4.35e-7

Table 2.4: Comparison of predicted and measured $\triangle H_b/H_b$ for the three cannulas (experimental measurements from [79])

2.5 Conclusions

As a whole, seven different hemolysis models from the literature and two derived formulations have been discussed and compared in this work, with the final objective of coupling one of those models with CFD computations of rotary blood pumps. All these models show specific advantages and drawbacks, and there is unfortunately no clear guidelines concerning applicability or limitation. An even worse problem is the lack of well-documented experimental data suitable for a final check of those models under realistic conditions.

Based on a first validation for a simple configuration, a Lagrangian power-law model (Method C) performs best, followed closely by a much more complex Lagrangian strain-based model (Method E). Considering that Eulerian models are more suitable for coupling with CFD simulations, corresponding formulations have been derived, leading to Methods C$_E$ and E$_E$. Unfortunately, the model with the highest potential in principle, model E$_E$ cannot be implemented easily into any existing CFD solver, due to the structure of the resulting equations. The results obtained with method C$_E$ show the right trend, but not the correct order of magnitude. This demonstrates that much more work is needed before obtaining an accurate, generally-applicable hemolysis model compatible with CFD: this will be left to future projects.

Concerning perspectives, the implementation of Method E$_E$ into the open-source software OpenFOAM should be pursued. Most important, **the need for further experiments concerning hemolysis under well-defined, reproducible and well-documented conditions is again highlighted**. This will be ultimately the only possibility to develop and validate models with a high level of generality and accuracy. Those experiments will hopefully also cast light on further open issues, in particular:

- importance of membrane hardening under shear stress;
- process leading to the release of membrane deformation when reducing shear stress;
- importance – or not – of RBC diffusion; if this is important, what are the proper diffusion coefficients?
- importance of hemolysis associated to heating, a point particularly important for blood pumps, which have currently a limited efficiency.

Since we have not been able in this Chapter to obtain a final answer concerning applicability and generality of all hemolysis models (there is no clear winner), the results discussed in the next chapters involve models A, B, and C$_E$.

CHAPTER 3

Numerical Simulation of the FDA's Test Cases

This chapter describes numerical investigations of the two test cases recently proposed by the US Food and Drug Administration (FDA) as part of the so-called "CFD Critical Path Initiative" project. The final purpose of this project is to determine if and how computational fluid dynamics can be effectively used to characterize fluid flow and to predict blood damage in medical devices. In case of a positive outcome of this project, CFD might be used as part of the official approval procedure by FDA. In any case, these two FDA challenges can be used as realistic benchmarks to evaluate CFD for hemodynamics and blood pumps.

3.1 FDA Test Case #1 (Hemodynamics): Blood Nozzle with Sudden Expansion

3.1.1 Introduction

The nozzle proposed by FDA shows an axis-symmetrical geometry and is shown in more details in Figs. 3.1 and 3.2. All details can be found in [94] and on the Website given in this article. The nozzle shows characteristics found in many medical devices that have blood flowing through them, including blood tubing, hemodialysis sets, catheters, cannulas, syringes, and hypodermic needles. It incorporates tubes of two diameters, with a cone connecting the two tubes on one end, and a sudden change in diameter on the other side. When the flow is going from left to right in Fig. 3.1 (the reference case), the blood flow thus encounters a sudden expansion. The configuration retained by FDA will deliver flow pathlines showing sudden accelerations and strong recirculations, both aspects considered to be very important in order to model blood damage in medical devices [94].

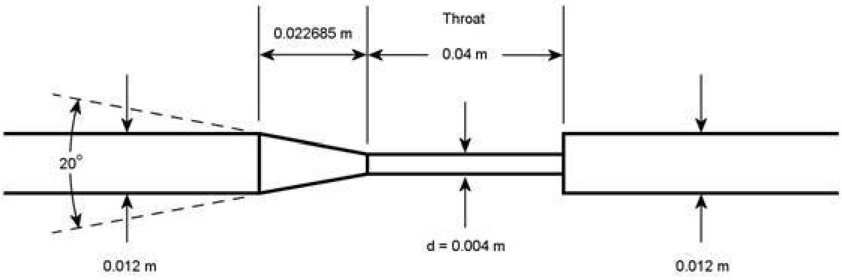

Figure 3.1: Blood nozzle: tube with sudden expansion

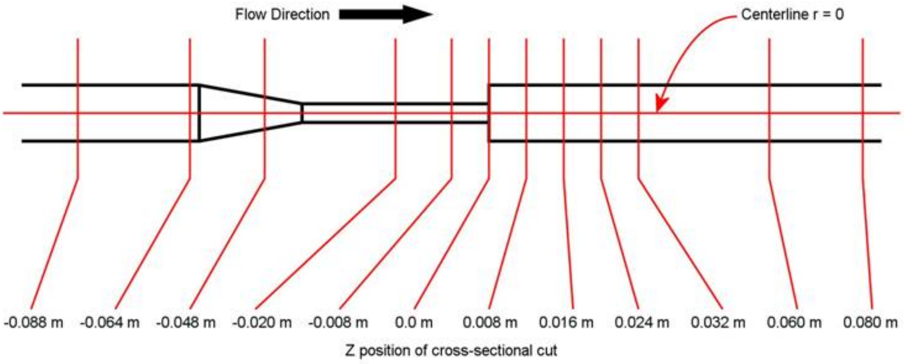

Figure 3.2: Defined axial positions along the tube

As prescribed by FDA, the CFD simulations are carried out for 5 different flow conditions with volume flow rates of $5.2\,10^{-6}$ m^3/s, $2.08\,10^{-5}$ m^3/s, $3.64\,10^{-5}$ m^3/s, $5.21\,10^{-5}$ m^3/s, and $6.77\,10^{-5}$ m^3/s, corresponding to five increasing Reynolds numbers of 500, 2000, 3500, 5000 and 6500 respectively, computed with the diameter of the smallest, central tube. Thus, depending on the case considered, laminar, transitional or mild turbulent conditions are expected in the system, which explains the difficulty of this case, as discussed in more details in [95].

3.1.2 Numerical Study

3.1.2.1 Grid

All quadrangular, 2D axis-symmetrical meshes have been constructed using ANSYS® ICEM-CFD. After checking mesh independency of the velocity fields, several regions have been locally refined. Two selected regions of the finally retained mesh are shown in Figs. 3.3 and 3.4. The final mesh includes altogether 1 159 247 quadrangles. The simulated domain is exactly twice as long as the given geometry show in Fig. 3.1, in order to minimize the influence of the boundary conditions employed at inlet and outlet (which are not prescribed further by FDA). On the inlet side, the extrusion is used to get a fully developed flow field at the entrance of the domain of interest. On the outlet side, extending the domain is necessary to avoid any flow reentry through the outlet.

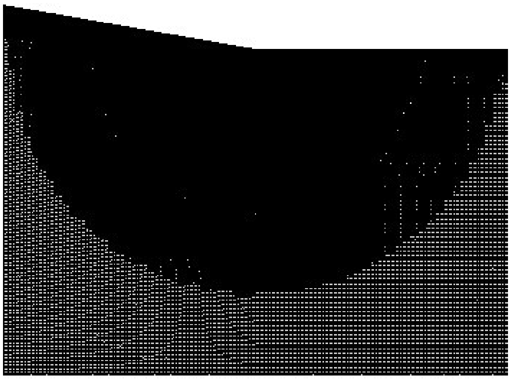

Figure 3.3: Zoom on the mesh in the entry region of the central tube (flow from left to right)

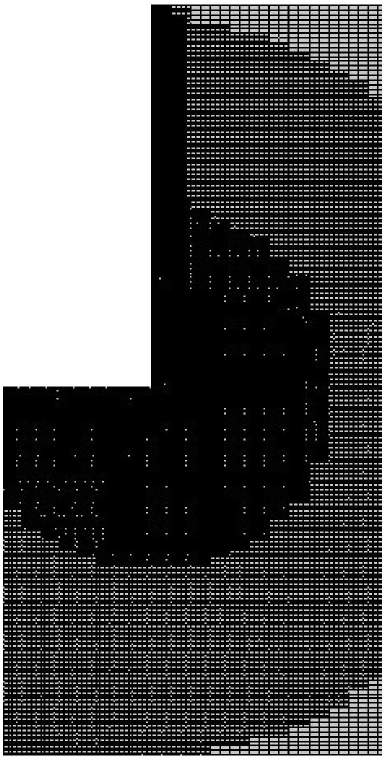

Figure 3.4: Zoom on the mesh at the end of the central tube (sudden expansion)

3.1.2.2 Settings of the Numerical Simulations

All simulations rely on ANSYS® Fluent using a 2D axis-symmetrical geometry. For all RANS (Reynolds-averaged Navier-Stokes) and RSM (Reynolds Stress model) turbulence models, steady flow conditions are prescribed. The further settings are listed in Table 3.1.

Density	1035 kg/m^3
Viscosity	0.0035 Pa.s
Inlet velocity profile	$V_{max}\sqrt{0.006 - x[1]}$ (y-direction)
Inlet turbulence intensity	0
Pressure-velocity coupling	SIMPLE
Outlet	Outflow

Table 3.1: Settings employed in Fluent

The impact of different turbulence models has been tested for the flow conditions corresponding to Re=5000. The velocities obtained at selected positions along the central line of the system are compared with experimental data given in [96], as discussed in the next section. The turbulence model leading to the best agreement with the experimental data is then employed for all further simulations.

Two hemolysis models discussed in the previous chapter have been coded into Fluent using User-Defined Functions (UDF). The corresponding lines of code can be found in Appendix D. The obtained results will be discussed as well in what follows.

3.1.3 Results

3.1.3.1 Impact of Turbulence Model

The comparison of velocity magnitude along the central axis of the device for Re=5000 is shown in Fig. 3.5. Two different, independently obtained sets of experimental measurements have been proposed by FDA, as discussed in [96]. From Fig. 3.5, it appears that the standard Reynolds-Stress Model (RSM) of Fluent with quadratic pressure-strain relation delivers the best overall agreement with the experimental data. A small region of the central tube around $x = -0.02$ is the only one for which noticeable differences are found between RSM and measurements, the rest of the prediction being in very good agreement with the experiments.

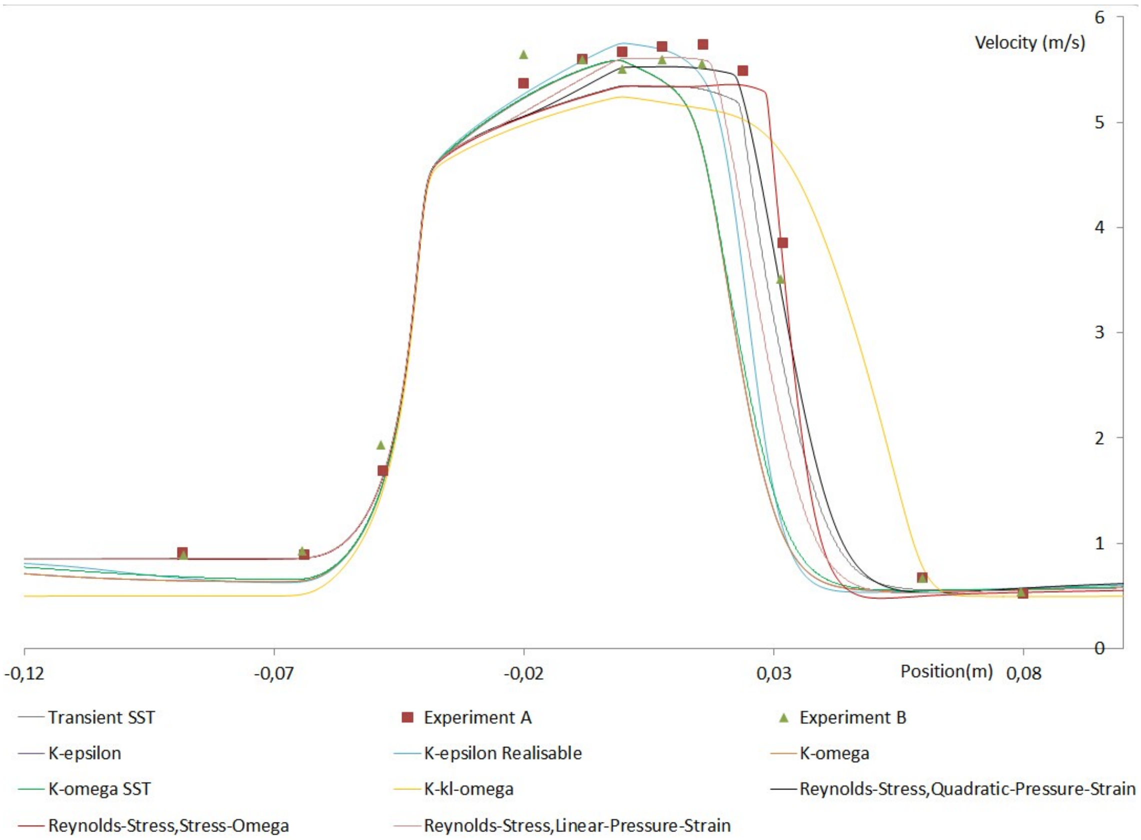

Figure 3.5: Velocity magnitude along central axis for Re=5000 as function of the turbulence model, compared to experimental data from [96]

Therefore, the further flow conditions corresponding to Re=500, 2000, 3500, 6500 have been simulated as well with the RSM model using a quadratic pressure-strain relation. The corresponding comparisons between our numerical results and the experimental data published by FDA are shown in Figs. 3.6 to 3.9. The agreement obtained for Re=2000 and Re=3500 is almost perfect. At the highest Reynolds number (Re=6500), the agreement is still very good, in spite of a slight underprediction of the peak velocity in the inner tube. For the laminar conditions (Re=500), the agreement is quite good until the sudden expansion; there, the two RSM versions (quadratic pressure-strain relation or stress-ω relation) lead to two widely different predictions that surround the measurements. Obviously, the recirculation zone and the reattachment region are difficult to predict using RSM for the laminar case.

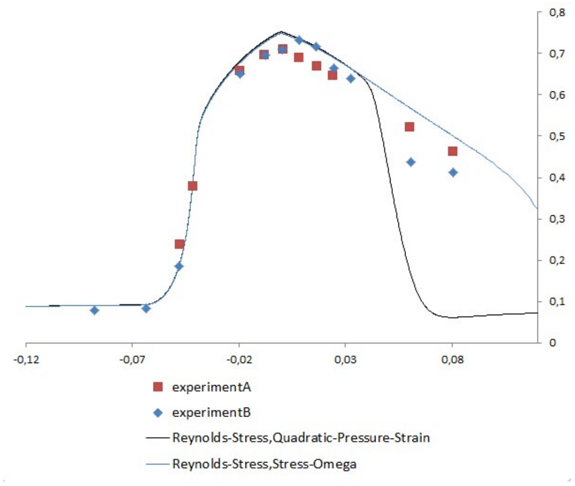

Figure 3.6: Velocity magnitude along central axis for Re=500 compared to experimental data from [96]

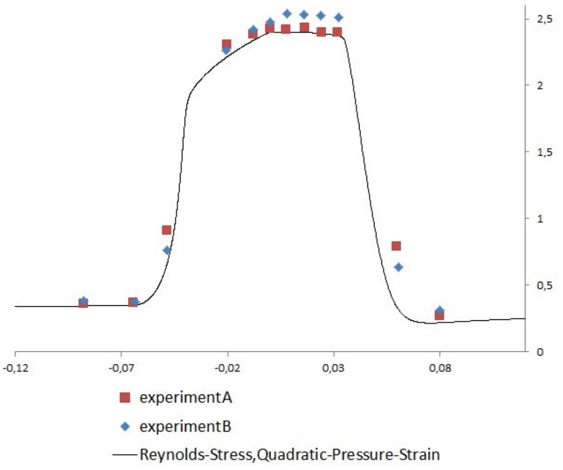

Figure 3.7: Velocity magnitude along central axis for Re=2000 compared to experimental data from [96]

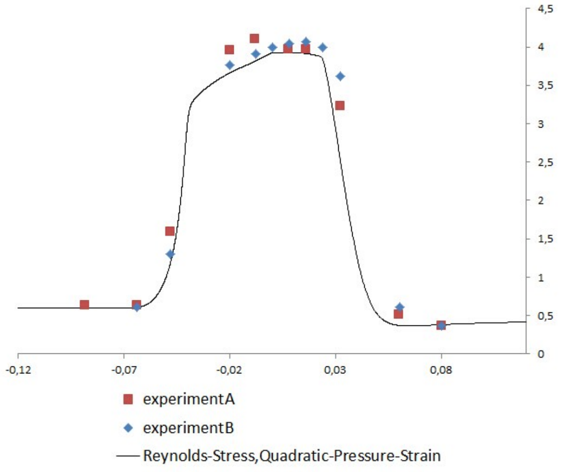

Figure 3.8: Velocity magnitude along central axis for Re=3500 compared to experimental data from [96]

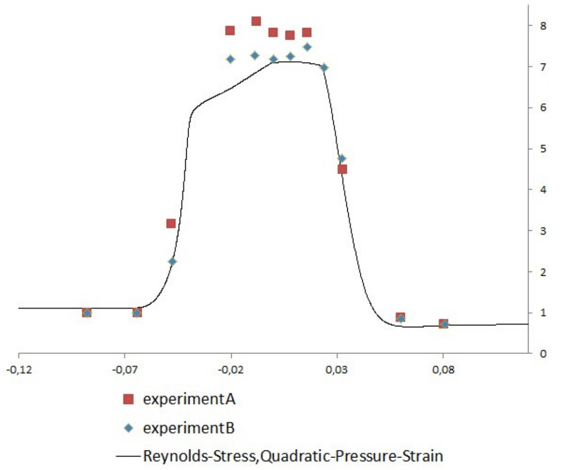

Figure 3.9: Velocity magnitude along central axis for Re=6500 compared to experimental data from [96]

3.1.3.2 Hemolysis

As explained in the previous chapter, it has been unfortunately impossible to identify an accurate, generally applicable hemolysis model compatible with CFD. Therefore, hemolysis is now calculated using two different models, in order to get an idea of the underlying variability. Both model A (see Section 2.3.2.1) and our own, Eulerian formulation of model C, called model C$_E$ (see Section 2.4.5) have been employed. The obtained predictions are compared in Table 3.2.

Re	$\triangle H_b/H_b$ Model A	$\triangle H_b/H_b$ Model C$_E$
500	$2.83\,10^{-8}$	$9.52\,10^{-9}$
2000	$4.18\,10^{-8}$	$8.21\,10^{-6}$
3500	$1.40\,10^{-7}$	$3.03\,10^{-5}$
5000	$3.03\,10^{-7}$	$5.63\,10^{-5}$
6500	$5.61\,10^{-7}$	$1.41\,10^{-4}$

Table 3.2: Prediction of hemolysis $\triangle H_b/H_b$ in the FDA blood nozzle obtained by models A and C$_E$ at different Reynolds numbers

3.1.4 Final Comments and Discussion Concerning the FDA Blood Nozzle

Based on the presented results and on many further simulations involving RANS turbulence models and Large-Eddy Simulations, not shown in the interest of space, first conclusions can be drawn concerning turbulence modeling:

- The standard Reynolds-stress models implemented in Fluent show the best agreement with the experimental data. This is particularly true at axial (x) positions larger than 0 m and smaller than -0.04 m (see Fig. 3.2). The worst agreement is always obtained within and just after the conical section joining the larger tube with the smaller, inner tube.

- According to theory, the RSM model with quadratic-pressure-strain relation should show a superior performance for axis-symmetric expansions/contractions [97], explaining why it works particularly well here. In the entry region, all RSM models perform equally well. But, after entering the smaller, central tube, the RSM model with quadratic-pressure-strain relation shows a noticeably better agreement.

- However, for the laminar case (Re=500), the RSM Stress-ω model shows a better performance than the RSM quadratic-pressure-strain model just after the sudden expansion.

- Numerical simulations with RSM models are often associated with convergence problems, far more so than with RANS turbulence models. The only solution is to reduce the Max Coarsening Levels and to increase the Sweeps (both are numerical options in Fluent).

- Many tests with a variety of RANS models show that the k–ϵ–RNG model performs best for this configuration. The obtained agreement with experimental data is only slightly worse than for the RSM model with quadratic-pressure-strain relation. It is even better than the RSM model in the axial region between -0.04 and 0 m.

- In collaboration with Prof. G. Janiga, an extensive study has been carried out for this case involving Large-Eddy Simulations. The results are documented in [95], and prove that LES can be used to simulate with a high accuracy – but unfortunately also with a high computational cost – this configuration. One exemplary result is shown in Fig. 3.10.

Let us now summarize some preliminary findings concerning hemolysis:

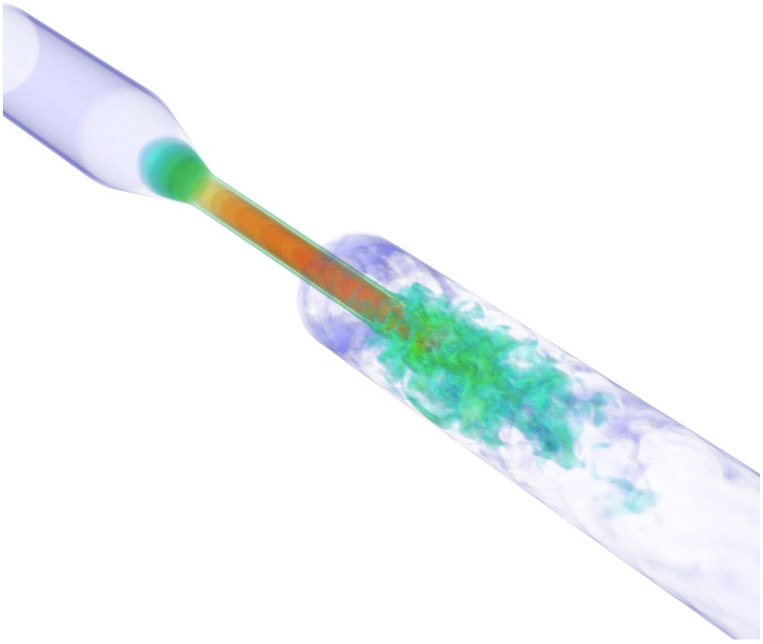

Figure 3.10: Volume rendering of the instantaneous velocity magnitude obtained by Large-Eddy Simulation; further details can be found in [95]

- Model C_E gives larger differences in hemolysis, $\triangle H_b/H_b$, between the different flow conditions (different values of Re), compared to model A. This confirms the hemolysis predictions in Section 2.4.5, where $\triangle H_b/H_b$ with model C varies much more considerably than with model A. Since the actual FDA experiment involves an artificial substitute instead of real blood, a more detailed validation is – unfortunately – not possible.

- Following FDA's requirement, a constant viscosity value has been used in the above simulations. Using in a further test a non-Newtonian Carreau viscosity model (Eq. 3.1) with constants listed in Table 3.3, noticeable differences are observed in the velocity field, and, consequently, in the resulting hemolysis values. Since hemolysis models are very sensitive to large shear stress values, and remembering that a non-Newtonian model may significantly reduce peak values of shear stress, such differences are not surprising.

$$\eta = \eta_\infty + (\eta_0 - \eta_\infty)(1 + \gamma^2\lambda^2)^{(n-1)/2} \tag{3.1}$$

Time Constant, λ (s)	8.2
Power-Law Index, n	0.21
Zero Shear Viscosity (Pa.s)	0.16
Infinite Shear Viscosity (Pa.s)	0.0035

Table 3.3: Values employed for blood modeled with a Carreau model

Finally, all further fields required by the FDA in order to participate into the contest for the Blood Nozzle are shown in Appendix A.

3.2 FDA Test Case #2: Blood Pump

3.2.1 Introduction

The FDA blood pump features a very simple centrifugal type, with straight blades and a volute of constant diameter, as shown in Fig. 3.11. The rotor itself is half covered by a disk of large thickness in opposite direction to the inlet. Four very simple straight blades of large thickness and relatively small chordwise depth constitute the impeller. Both the disk and the blades are polished along edges and corners. Finally, the setup involves unusually long inlet and outlet pipes.

According to FDA, this blood pump model is highly relevant for several blood pump designs currently being developed as part of the NIH Pediatric Circulatory Support initiative. This is the reason why this unusual geometry has been retained for the case study.

Six different flow conditions must be numerically investigated, as a combination of four different flow rates and two rotating speeds. The transport media is to be considered as a liquid with constant density (1035 kg/m^3) and constant dynamic viscosity 0.0035 Pa.s (3.5 cP).

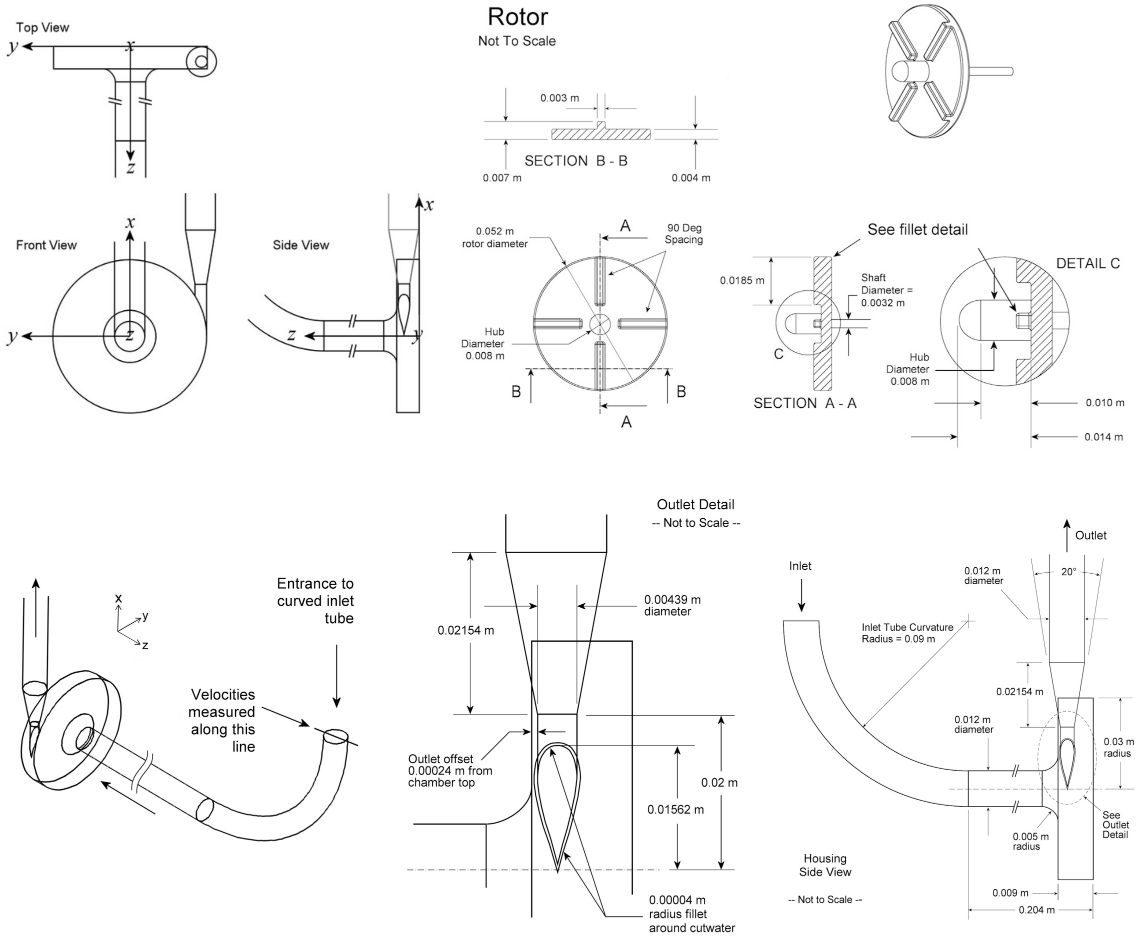

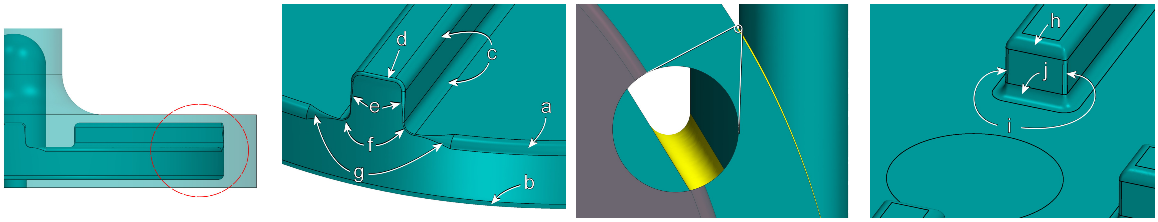

Figure 3.11: Selected details of the geometry of the FDA blood pump, see also https://fdacfd.nci.nih.gov/

3.2.2 Numerical Study

3.2.2.1 Grid

After a grid-independence study concerning the obtained velocity fields, a fully hexahedral mesh with 10 086 367 elements has been generated thanks to Ansys® IcemCFD. It involves nine segments (see Fig. 3.12) with nonidentical surface meshes along the connecting interfaces. The number of elements in the different segments is listed in Table 3.13. The interface between the rotating part and the stationary part is placed at the arithmetical middle in diametrical distance between the volute shell and the span-end of the rotor.

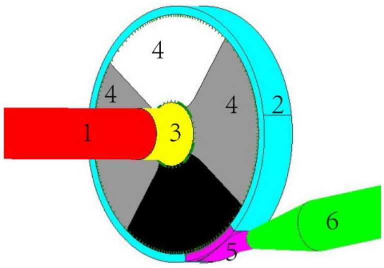

Figure 3.12: Mesh segments

Region	Mesh Size
1	60 345
2	671 814
3	38 817
4	2 028 860(×4)
5	959 886
6	240 065

Figure 3.13: Mesh size of the different regions

Figures 3.14 to 3.17 show zooms on selected regions of the mesh.

3.2.2.2 Numerical Simulation

The approach called GGI (General Grid Interface) is used in Ansys®CFX to connect the different grid parts, between rotating and stationary zone.

A desktop PC with 32 GB memory and Intel® Core i7-4930K processor (6-core, 3.4 GHz, 12 MB-cache) is used to carry out the numerical simulation. The CFD solver CFX runs with single precision (in order to get a higher speed-up), and the memory allocation factor is set to 1.2. The total system memory consumption is around 23 GB, with approximately 2 GB occupied by the Windows 7 (x64) operating system.

The reference flow condition with a flow rate of 6 L/min and a rotation speed of 3500 rpm is first computed. It is initiated with a laminar flow model for the first two rotations. Then, the resulting solution is mapped to the RNG k–ϵ turbulence model with scalable wall function, found to be best of all RANS models in the previous section. The settings employed in the CFD simulation relying on CFX are listed in Table 5.2.

The simulation is finally stopped after computing a total of 12 rotations; at this point, a fully periodic steady state is observed concerning pump pressure head. The employed timestep size is 1/200 of one rotation, and the residual target is set to 0.0005 (RMS). For

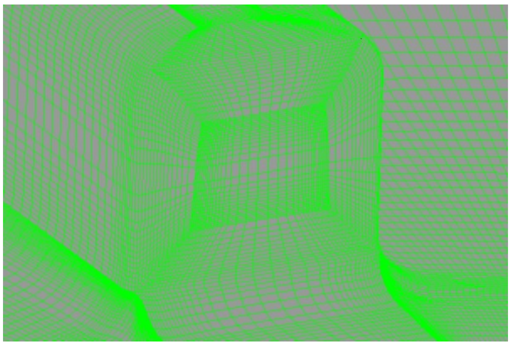

Figure 3.14: Mesh at beginning of blade

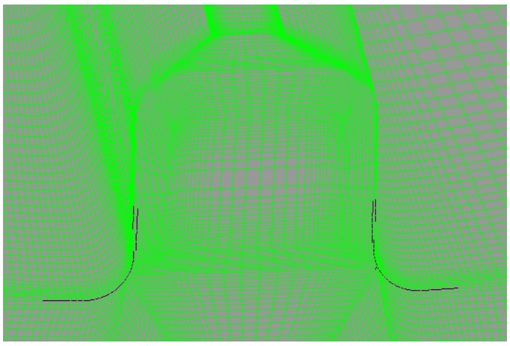

Figure 3.15: Mesh at end of blade

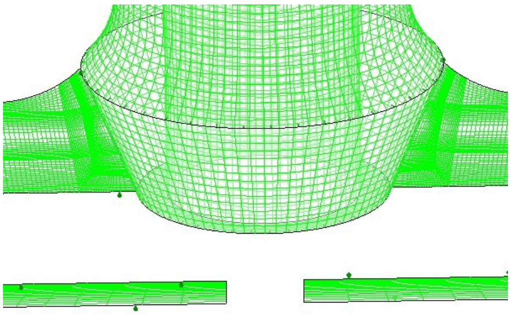

Figure 3.16: Mesh at rotor inlet

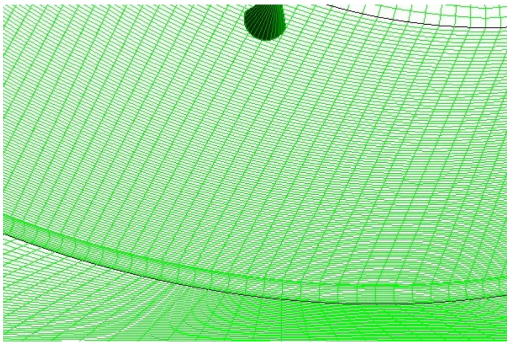

Figure 3.17: Mesh at cut water

other flow conditions, this converged solution is used to start the corresponding simulation. Then, 5 to 10 rotations are needed to obtain a periodically repeating pressure head, and the time step size is set to 1/100 of one full rotation.

Density	1035 kg/m^3
Viscosity	0.0035 Pa.s
Turbulence Model	RNG k–ϵ
Inlet velocity profile	$V_{max}(1-(r/R_{max}))^{1/n}$, n=3 @ 2.5, 4 @ 4.5, 5 @ 6&7 L/min
Inlet turbulence Intensity	4% to 7%, as prescribed by FDA for each case
Convergence Criteria	RMS 0.00005
Outlet	Open
Min. Coeff. Loops	1
Max. Coeff. Loops	10
Timestep size (s)	$1.71\,10^{-4}$ (@3500rpm), $2.4\,10^{-4}$ (@2500rpm)

Table 3.4: Settings of CFX for the CFD simulation of the FDA pump

3.2.3 Results

3.2.3.1 Flow Field

Figure 3.18 is a plot of pressure head versus time for the reference flow condition (6 L/min at 3500 rpm). An almost periodic pattern is observed already after 8 rotations. However, a truly periodic repetition (less than 5% difference) is first observed after 12 rotations, which is perhaps a consequence of turbulence.

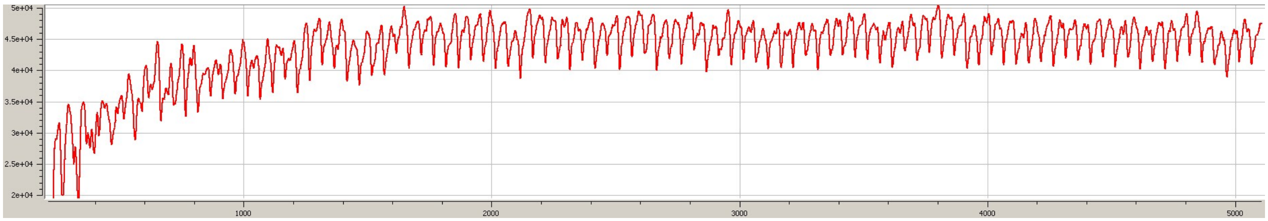

Figure 3.18: Instantaneous pump pressure head vs. time

Table 3.5 summarizes the most important parameters and the results asked for by FDA for the simulation of the six different flow conditions as prescribed by FDA.

Flow rate (L/min)	2.5	2.5	4.5	6.0	6.0	7.0
Pump speed (rpm)	2500	3500	3500	2500	3500	3500
Timestep size (s)	$2.40\,10^{-4}$	$1.71\,10^{-4}$	$1.71\,10^{-4}$	$2.40\,10^{-4}$	$8.57\,10^{-5}$	$1.71\,10^{-4}$
Pressure Head (Pa), averaged over last full rotation	21 920	53 160	49 732	8 740	44 481	41 261
Time-averaged maximum wall shear stress (Pa) over the housing rim, averaged over last full rotation	$1.38\,10^{2}$	$1.99\,10^{2}$	$1.78\,10^{2}$	$1.08\,10^{2}$	$1.15\,10^{2}$	$1.31\,10^{2}$
Time-averaged maximum wall shear stress magnitude (Pa) over the entire outlet fillet, averaged over last full rotation	$1.42\,10^{2}$	$2.88\,10^{2}$	$1.83\,10^{2}$	$2.65\,10^{2}$	$2.55\,10^{2}$	$3.84\,10^{2}$
Time-averaged shaft torque (Nm), averaged over last full rotation	$1.01\,10^{-2}$	$1.63\,10^{-2}$	$2.30\,10^{-2}$	$1.86\,10^{-2}$	$2.80\,10^{-2}$	$3.16\,10^{-2}$
Hemolysis rate $\triangle H_b/H_b$ obtained from model C_E	0.0073	0.0085	0.0034	0.00062	0.0025	0.0014

Table 3.5: Detailed CFD settings and main results for the six different conditions prescribed by FDA

3.2.3.2 Hemolysis

The hemolysis rate predicted by the simulation using model C_E (see Section 2.4.5) is given as well in Table 3.5. The FDA has communicated that experimental data will be published concerning the really observed hemolysis in this configuration. Unfortunately, at the time when this Thesis has been submitted (early January 2015), such data sets are not available yet. Therefore, a comparison – and hence a validation – is not possible at that time.

3.2.4 Final Comments and Discussion Concerning the FDA Blood Pump

Keeping in mind that the FDA will publish experimental results concerning this blood pump, but that those results are not available yet, first conclusions can only rely on the obtained CFD results. From the computational results obtained for the six working conditions, following conclusions can be drawn:

- Considering the four flow conditions with the same rotation speed (3500 rpm), the pressure head decreases when the flow rate increases, which is logical for the shape of a typical characteristic pump curve. The same situation is also observed for the two conditions with a rotation speed of 2500 rpm. This is a first indication that the obtained results are physically sound.
- Due to the unusual (very simple) design of the impeller, large oscillations in pressure head are observed, even after many full rotations. A truly stable, periodical evolution of the pressure head can only be obtained with a much coarser grid (4 million grid cells and less), associated to a much higher level of numerical diffusion. The values listed in Table 3.5 are cycle-averaged values.
- For this particular geometry, it was impossible to obtain converged results with the standard k–ϵ and k–ω-models. Only the realizable k–ϵ, RNG-k–ϵ and SAS-SST models converged. From the latter models, SAS-SST requires a noticeably longer computational time, so that RNG-k–ϵ was finally retained as a reference.
- All further fields required by the FDA in order to participate into the contest are shown in Appendix B.

3.3 Conclusion

Even if a proper validation could not be achieved yet due to missing experimental data, it appears that CFD is able to reproduce with a satisfactory accuracy hemodynamic fields in practically relevant geometries and configurations. This opens the door for a possible optimization of practical blood pumps using CFD-O, as will be considered next.

Chapter 4

Design Optimization Method for Blood Pumps

4.1 Literature Review

4.1.1 Pump

An hydraulic pump is a machine used to move a liquid through a piping system and to raise the pressure of the liquid. Looking at the rotor outflow direction, a rotary pump can be classified into three groups: centrifugal pumps (as an example, see Fig. 4.1), axial-flow pumps (Fig. 4.2); and mixed flow pumps, as a compromise between both designs.

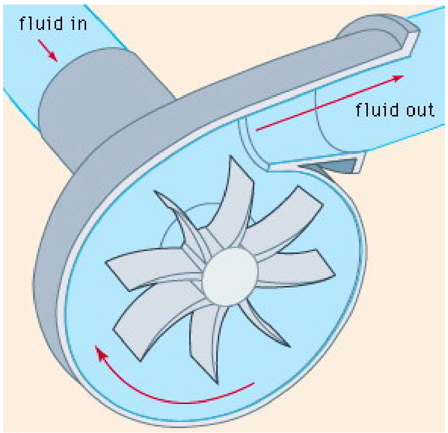

Figure 4.1: Example of a centrifugal pump, from [98]

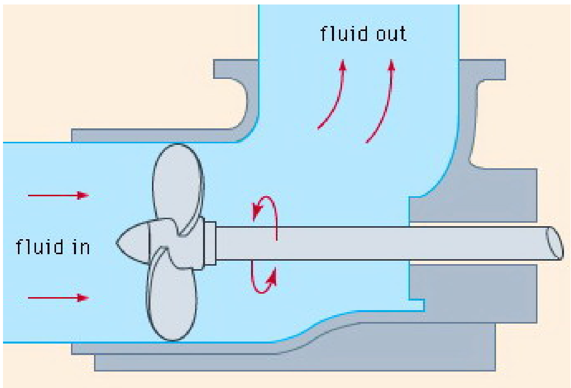

Figure 4.2: Example of an axial-flow pump, from [98]

The energy conversion in a pump takes place in the impeller, in which the input energy is converted into mechanical energy. First, the rotating impeller causes the liquid that has entered the pump to accelerate, raising the kinetic energy of the liquid. The vanes in a rotary pump are often curved backward to the direction of rotation. When the liquid leaves the impeller vane outlet tip, it is at its maximum velocity. Figure 4.3 illustrates typical velocity and pressure changes in a rotary pump as the liquid moves through the pump. After the liquid leaves the impeller tip, it enters the outlet region. The outlet region design ensures that the cross-sectional area of the flow passage increases in direction of liquid movement. Because of this, a diffusion process occurs, causing the liquid velocity to decrease. In agreement with the Bernoulli equation, the decreased kinetic energy is transformed into increased pressure energy.

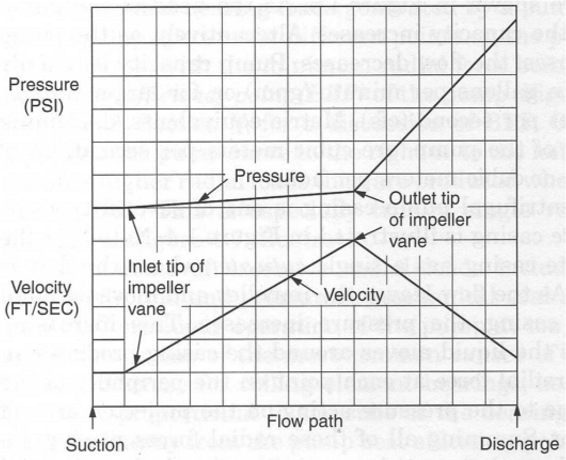

Figure 4.3: Typical velocity and pressure evolution along the flow path in a pump [99]

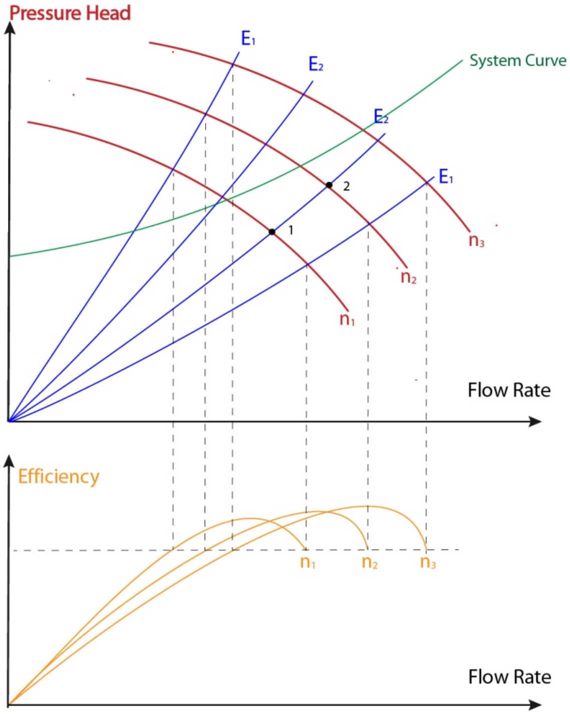

Figure 4.4: Typical characteristic curve of a pump [99]

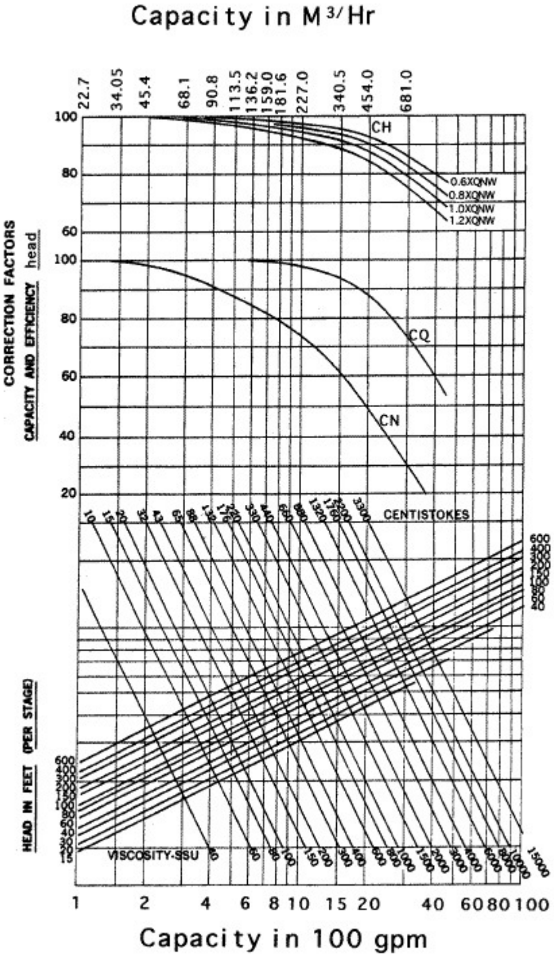

Figure 4.5: Performance correction chart for viscosity [99]

A centrifugal pump operating at a given rotation speed and with a given impeller diameter produces a differential pressure, or differential head. While all terms in the Bernoulli equation are expressed in specific energy units (J/kg), this equation is in practice very often converted to height units (m) by dividing the whole equation by gravity acceleration g. Then, the resulting head is finally expressed in meters (or feet in english-speaking countries). The amount of head produced varies with the flow rate, as illustrated by the characteristic head-flow rate curve (also called H-Q curve, connecting the head H to the flow rate Q or $\dot{q}$). Such H-Q curves are shown in red in Fig. 4.4. As the flow rate increases, the head of the pump decreases. Increasing the rotating speed of a pump, will move the H-Q curve towards higher values, as shown in Fig. 4.4 for three increasing values of the rotating speed ($n_3 > n_2 > n_1$). Increasing the rotating speed will also typically move the efficiency curve to the right, as the orange curves illustrate.

A point on a H-Q curve is called an operation point. It represents a certain combination of flow rate and pressure head for a certain rotating speed. If different operation points on different H-Q curves share the same efficiency, they are called similar operation points. Connecting similar operation points will deliver the equal-efficiency curves shown in blue in Fig. 4.4. Equal-efficiency curves in the central region correspond to higher efficiencies, $E_2 > E_1$.

The system curve is a graphical representation of the head requirement of the external system connected to the pump. It usually consists of a combination of static and frictional components. The static head does not vary with flow velocity, while the frictional head varies quadratically with flow velocity. The intersection of the system curve and of the pump (H-Q) curve indicates the real working condition of the pump interacting with the system. This working condition is stable when and only when the product of the two derivatives of the two curves is negative at the intersection point, as is the case in Fig. 4.4.

Pressure head and flow rate of two points (for instance, point 1 and point 2 in Fig. 4.4) on the same equal-efficiency curve follow the so-called Affinity Law described by the relationships in Eqs. (4.1) and (4.2):

$$\frac{Q_2}{Q_1} = \frac{n_2}{n_1} \tag{4.1}$$

$$\frac{H_2}{H_1} = \left(\frac{n_2}{n_1}\right)^2 \tag{4.2}$$

If a rotary pump is being considered for pumping a viscous liquid other than water, the pump performance curve obtained with water must be adjusted to take into account the impact of a different viscosity. In general, pumping a viscous liquid with viscosity higher than water causes a corresponding reduction in both head and capacity. Correction factors for pressure head and flow rate are given in Eqs. (4.3) and (4.4):

$$C_H = \frac{H_{visco}}{H_{water}} \tag{4.3}$$

$$C_Q = \frac{Q_{visco}}{Q_{water}} \tag{4.4}$$

The relation between C_H, C_Q, H, Q, and viscosity is shown in Fig. 4.5.

4.1.2 Design Theory for Axial-flow Pump

A typical pump design process begins with the Specific Speed, N_q, used by pump designers:

$$N_q = \frac{nQ^{1/2}}{H^{3/4}} \tag{4.5}$$

In this equation, the flow rate Q is normalized by a reference flow rate of 1 m^3/s and the head is normalized by 1 m. For this reason, the unit of N_q is the same as the unit of n, either 1/s or very commonly 1/min. The first use of N_q is to classify the pump impeller concerning type and proportions. Table 4.1 shows empirical data relating pump type and N_q, based on decades of past experience and leading to a good hydraulic efficiency [100].

Type of Impeller	N_q in 1/min	Impeller outlet diameter/Inlet diameter
Slow speed radial flow	10-30	3.5-2
Standard speed radial flow	30-50	2-1.5
High speed radial flow	50-80	1.5-1.3
Mixed flow	80-160	1.2-1.1
Axial flow	110-500	1.0

Table 4.1: Typical relation between N_q and impeller shape based on experience [99]

If a specific pump type is decided in advance by the application or due to geometrical limitations, then n can be estimated knowing N_q, Q and H by inverting Eq. (4.5), as shown later in Eq. (4.22).

The axial velocity c_A is then determined by n and Q when assuming a given inlet blade angle β (see Eq. 4.23), which will be recalculated and improved in later steps. For an axial-flow pump, N_q also empirically decides the ratio of d/D, as shown in Table 4.2. Finally, after c_A, n and d/D have been determined, d and D can be calculated separately from Eqs. (4.24), (4.25) and (4.26).

N_q	140	150	165	220
d/D	0.6	0.55	0.5	0.4

Table 4.2: Optimal relation between N_q and diameter ratio based on experience [101]

The next step is to decide the shape of the impeller blades, especially the outlet angles. This task is fulfilled by analyzing the velocity triangle at the impeller outlet axial plane. Figure 4.6 shows the velocity triangles at different axial positions along an axial-flow pump. First neglecting the thickness of the blades, the axial velocity c_0 does not change through the pump (conservation of flow rate in the steady system). The blade angles at impeller outlet determine the local absolute velocity of the flow, which is directly related to its kinetic energy.

Equation (4.6) is the basic equation delivering the theoretical pressure head (in m) for the impeller. The head is composed of the pressure rise $(p_{p\infty} - p_0)/\rho g$ generated within the impeller, and of the kinetic energy rise $(c_2^2 - c_1^2)/2g$, which is to be converted partly into pressure rise later in the outlet vane/diffuser.

$$H_{th} = \frac{p_{p\infty} - p_0}{\rho g} + \frac{c_2^2 - c_1^2}{2g} \tag{4.6}$$

The pressure head equation for the whole pump is thus derived using following steps, considering now a centrifugal pump as an example (this procedure can obviously be adapted as well to an axial pump, as done later).

First looking at Fig. 4.7 in region (a), the centrifugal force balance equation reads $dfdp = dfdr\rho r\omega^2$ along the tangential direction and generates a pressure rise of $dp = \rho\omega^2 r dr$ N/m^2, which can be rewritten as:

$$\frac{dp}{\rho} = \omega^2 r dr = dY' \tag{4.7}$$

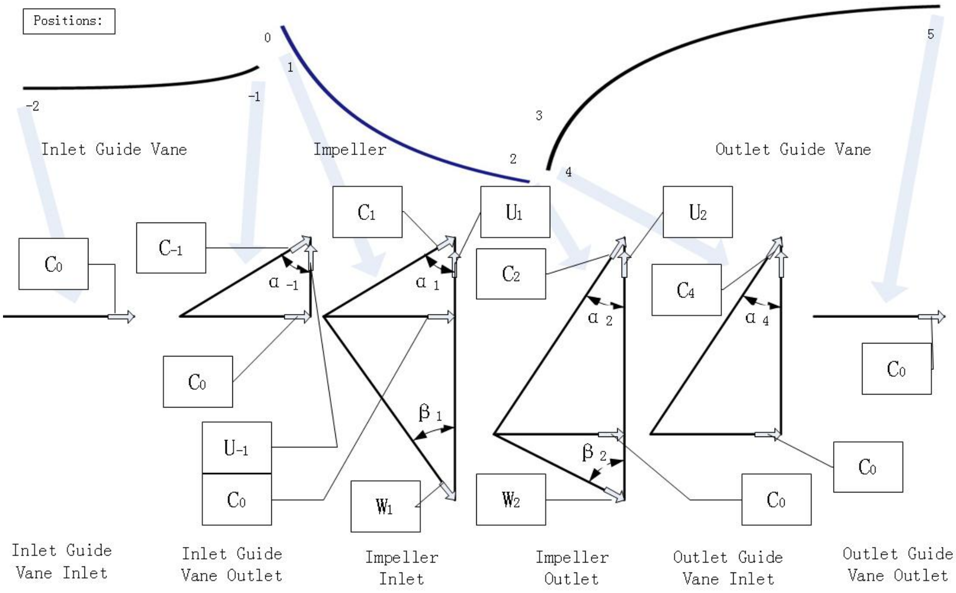

Figure 4.6: Velocity triangles for an axial-flow pump

This corresponds to the work needed by centrifugal force to move 1 kg of fluid along a distance dr. Its integration reads:

$$Y' = \frac{1}{\rho}\int_{p_0}^{p_\infty} dp = \frac{p_\infty - p_0}{\rho} = \omega^2 \int_{r_1}^{r_2} r dr = \frac{u_2^2 - u_1^2}{2} \tag{4.8}$$

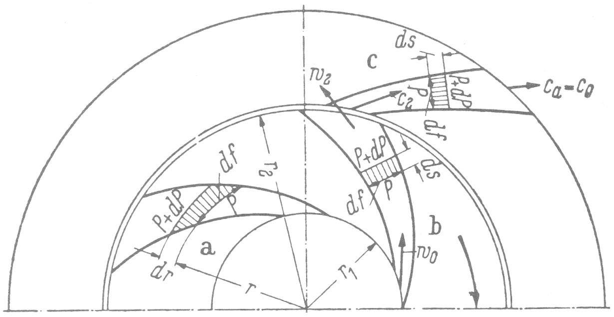

Figure 4.7: Typical pressure variation in impeller and outlet guide vane in a centrifugal pump [102]

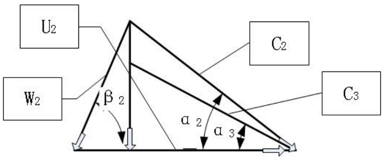

Figure 4.8: Velocity triangle just before/just after blade end taking into account blade thickness [102]

In region (b) of Fig. 4.7, the dynamic equation for the fluid control volume reads:

$$df dp = -df \rho w dw = -df \rho \frac{ds}{dt} dw = -df ds \rho \frac{dw^2}{dt} \tag{4.9}$$

Equation (4.9) for the whole channel length is:

$$Y'' = \frac{1}{\rho}\int_{p_\infty}^{p_{p\infty}} dp = \frac{p_{p\infty} - p_\infty}{\rho} = \frac{w_0^2 - w_2^2}{2} \tag{4.10}$$

Thus, the total pressure rise in the impeller is:

$$\frac{p_{p\infty} - p_0}{\rho g} = \frac{u_2^2 - u_1^2 + w_0^2 - w_2^2}{2g} \tag{4.11}$$

In the outlet guide vane (region (c) of Fig. 4.7), part of the kinetic energy is converted into a pressure rise, and the corresponding equations read:

$$\begin{aligned} df\,dp &= -df\,ds\rho\frac{dc}{dt} & (4.12)\\ \frac{dp}{\rho} &= -cdc & (4.13)\\ &= dY''' & (4.14)\\ Y''' &= \frac{p_{2\infty} - p_{p\infty}}{\rho g} & (4.15)\\ &= \frac{c_2^2 - c_1^2}{2} & (4.16)\end{aligned}$$

Finally, the total pressure rise for the whole pump is:

$$H_{th} = \frac{p_{p\infty} - p_0}{\rho g} + Y''' = \frac{1}{2g}(u_2^2 - u_1^2 + w_0^2 - w_2^2 + c_2^2 - c_1^2) \tag{4.17}$$

Since $w_2^2 = u_2^2 + c_2^2 - 2u_2c_2\cos\alpha_2$ and $w_0^2 = u_1^2 + c_0^2 - 2u_1c_0\cos\alpha_1$, Equation (4.17) can be rewritten into:

$$H_{th} = \frac{u_2c_2\cos\alpha_2 - u_1c_1\cos\alpha_1}{g} \tag{4.18}$$

Considering an inflow without rotation ($\beta_0 = 0$), the pressure head equation can be simplified as:

$$H_{th} = \frac{u_2c_2\cos\alpha_2}{g} \tag{4.19}$$

The blade angles at the shaft, at the blade radial top, and at the middle position, are usually calculated separately, in order to ensure equal or at least similar values of c_A along axial planes.

The blades of the inlet guide vane are designed to reduce useless rotation before the impeller and to ensure a smooth transition between inlet guide vane and impeller. The blades of the outlet guide vane are designed to ensure a smooth transition between impeller and outlet region, and to support a maximal conversion efficiency from kinetic energy to pressure energy. Detailed equations are given later in Section 4.2.

When considering the real thickness of the blade, the velocity triangles are modified, as shown at the end of the impeller in Fig. 4.8. However, the overall flow rate $c\cos\alpha$ does not change before and after the blade end, and is used as a bridge between the equations for impeller and guide vanes.

4.1.3 Past Experience Concerning CFD of Blood Pumps

The computation of the pump will rely on Computational Fluid Dynamics (CFD). Since blood pumps show very specific properties, it is useful to describe in more details practical aspects associated with CFD of such pumps.

CFD is being increasingly used as a promising design tool for the development of VAD systems. It is employed not only at an early stage (design), but also later (optimization). Applying CFD for blood pumps shows the following advantages [103]:

- Time and cost-effectiveness, since prototype building and experiments can be reduced;
- Full information concerning the exact flow properties within the device are obtained;
- Easy design modifications become possible.

In the field of turbomachinery, ANSYS® CFX (formally called CFX-TASCflow/CFDS-FLow3D/CFX-4) is the most widely employed commercial CFD tool, because it comes with a variety of add-ons developed during decades to support and facilitate corresponding computations. It uses a hybrid finite volume/finite element methodology, by which the control volumes are constructed around nodes, while finite elements describe the solution variation within each element. It is of course also possible to use other commercial solvers, like ANSYS® Fluent and STAR-CCM+, or Open Source tools like OpenFOAM [104]; all these tools are based on a pure finite volume methodology.

The total grid size employed to simulate a whole pump varies typically in the scientific literature and considering our own experience from 0.1 to 5 million cells. CFD simulations of pumps often require hexahedral meshes with O-grid around the blades, becoming progressively finer in the direction perpendicular to the blade in order to capture the large pressure gradients. For instance, Taskin's simulation of the UltraMag centrifugal pump used a hybrid mesh of 3.86 million cells, showing that (*a*) a hybrid mesh may be a good compromise between the difficulty of meshing complicated geometries with a structured mesh, and the benefits of having a structured mesh in critical regions, (*b*) the mesh structure may influence the calculated flow field in the gap region, since the expected vortices were only observed when using a hexahedral mesh [105, 106].

Many older numerical simulations of centrifugal and axial-flow blood pumps used as an approximation CFX's Frozen Stator-Rotor model (or the equivalent Multiple Reference Frame model of Fluent). Though such approaches lead to a tremendous reduction in the needed computational resources, they constitute only an approximation of reality and may lead to noticeable errors, increasingly so for strong interactions between rotating and static parts. Song et al. investigated the difference between MRF and Sliding Mesh models for the HeartQuest CF4, showing that the (steady) pressure head predicted by MRF was about 2% higher than the (average) pressure head predicted by Sliding Mesh [106, 107]. With the continuing increase of computer power, simulations in the future are likely to use in a systematic manner the far more realistic General Grid Interface model of CFX and OpenFOAM (or the equivalent Sliding Mesh model of Fluent).

In the scientific literature, the documented hydraulic efficiency of blood pumps covers a huge range, from 20% to 80%. Predicting the hydraulic performance by CFD is a difficult task. Part of the error is introduced by the imprecision of the employed turbulence models. Several comparisons between experimental values and CFD concerning pressure have been published. For the standard $k-\epsilon$ turbulence model, the pressure head was overpredicted by $30-60$ mmHg (25-70%) in the HeartQuest CF3 ; in the Kyoto-NTN, it was underpredicted by 10 mmHg (8.3%); in the Virginia LEV-VAD, it was overpredicted by 10 mmHg (10%); in the PVAD22, it was underpredicted by 15 mmHg (13%); in the Impella it was underpredicted by 24 mmHg (30%). When activating the logarithmic wall function with the $k-\epsilon$ model, the pressure head prediction error was 20 mmHg (18%) for the Virginia LEV-VAD and 10 mmHg (30%) for the PVAD3. Finally, when using the SST $k-\omega$ model, the TinyPump's pressure head was underpredicted by $4-25$ mmHg (5-21%) [106].

Concerning hemolysis, an accurate prediction of shear stress is essential. However, this is a difficult task for CFD. When simulating by CFD the Kyoto-NTN with the standard $k - \epsilon$ turbulence model at 2500 rpm with a 3 mm gap, the calculated maximal shear stress was 696 Pa on the casing and 203 Pa in the fluid, compared with experimental measurements of 450 Pa on the casing and 180 Pa in the fluid [106]. With a narrower gap of 0.5 mm, the calculated maximal shear stress was 585 Pa in the fluid, compared with an experimental value of 330 Pa, showing a very large difference (by a factor of 1.8). All these comparisons illustrate the difficulty of simulating properly blood pumps with CFD.

4.1.4 CFD-based Design Optimization of a Blood Pump

Although the concept of CFD-O is not new, the extremely high computational costs typically associated to this process still limit its applicability. Figure 4.9 is the flow chart of a typical CFD-based design process, see also [14, 108] for further details. CFD-O is usually started from a fairly good design, which is achieved by an experience-based cut-and-try approach. Most published instances of CFD-O for blood pumps involve only regional optimization, without parameterizing the geometry of the whole pump. The difference between obtaining (manually) a so-called "Optimized Design" and an (automatic) Design Optimization, as considered in the present Thesis, is explained in Table 4.3.

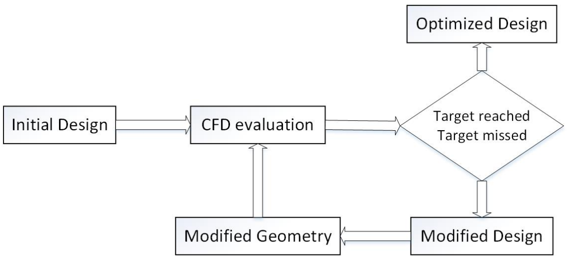

Figure 4.9: A CFD-based design process

	Module Options		
	Evaluate Design	Modify Design	Modify Geometry
Optimized Design	Qualitative	Institution & Experience	Manual
Design Optimization	Quantitative	Formal Optimization	Automatic

Table 4.3: Optimized Design vs. Design Optimization [108]

One major challenge of CFD-O is the automatic and robust looping, involving all steps shown in Fig. 4.9 without human interference. In many published works, part of the optimization remained a manual process. For instance, the geometry was parameterized and updated in an automatic manner, but the grid was still generated manually. Using such a semi-automatic approach, and after choosing two or more values as geometry variables, the influence of these variable on the objective(s) can be evaluated [109–112].

More recently, a few works describing fully automatic pump optimization have been published. Singh et al. developed an automatic remeshing technique based on an elastic spring analogy for unstructured meshes [113]. This remeshing technique was used to automatically optimize the outlet stator of a cardiac assist device [114]. The mesh contained about 55 500 tetrahedral elements. Six geometry variables were chosen to regulate the diameter of the outlet region, while the blade angles were kept fixed for the stator.

Zhu et al. optimized the diffuser of an axial-flow blood pump with fixed-shape straightener and impeller. The mesh for the fixed parts involved about 500 000 elements. Remeshing was carried out by re-running an Ansys® ICEM-CFD replay file, ESTECO® modeFRONTIER4.0 was used for procedure control, and the NSGA-II algorithm was used for generating variables' values. A total of 37 days were needed for the simulation of a total of more than 1 600 designs, on a platform built with 20 CPUs with average frequency of 2.4 GHz. The two objective functions were pressure head and backflow index. The maximum pressure output obtained was 93 mmHg [115].

Derakhshan et al. optimized a centrifugal pump considering 6 geometry variables, by using artificial neural networks (ANNs) and an Artificial Bee Colony algorithm. The mesh involved about 230 000 nodes. The evaluation of each design consumed half an hour of computing time on a platform of Intel Core i5 processor 2.4 GHz with 4 GB memory [116].

4.2 Basic Design of a Screw-type Axial-flow Pump

The design method presented in this section is a combination of the approaches presented in several reference textbooks [99, 101, 102, 117].

The standard working condition of a blood pump is: 1) a flow rate of $8.33\,10^{-5}$ m^3/s (corresponding to 5 L/min), and 2) a pressure head equivalent to 1.36 m of water, corresponding to 100 mmHg. Hence, as an additional challenge, each new design requires more than one single CFD simulation, in order to ascertain the right rotating speed (variable parameter), which delivers the right pressure head (prescribed value) for the given flow rate (prescribed value). It is therefore clear that the computational challenges associated with this problem are extremely high. A new, more efficient solution procedure is required.

Some further considerations, important for the design of a blood pump, are:

1. Due to limited viscosity differences, and looking back at Fig. 4.5, the correction factors C_Q and C_H for blood are very close to 1. Hence, the design method for a water pump can be directly used for a blood pump.
2. Though inlet guide and outlet guide are not a compulsory requirement for the design of an axial-flow pump, they are almost always found in existing blood pumps, in particular to accommodate the fixed part of electronic magnets for the levitation system. Therefore, both inlet and outlet guide vanes will be considered in what follows.
3. Existing axial-flow blood pumps usually employ a screw-shaped impeller with considerable axial length, in order:
    - To achieve a smoother blade angle change from β_1 to β_2, leading to low shear stress;
    - To achieve a larger blade angle change, $\beta_1 - \beta_2$, and thus a higher pressure head at a lower rotating speed.
4. Since $\beta_1 - \beta_2$ is large, the standard axial-flow pump pressure head equation

$$Y = \zeta_a \frac{u w_\infty^2 l}{2 c_A t} \sin(\beta_\infty + \lambda) \tag{4.20}$$

leads to a poor accuracy for such a design. Instead, the general pressure head equation (Eq. 4.19) is preferred in the design process.

5. For calculation convenience, a simple geometry is chosen in this first work, involving a constant diameter for impeller and guide vanes.
6. For the same reason, it is assumed that $\alpha_{-2} = \alpha_{-1} = \alpha_5 = 90°$.

Design Procedure

The first step is to choose the minimal specific speed of an axial-flow pump, $N_q = 110$ 1/min, which corresponds to the highest H/Q ratio:

$$N_{qy} = 3N_q \times 10^{-3} = 3 \times 110 \times 10^{-3} = 0.33 \tag{4.21}$$

Then use Eq. (4.5) to calculate n:

$$n = N_{qy}\frac{Y^{3/4}}{Q^{1/2}} = 0.33\frac{(1.36 \times 9.8)^{3/4}}{(8.33 \times 10^{-5})^{1/2}} = 252.21 \quad (rpm) \tag{4.22}$$

Assuming an average impeller inlet squeeze coefficient $\overline{\psi}_1 = 0.8$, choose average values $\beta_0 = 20°$, $\alpha_{-1} = \alpha_0 = \alpha_1 = 90°$. For $N_s = 110$ 1/min, the empirical best d/D-ratio is 0.7. Then, calculate the axial velocity by:

$$\begin{aligned} c_A &= \left(\frac{4\pi \tan^2 \beta_0 k_2}{\left(1-\left(\frac{d}{D}\right)^2\right) k_1} Qn^2\right)^{1/3} \\ &= \left(\frac{4\pi \tan^2 17° \times 0.8}{0.51 \times 1} 8.33\,10^{-5} \times 252.21^2\right)^{1/3} = 2.995 \quad (m/s) \end{aligned} \tag{4.23}$$

where, $k = 1 - (d/D_A)^2 = 0.51$ is the contraction factor, and $k_1 = D_1/D_A = 1$ if the pump has a fixed diameter (simple design). Additionally, $k_2 = c_0/c_A = 0.8$ for $\overline{\psi}_1 = 0.8$.

Then, calculate the equivalent diameter:

$$D_0 = \left(\frac{4Q}{\pi c_A}\right)^{1/2} = \left(\frac{4 \times 8.33\,10^{-5}}{2.136\pi}\right)^{1/2} = 5.95\,10^{-3} \quad (m) \tag{4.24}$$

The diameters are then obtained by:

$$D = \frac{D_0}{\left(1-\left(\frac{d}{D}\right)^2\right)^{1/2}} = \frac{7.05\,10^{-3}}{\sqrt{1-0.7^2}} = 9.92\,10^{-3} \quad (m) \tag{4.25}$$

and

$$d = 0.7D = 7.93\,10^{-3}(m) \tag{4.26}$$

At this point, it is possible to calculate the circumferential velocity, for a simple axial flow with constant diameters:

$$u_{1n} = u_{2n} = \pi n d = 7.41 \quad (m/s) \tag{4.27}$$

$$u_{1x} = u_{2x} = \pi n D = 9.27 \quad (m/s) \tag{4.28}$$

For an axial-flow pump with screw-type long blades, β_n and β_x should obey the following rule, in order to ensure that the blade stays perpendicular to the axis on the span direction:

$$d \tan \beta_n = D \tan \beta_x \tag{4.29}$$

Taking as a first estimate $\beta_0 = 20°$ for the geometrical middle spanwise position of the blade, it is possible to calculate the blade angles at blade top and bottom separately:

$$\beta_{1x} = \arctan\left(\tan\beta_0 \frac{D}{\sqrt{\dfrac{D^2+d^2}{2}}}\right) = 22.02° \tag{4.30}$$

$$\beta_{1n} = \arctan\left(\tan\beta_0 \frac{d}{\sqrt{\dfrac{D^2+d^2}{2}}}\right) = 17.93° \tag{4.31}$$

Considering a number of blades $z = 2$ and a blade thickness $\delta = 1$ mm, it is possible to calculate the real average squeeze coefficient with a slightly simplified formulation:

$$1 - \frac{z\delta}{\sin\beta_0} \frac{1}{\pi\sqrt{\dfrac{D^2+d^2}{2}}} = 0.79 \tag{4.32}$$

If a large difference is found between the assumed squeeze coefficient and the real average one, then the thickness of blade δ should be modified to reduce the difference. If the thickness of the blade is fixed due to physical limitations, then the former steps should be repeated iteratively, until reaching a close fit between the real and the target value.

The next step is to calculate the blade angle at rotor outlet. Assuming first a pump efficiency $\eta_i = 0.8$ as an initial guess, solve Eq. (4.33) using Eqs. (4.34) and (4.35):

$$\frac{H_{th}}{\eta_i} = u_{2m} c_{2m} \cos\alpha_{2m} \tag{4.33}$$

$$\sin\alpha_{2m} = \frac{c_0/\phi_{2m}}{c_{2m}} \tag{4.34}$$

$$\phi_{2m} = 1 - \frac{z\delta}{2\pi\sqrt{\dfrac{D^2+d^2}{2}}\sin\alpha_{2m}} \tag{4.35}$$

This results into:

$$(\alpha_{2m},\ \psi_{2m},\ c_{2m}) = (28.38°,\ 0.85,\ 5.85\ m/s) \tag{4.36}$$

where α_{2m} refers to the velocity angle at middle spanwise position. Here, the variable values at spanwise middle position are used as the average values for calculating the pressure head, in order to simplify the numerical procedure.

The blade angles at rotor outlet are calculated by:

$$\beta_{2m} = \arctan \frac{c_0/\phi_{2m}}{\sqrt{\frac{{u_{2x}}^2 + {u_{2n}}^2}{2}} - c_{2m}\cos\alpha_{2m}} = 41.03° \tag{4.37}$$

together with

$$\beta_{2x} = \arctan\left(\tan\beta_{2m}\frac{D}{\sqrt{\frac{D^2+d^2}{2}}}\right) = 44.04° \tag{4.38}$$

and

$$\beta_{2n} = \arctan\left(\tan\beta_{2m}\frac{d}{\sqrt{\frac{D^2+d^2}{2}}}\right) = 37.72° \tag{4.39}$$

Then, it is possible to calculate α_4:

$$\alpha_{4x} = \arctan\left(\tan\alpha_{2m}\frac{D}{\sqrt{\frac{D^2+d^2}{2}}}\right) = 43.87° \tag{4.40}$$

and

$$\alpha_{4n} = \arctan\left(\tan\alpha_{2m}\frac{d}{\sqrt{\frac{D^2+d^2}{2}}}\right) = 37.54° \tag{4.41}$$

As a summary, all angles (assumed or obtained from the numerical procedure) are listed in Table 4.4.

	position					
	-2	-1	1	2	4	5
α_x	90°	90°	-	-	43.87°	90°
α_n	90°	90°	-	-	37.54°	90°
β_x	-	-	17.93°	37.72°	-	-
β_n	-	-	22.02°	44.04°	-	-

Table 4.4: Blade/velocity angles

4.3 Design-theory-based CFD-O for Axial-flow Pump

As already explained, CFD-O refers to the computer-based optimization relying on evaluations obtained by CFD. Here, optimization means that corresponding algorithms are employed to converge toward optimal solutions as quantified by (possibly concurrent) objective functions. It is not simply a comparison between a few designs, with a final statement that the best of those is the "optimal" one, as often found in the literature. After developing, testing and validating the procedure, the resulting optimization is at the end a fully automatic process. Concerning CFD-O, our group has gathered a rich experience over the last fifteen years, from wind turbines to burners, from bioreactors to heat exchangers. The fundamental description of the approach used for CFD-O in our group is found in [14, 15, 118]. Specific examples associated to the optimization of turbomachines considered in particular vertical-axis wind turbines [119], Wells turbines [120] and Pitot-tube pumps [121].

A fully automatic optimization employs a shell program for choosing and generating the parameter variables, and for controlling the optimization loop. In this automatic optimization loop, geometry and mesh generators, CFD solver, and all further pre- and post-processing tools are all integrated. The involved tools are executed based on journal scripts, so that the optimization proceeds automatically without need for human interference. The shell program calls all the integrated tools in a pre-defined sequence, and repeats this sequence in a loop, with embedded tests and controls to avoid any error.

Based on our experience during the last fifteen years, Evolutionary Algorithms (EA) are very robust for CFD-O and have been used in the vast majority of our projects. This is done as well for the rotary blood pump now considered. EA involve iterations sorted in groups, which are called design "generations" in EA terminology. The variable values of later generations depend on the outcomes (objective values) of earlier generations. After analyzing each generation, the corresponding objective values are stored in a result file for final analysis.

The main limitation of CFD-O is the vast requirement in terms of computational resources concerning both hardware (computing time, memory requirements) and software licenses (when using commercial CFD solvers, as done in the present project). This is particularly true for standard EA procedures considering multi-objective, concurrent optimization, since a large number of designs must be simulated in order to identify and populate the set of optimal solutions (so-called Pareto front). For this reason, most CFD-O analyses documented in the past considered only two-dimensional or axis-symmetric configurations, or extremely simple 3D geometries, both usually for steady flows. In that case, the numerical cost of a CFD evaluation is low, and EA can really perform excellent work. However, the blood pump considered in the present article is an axial-flow pump with inlet and outlet guide vanes. It is a complex 3D geometry, which can not be simplified and simulated in 2D. Each evaluation requires unsteady flow simulations with nine complete rotations, in order to reach periodic steady-state results. As a final difficulty, each new design requires more than one single CFD simulation, in order to find out the right rotating speed (variable parameter), which delivers the right pressure head (prescribed value) for the given flow rate (prescribed value). It is therefore easy to understand that the computational challenges associated to this problem are extremely high. A new, more efficient solution procedure is needed.

For this purpose, it is useful to look at the currently used procedure for commercial providers of innovative pump designs. Progress is there very strongly connected to the impressive experience of the involved engineers, supported by well-established scientific and technical procedures known as pump design theory, building on top of at least one century of high-quality research. In its current state, pump design theory is a combination of mathematical procedures and technical empirical experience. It provides a well-trained engineer with a close-to-best pump design suitable for further CFD and/or prototype tests. Pump design theory can readily provide, in addition to relevant geometrical data, indicative values for rotating speed, expected flow rate and pressure head around the design point.

Therefore, a very promising solution can be obtained by combining the best of the two approaches. This extended method is called "design-theory-based CFD-O" (DTB-CFD-O) in what follows. DTB-CFD-O uses pump design theory to reduce the total number of designs that must still be evaluated using CFD, by: 1) avoiding the evaluation of completely atypical designs that are incompatible with the design theory and would thus deliver probably an extremely poor efficiency; 2) reducing the number of geometrical parameters involved in CFD-O, since many geometrical variables can be expressed as a function of other variables thanks to design theory; 3) delivering suitable assumptions for the rotating speed leading to the targeted pressure head, thus reducing the number of inner iterations within each CFD-O evaluation.

The function of design theory as a support of a CFD-O can best be illustrated by an example.

Suppose the geometry of a design can be parameterized by 3 variables: x_1, x_2 and x_3. If x_3 can be expressed as a function of x_1 and x_2 using Eq. (4.42), derived from design theory,

$$x_3 = f_1(x_1, x_2) \tag{4.42}$$

then x_3 is no longer a free geometrical variable, and therefore the number of geometrical variable is reduced from 3 to 2.

If, additionally, x_1 and x_2 can be correlated by design theory through Eq. (4.43),

$$x_2 = cx_1 \tag{4.43}$$

where c is a proportionality variable evolving within a known range (c_1, c_2), then c can be involved instead of x_2 as design variable. Finally, as illustrated in Fig. 4.10, the design space considered in the optimization can be tremendously reduced. It shrinks for the first generation from the square region of $[0, x_1'] \times [0, x_2']$ to the gray region between line x_1c_1 and line x_2c_1; the two red regions can be completely omitted from the evaluation. Thus, the number of evaluated designs can be very strongly reduced, leading to a considerable speed up. It is worth mentioning that, for the second generation of designs, the evaluation regions for x_1 and x_2 are reduced to $[x_1'', x_1''']$ and $[x_2'', x_2''']$, respectively. Thus, Eq. (4.43) is further on helpful to reduce the evaluation domain by omitting the two light-green regions. This applies as well during the whole optimization process.

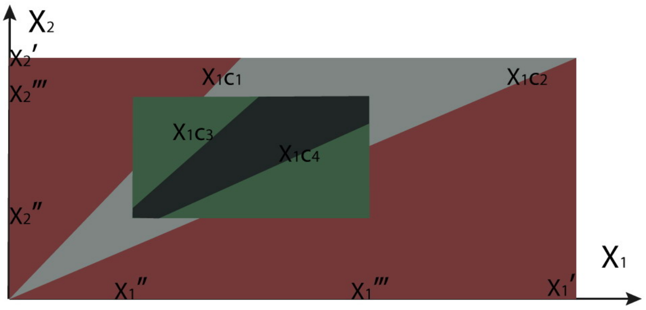

Figure 4.10: Example showing the design parameter space and how it can be reduced thanks to design theory

For the special case of a screw-type axial-pump (also sometimes called Archimedes screw pump), DTB-CFD-O is a key to success by:

1. Establishing a relation between β_x and β_n at each axial position. Thus, it is possible to suppress at least one design variable at each axial position, while still ensuring that the extension line from the blade top to the blade bottom meets the axis.
2. Using N_q to decide d/D and n. This empirical method ensures that the produced design works close to the optimal working condition on the characteristic curve.

3. Using an assumed η_o to calculate β_2, thus narrowing the range of design variable values for β_2. Although this first assumption for η_o may initially lead to a large inaccuracy, it is still more robust than assuming β_2 directly, as shown by first tests.
4. Using a coefficient to relate β_2 with β_4 (and also β_1 with β_{-1}). This is used to reduce the size of the domains $\beta_4 - \beta_2$ (and $\beta_1 - \beta_{-1}$), similarly to the example shown in Fig. 4.10.

Geometry Parameterization

Now, it is time to describe the numerical strategy employed to parametrize the Archimedes screw pump in the DTB-CFD-O approach. Figure 4.11 shows the derivation logics for the five design parameters (or geometrical variables) used in the simplest optimization strategy. Here, N_q, β_0, η_o, ξ and K_4 are the design variables, and all other pump geometrical variables are derived from those five variables. Decades of experience by pump practitioners prove that values of N_q, β_0 and, to a lesser extent, η_o are absolutely essential to determine properly the geometry, and therefore must be kept in the optimization. The variable ξ is particularly important for an Archimedes screw pump, and must also be kept. First tests have shown that K_4, though less essential in general, should be also involved in the optimization for this particular system. To summarize and rank the importance of the five design variables:

- N_q and β_0: absolutely essential;
- η_o and ξ: important;
- K_4: useful.

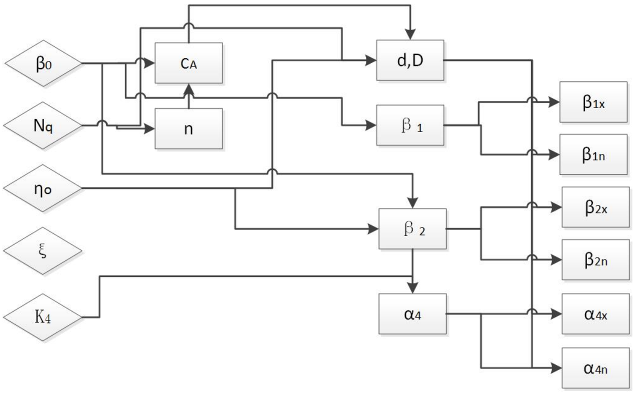

Figure 4.11: Simple optimization strategy involving 5 geometrical variables

Most equations required for this optimization strategy have been already given in Section 4.2. An attack angle is introduced in connection with β_4 by adding a coefficient K_4, thus Eqs. (4.40) and (4.41) are changed to Eq. (4.44) and Eq. (4.45), respectively.

$$\tan\alpha_{4x} = K_4 \tan\alpha_{2m} \frac{D}{\sqrt{\frac{D^2+d^2}{2}}} \tag{4.44}$$

$$\tan\alpha_{4x} = K_4 \tan\alpha_{2m} \frac{d}{\sqrt{\frac{D^2+d^2}{2}}} \tag{4.45}$$

If a more detailed description of the geometry is needed, the next candidates to be retained as design variables are:

- If the ratio between shaft diameter and blade axial diameter, d/D, is not kept constant, it must necessarily be included in the optimization process.

- K_{-1}: The equivalent attack angle coefficient for β_{-1}, β_{-1_x} and β_{-1_n} is governed by Eqs. (4.46) and 4.47, respectively.

$$\tan\alpha_{-1_x} = K_{-1}\tan\alpha_{1m}\frac{D}{\sqrt{\dfrac{D^2+d^2}{2}}} \tag{4.46}$$

$$\tan\alpha_{-1_n} = K_{-1}\tan\alpha_{1m}\frac{d}{\sqrt{\dfrac{D^2+d^2}{2}}} \tag{4.47}$$

Finally, the optimization involving seven design variables is the one that has been retained in the rest of this Thesis (see next chapter for more information), since it is the only one leading to acceptable computing times.

However, if an even more precise description of the geometry is required (and if corresponding computational resources are available...), the next candidates as design variables are:

- l: If the total axial length of the pump is pre-defined, l_i can be estimated by the minimal length of the electronic magnets, and then $l + l_o = l_{maxAvailable}$. Choosing l as input variable, then l_o is a derived variable.

- $K_{1.5}$: This is the equivalent angle of attack coefficient for $\beta_{1.5_m}$. For a screw-type impeller with a long axial length, the optimal changing rate of blade angle, $\partial\beta/\partial l$, may not be constant. Then, one or more control point(s) along the axial length should be used to control the change in blade angle. It is proposed to use first one single additional point at average blade angle $\beta_{1.5_m}$ as control point, located exactly in the middle of the rotor axial length, together with Eq. (4.48):

$$K_{1.5}\frac{H_{th}}{\eta_o} = u_{1.5_m}c_{1.5}\cos\alpha_{1.5_m} \tag{4.48}$$

This equation is then solved together with Eqs. (4.49) and (4.50):

$$\sin\alpha_{1.5_m} = \frac{c_0/\phi_{1.5}}{c_{1.5}} \tag{4.49}$$

and

$$\phi_{1.5} = 1 - \frac{z\delta}{2\pi\sqrt{\dfrac{D^2+d^2}{2}}\sin\alpha_{1.5_m}} \tag{4.50}$$

Afterwards, the blade angles at shaft and shell are calculated respectively by:

$$\beta_{1.5_n} = \arctan\left(\tan\beta_{1.5_m}\frac{d}{\sqrt{\frac{D^2+d^2}{2}}}\right) \tag{4.51}$$

$$\beta_{1.5_x} = \arctan\left(\tan\beta_{1.5_m}\frac{D}{\sqrt{\frac{D^2+d^2}{2}}}\right) \tag{4.52}$$

- $\triangle l_1$, $\triangle l_2$: The gap between inlet guide vane and rotor, $\triangle l_1$, and the gap between rotor and outlet guide vane, $\triangle l_2$, can be critical to control the turbulence generated at this level, and could be therefore adopted as additional input variables.

Taking into account all those design variables in an advanced optimization, the flow chart allowing to derive all needed quantities is shown in Fig. 4.12.

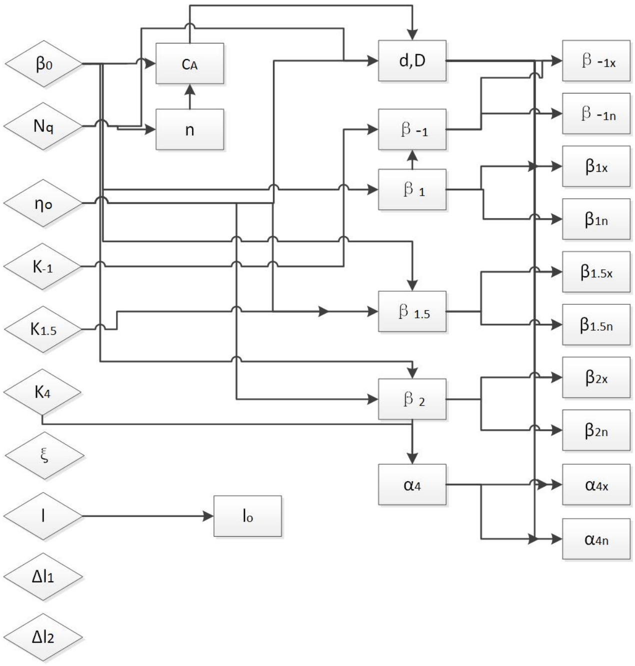

Figure 4.12: Advanced optimization strategy

4.4 Practical Optimization Procedure

4.4.1 General Method

The optimization strategy proposed above has been implemented by coupling the commercial optimization tool ESTECO® modeFRONTIER 4.0 with the commercial CFD package ANSYS® CFX 14. However, the described approach is generally valid and could obviously be used for other applications; it could rely on other software.

Pump hydraulic efficiency is adopted as primary optimization objective, while hemolysis may be also integrated as an additional, concurrent objective, as discussed later on.

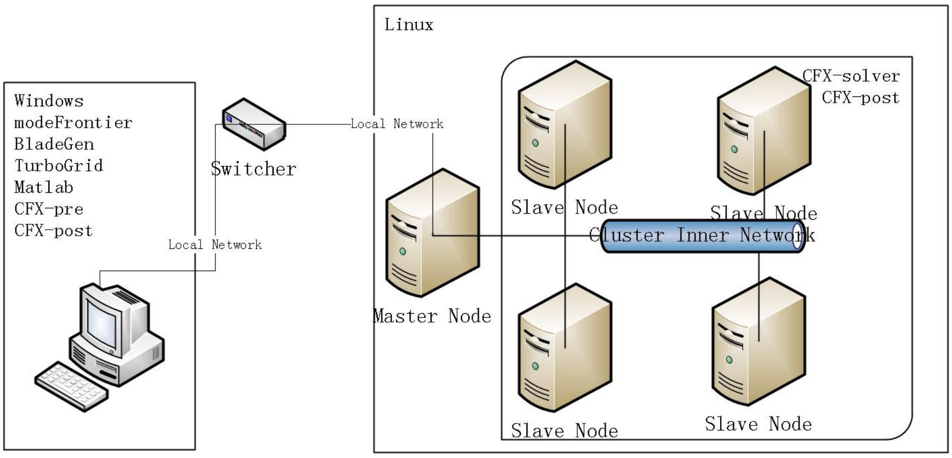

Figure 4.13: System distribution of the employed numerical tools

In order to combine the advantage of parallel computing with convenient real-time monitoring and post-processing, a distributed allocation of the employed softwares can be adopted. The choice of this infrastructure is also conditioned by some limitations concerning the supported operating systems by the employed numerical tools. The finally used allocation of all numerical tools is shown in Fig. 4.13. Transfer of information through the network is performed by ”remote SSH” function in ESTECO® modeFrontier, and the most important transfered data are the CFX ”.def” file (from desktop to cluster) and the result ”.txt” file (from cluster to desktop). The main CFD simulation and part of the post-processing are carried out on the Linux cluster, while pre-process, another part of the post-processing, design evaluation and support by pump design theory are carried out on the Windows desktop.

The data flow path through the different numerical tools is shown in Fig. 4.14. In the loop, modeFrontier generates all values for the design variables; then, these value are sent to a Matlab code, which generates all derived values. At that point, modeFrontier gathers back the complete geometrical information, and sends it together with the rotating speed to the tools employed to generate the geometry and mesh, ICEM-CFD, BladeGen and TurboGrid. In order to maximize grid quality while keeping a robust procedure, geometry and grid are generated in five different parts (see next section for more details). The parts are then sent to CFX-Pre, which calls a pre-generated journal file and assembles the grids together, and outputs a CFX ”.def” file. Then, modeFrontier sends this file to the Linux cluster and calls the CFX-Solver to carry out the CFD simulation. During this simulation, an additional CFX User-Fortran code is activated to calculate hemolysis. The result file ”.res” is filtered to obtain values for efficiency and hemolysis by running ”cfx5mondata” on the Linux cluster. As a last step, a ”.txt” file containing efficiency and hemolysis information is sent back to the Windows desktop, and modeFrontier evaluates the results, before starting the next iteration loop.

4.4.2 Numerical Tools

4.4.2.1 Preprocessing

As explained previously, the geometry and mesh are generated in five separate parts:

1. inlet pipe and shaft before guide vane,
2. inlet guide vane,
3. impeller,
4. outlet guide vane,
5. shaft after guide vane and outlet pipe.

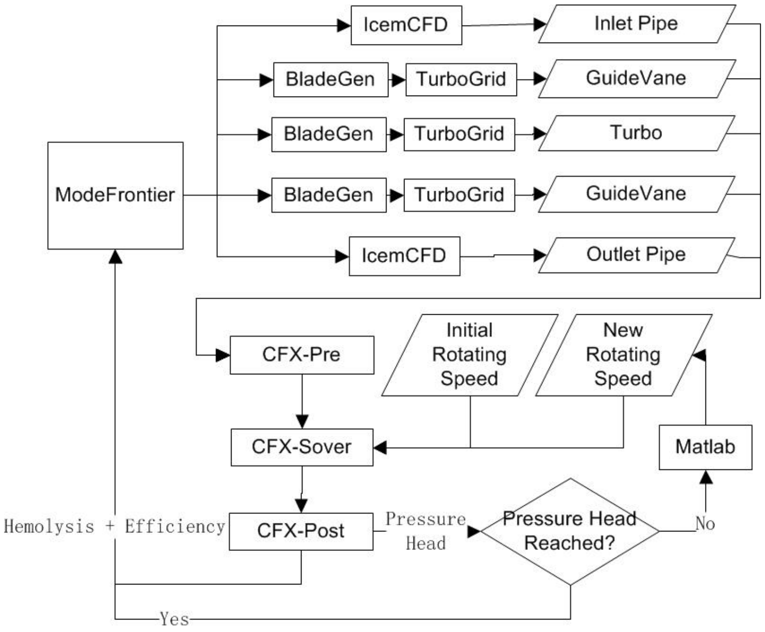

Figure 4.14: Flow chart for optimization of an Archimedes screw pump

The geometries and meshes of parts 1 and 5 are generated by ANSYS® ICEM-CFD thanks to journal files. Typically, many control points are needed along the shell as well as at the beginning and at the end of the shaft in order to get a smooth geometry. This is obtained by a recursive procedure coded unter Matlab, starting from only few control points and cutting iteratively the segments into two equal parts.

The geometries of parts 2, 3 and 4 are generated by ANSYS® BladeGen, which is a dedicated generator for turbomachines. Automatization is based on a script, in which the diameters and blade angles at user-chosen axial positions (the corresponding number of positions is unlimited) are recorded. Compared to ICEM-CFD, BladeGen requires far less operations and is able to generate corresponding geometries in a far more robust manner.

The grids of parts 2, 3 and 4 are generated by ANSYS® TurboGrid, which is a dedicated mesh generator associated to BladeGen. Using this tool, it is very convenient to obtain a fully hexahedral grid for the geometries generated by BladeGen. An example of an hexahedral grid generated by TurboGrid in this manner is shown in Fig. 4.15.

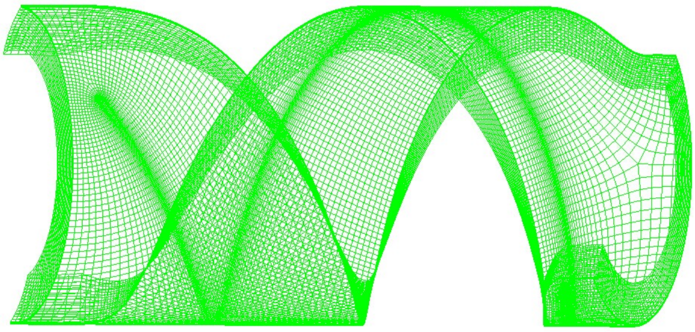

Figure 4.15: Example of TurboGrid hexahedral meshing

The tools employed to generate each part of the geometry and mesh are summarized again in Fig. 4.16.

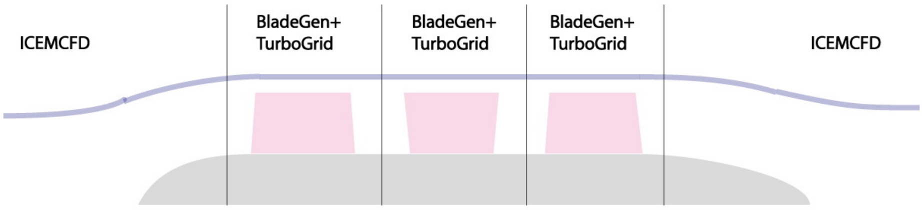

Figure 4.16: Tools employed to generate each part of the geometry and mesh

In practice, using BladeGen and TurboGrid instead of ICEM-CFD has been a major help for this project. It was almost impossible to develop a sufficiently robust procedure using ICEM-CFD. The geometries, and consequently the mesh topologies needed for this project are very complex, involving H-grid and O-grid hexahedral structures.

However, one problem of BladeGen and TurboGrid is that these tools can only run on a Microsoft® Windows platform. Therefore, a Windows optimizer tool (like modeFrontier in this project) is needed.

4.4.2.2 Solver

ANSYS® CFX 14.0 is employed for CFD-solving. Generally, CFX and ANSYS® Fluent offer very similar CFD functions. CFX shows some advantages over Fluent concerning turbomachine simulation. Additionally, it was observed to be more tolerant concerning complex mesh structures compared to Fluent.

However, Fluent would certainly also be capable of solving similar problems. In addition, open-source tools like OpenFOAM, which was tested for turbomachinery optimization in several master theses in our group [104, 122] could be used as well. Preliminary tests have, however, shown that OpenFOAM often encounters stability problems when using dynamic mesh. Additionally, the complex geometries and meshes needed for this project could not be generated automatically with any available open-source tool, so that a license-free procedure seems out of reach at present.

The CFX simulation is systematically carried out for transient flows, including a transient stator-rotor dynamic mesh model. Only one blade section is meshed and simulated for the impeller and guide vanes in order to save computational time. Therefore, partial GGI (General Grid Interface) and periodical interfaces are used for all variable values in order to map those properly between the mesh interfaces.

4.4.2.3 Adjusting Rotating Speed

Although an approximative value of the rotating speed has been provided for n using Eq. (4.22), it may not generate a pressure head exactly equal to the fixed target value H_{target}, due to the imprecision of the process. A further adjustment of n is hence needed in most cases. Based on the affinity law discussed previously, an updated value for n is given iteratively using Eq. (4.53), and a new CFD simulation is carried out with this new value of n, until this iterative process delivers the requested pressure head within a prescribed tolerance:

$$n_{i+1} = n_i \sqrt{\frac{H_{\text{target}}}{H_i}} \tag{4.53}$$

Figure 4.17 illustrates how this method works in connection with the affinity law.

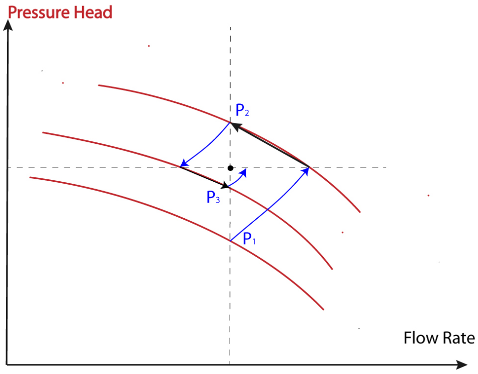

Figure 4.17: Iterative procedure to find the suitable rotating speed n

Suppose that the very first simulation (rotating speed n_1) leads to working point P_1. Then, the rotating speed is adjusted thanks to Eq. (4.53) to n_2, leading to the new working point P_2. In a few steps, the target working point is reached. In practice, an even faster convergence could be obtained by using the modified equation:

$$n_{i+1} = 0.5 n_i \left(1 + \sqrt{\frac{H_{\text{target}}}{H_i}} \right) \tag{4.54}$$

In practice, for each design, a maximum of three inner iterations are considered to update the value of the rotating speed n. If this is not sufficient to reach the targeted pressure head, this particular design is considered as being unsuitable and is simply discarded from the optimization process. A manual check of such designs at the beginning of the project showed that a bad convergence typically stems from unsuitable design parameter combinations, leading to highly unstable flow conditions. For the sake of robustness, such solutions should be removed from the optimization process.

4.4.2.4 Postprocessing

No special postprocessing tool is needed.

Efficiency and pressure head at each time step can be saved into the ".res" file, if predefined by CEL expressions written in CFX-Pre:

```
deltaP areaAve(Pressure)@outlet − areaAve(Pressure)@inlet
Efficiency −2*deltaP * flowRate /(torque_z()@rotor Default *
 rotSpeed/1[rad])/1000[kg m^−3]
```

After completion of the CFD simulation, efficiency at each simulation time step can be written to a text file by following command line, allowing a direct analysis of the value:

```
cfx5mondata −res xx.res −nocoeffloops −varrule
”CATEGORY = USER POINT” −out a.txt
```

The numerical hemolysis prediction method described in Section 2.4.5 has been coded in CFX-User's Fortran. Hemolysis is thus solved simultaneously with the CFD simulation. Details of the code are given in Appendix E.

4.4.2.5 Optimizer

ESTECO® modeFrontier has been chosen as the optimizer, among many options available, due to the following properties:

- Runs both on Windows and Linux environments;
- Easy communication through Windows/Linux platforms by ”remote SSH”;
- Graphical user interface facilitates error debugging and code modifications;
- Extensive built-in graphical analysis of the optimization results.

4.5 Conclusions

Now, all the tools needed for optimizing a blood pump, and more specifically first an Archimedes screw blood pump, are available, working properly and in an acceptably robust manner. Therefore, the optimization can be started.

Chapter 5

Optimization of an Archimedes Screw Blood Pump

The optimization procedure described in the previous chapter has been used to optimize an Archimedes screw blood pump. The first objective is to check the feasibility of the proposed optimization strategy, and to test its robustness. The second goal is to gather information and experience on a screw-type axial-flow blood pump, and to check its possible applicability in practice. Part of this chapter has been submitted as an article to the journal "*Artificial Organs*".

5.1 Details of the Optimization

5.1.1 General Issues

In order to reduce the overwhelming complexity of the problem, the Archimedes screw blood pump has been simplified concerning several aspects: 1) along the axial direction, the pump has constant shaft diameter d and shell diameter, and constant clearance distance ξ; 2) the head and tail of the shaft are not considered in the optimization process; 3) $\tan\beta$, the tangent of the blade angle changes linearly in chordwise direction; 4) the rotor includes two blades, and the inlet guide and outlet guide each includes four blades. In this design, the flow field is axial-symmetrical, regardless of the relative position between the rotor and guide vanes. By applying periodical interfaces in the domain of the CFD solver, only half of the whole volume of the pump has to be numerically simulated.

A standard Archimedes screw-type axial-flow pump corresponds to a fixed value of the blade angle. The third hypothesis listed above allows for modifications of the blade angle corresponding to what is typically found in currently commercialized blood pumps.

Additionally, the considered pump involves only a single stage, which is not really an assumption, since all existing systems comply with this observation.

Summing up the discussion of the previous chapter, the finally realized optimization involves seven input variables, sufficient to parametrize a large number of different designs and relevant for process outcome:

1. The blade angle for infinitely long blade, β_0;
2. The ratio between shaft diameter and blade axial diameter, d/D;
3. The specific speed, N_q;
4. The efficiency loss in the outlet guide vane, η_o;
5. The blade clearance, ξ;

6. The equivalent angle of attack between α_{1m} and α_{-1m}, K_{-1}
7. The equivalent angle of attack between α_{2m} and α_{4m}, K_4.

In a first step, pump efficiency is the only objective and should be maximized.

Figures 5.1-5.3 show as an example three typical designs evaluated during the optimization, together with the design parameter values listed in Table 5.1

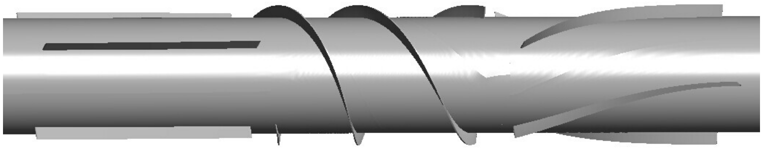

Figure 5.1: Design A

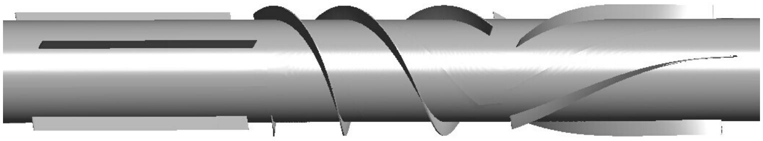

Figure 5.2: Design B

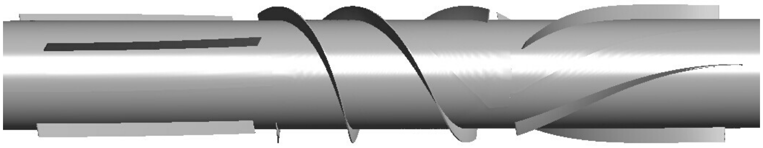

Figure 5.3: Design C

Design	K_{-1}	K_4	β_0	d/D	η_o	N_q	ξ
A	0.0447	0.7668	19.7	0.817	0.953	95.8	0.0678
B	0.0092	0.926	19.5	0.776	0.950	102	0.0614
C	0.148	0.836	19.2	0.789	0.933	94.4	0.0568

Table 5.1: Variable values corresponding to Figs. 5.1 to 5.3

5.1.2 The Variables

5.1.2.1 Rotating Speed n

As already explained, the target pressure head (this time in pressure unit) is 13 300 Pa [7]. For each design, a maximum of three inner iterations are considered to update the value of the rotating speed n. If this is not sufficient to reach the targeted pressure head, this particular design is considered as being unsuitable and is simply discarded from the optimization process. A manual check of such designs at the beginning of the project indeed showed that a bad convergence usually stems from exotic design parameter combinations leading to highly unstable flow conditions. For the sake of robustness, such solutions should indeed be removed from the optimization process.

5.1.2.2 Outlet Guide Efficiency, η_o

The variable H_{th}/η in Eq. (4.33) refers to how much kinetic energy is observed in the fluid, when it leaves the rotor. It equals the expected pressure head, plus the hydraulic loss in the outlet guide and outlet pipe:

$$\text{Loss}_{OutletGuide} = \frac{H_{th}}{\eta_o} - H_{th} \tag{5.1}$$

From engineering experience, the typical hydraulic loss within the outlet guide vane should be less than 10%. Therefore, the efficiency η_o is constrained during the optimization within a range between 0.91 and 0.97.

5.1.2.3 Input Specific Speed, N_q

Specific speed, N_q, is the variable that decides the shape of a pump. However, the traditional relationship between N_q and pump shape has been mostly derived only for blades with a short axial length. To what extent the empirical relationship between N_q and pump shape is valid for a screw-type axial pump is unclear. For this reason, a broader range of N_q, from 80 to 110 (1/min) is used.

5.1.2.4 Shaft to Shroud Ratio, d/D

A screw-type axial pump has usually a large d/D value, in order to avoid large differences in c_A along cross-sections perpendicular to the flow direction. However, the empirical relationship between specific speed and shaft-to-shell ratio (d/D) given in Table 4.2 does not cover large d/D values. It is also unclear to what extent this relationship is valid for a screw-type axial pump with long chordwise length. Therefore, d/D is taken as an individual variable and associated to an input range of 0.75 to 0.9.

5.1.2.5 Tip Clearance, ξ

Clearance is given as an individual geometrical variable, which is not correlated with other variables in the theoretical design process. It is considered as constant throughout the pump axial length. The input range is between 0.03 to 0.08, as a value rendered non-dimensional by dividing with the blade spanwise height.

5.1.2.6 Inlet Blade Angle of Rotor, β_0

The rotor inlet blade angle β_0 is considered as a design variable within the range of 18° to 21°.

5.1.2.7 Equivalent Attack Angles, K_{-1} and K_4

K_{-1} has a range of 0 to 0.3, and K_4 from 0.7 to 1.0.

5.1.2.8 Other Variables

The axial length of rotor and guide vanes are fixed to 0.02 m.

As discussed in the previous chapter, the distance between rotor and guide vanes ($\triangle L_1$ and $\triangle L_2$) is expected to have also an influence of the pump behavior, but is not included as a variable. It is fixed to 0.002 m in this study in order to reduce the complexity of the process.

5.1.3 Numerical Settings

The automatic optimization is extremely complex and involves a variety of tools that must be coupled in a safe and efficient manner before getting proper results. This required at the end many months of work. The shell program employed to control the optimization process is ESTECO® modeFrontier 4.0. All equations from design theory have been coded in a script using Mathworks® Matlab 2010. The geometry of guide vanes and rotor is generated automatically using Ansys® BladeGen thanks to an in-house script. Grid generation and grid quality control take place thanks to Ansys® TurboGrid 14 by running a journal file. Note that the help of this intermediate program, TurboGrid, has proven highly valuable in order to generate high-quality hexahedral grids for a complex rotor in an automatic mode. A previous attempt relying on Ansys® ICEMCFD 14 for this purpose proved to be too complex and remained unsuccessful.

Initial pre-processing is done with Ansys® CFX-Pre 14 by running a session in command line. The CFD simulation relies on the Ansys® CFX solver 14. Finally, post-processing for pressure head and efficiency is realized by the command line instruction ”cfx5mondata” and redirected toward Matlab, which calculates the average value in time.

The settings and models employed for evaluation by CFD are summarized in Table 5.2.

Density	1035 kg/m^3
Viscosity	0.0035 Pa.s
Turbulence Model	RNG k-ϵ
Convergence criteria	RMS 0.0001
Outlet	Open
Min. coeff. loops	3
Max. coeff. loops	6

Table 5.2: Settings used in CFX for the CFD simulation of the pump

Since Ansys® BladeGen is only available on Windows platforms to date, the whole optimization process has been controlled from a Windows PC with one Intel®i5-2500 quadcore processor. A detailed flow chart of the optimization is shown in Fig. 5.4.

5.1.3.1 BladeGen

Ansys® BladeGen uses scripts to actualize the blade geometry data. Such scripts have a fixed format, independent from the designer’s operation sequence in GUI (Graphical User Interface), and denoted by the file extension ”.bgi”.

Since the definition of blade angle in BladeGen is the angle between axial direction and blade direction, all the theoretical β values listed in the previous last chapter have been changed to their complement angle.

Three BladeGen batch scripts have been prepared for the rotor and guide vanes, respectively. These scripts are set in ”Angle/Thickness” mode, which requires blade angles β being defined at least at two spanwise positions, and at least at two chordwise positions for each spanwise position. In the following, an example is presented for defining β using five chordwise positions:

```
Begin AngleCurve
Layer = "Layer1"
HorizDim = Meridional
```

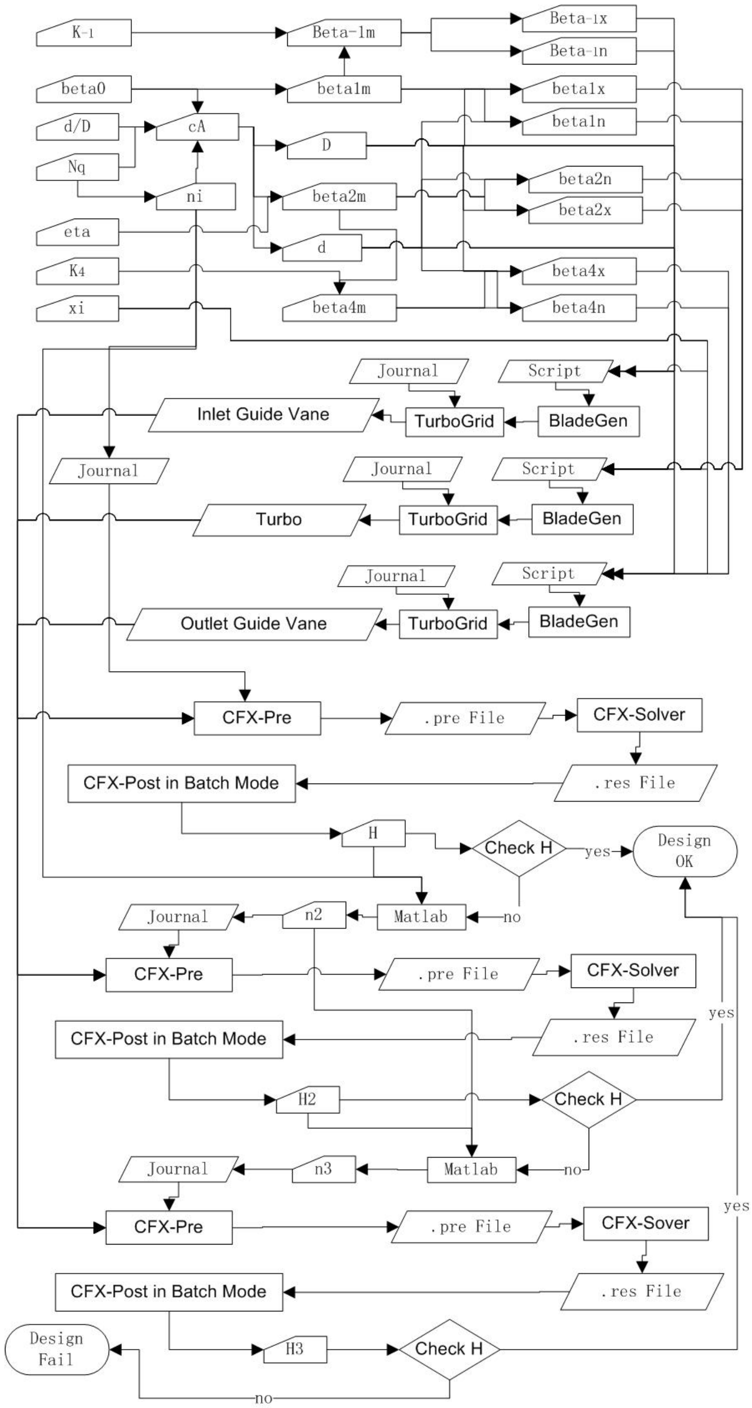

Figure 5.4: Detailed flow chart of the optimization involving seven design variables

```
VertDim = Degree
DefinitionType = Beta Curve
LE_Theta = 0.0000000000
Begin Segment
CurveType = Spline
UpstreamControl = Free
DownstreamControl = Free
Begin Data
( 0.00100000000,74.247998229 )
```

```
( 0.00550000000,71.983104002 )
( 0.00900000000,68.991526641 )
( 0.013500000000,64.884591488 )
( 0.0190000000,58.974722354)
End Data
End Segment
End AngleCurve
```

The first item and last item in the "Data" section correspond to the geometrical variables β_{1_x} and β_{2_x}; the three middle ones are generated by a linear approximation, shown in Eq. (5.2) for the ith increment:

$$\tan \beta_{i_x} = i \tan \beta_{1_x} - (i-1) \tan \beta_{2_x} \tag{5.2}$$

The purpose of this manual interpolation is to override the automation interpolation in BladeGrid, which usually generates an axial-plane separation. In that case, the control points for β_{2_x} and β_{2_n} would be located on different axial planes.

Shaft diameters and shroud diameters at different cross sections are defined separately. Here is an example for defining d and D at a selected axial position:

```
Begin Segment
CurveType = Bezier
UpstreamControl = Free
DownstreamControl = Free
Begin Data
( 0.00100000000,0.005505995 )
( 0.01900000000,0.005505995 )
End Data
End Segment
```

5.1.3.2 TurboGrid

TurboGrid session files (extension ".tse") are prepared for the rotor and guide vanes, respectively. These session files are generated by recording operations in GUI. Some important settings include:

- Set "*ATM Topology Optimizer = On*" to ensure a better tolerance against changes in geometry.

- Set the axial positions of beginning and end of the rotor or guide vane section by:

  ```
  GEO POINT:Low Shroud Point
  AR Location Method = Set A
  Requested ART = -0.03 [m],0.004 [m]
  Visibility = On
  END
  ```

5.1.3.3 CFX

A CFX session file is generated by recording operations in GUI. The simulation domain includes 500 000 to 600 000 hexahedral mesh cells. TurboGrid governs the final mesh size, which varies slightly from design to design. As explained in the previous chapter, it includes

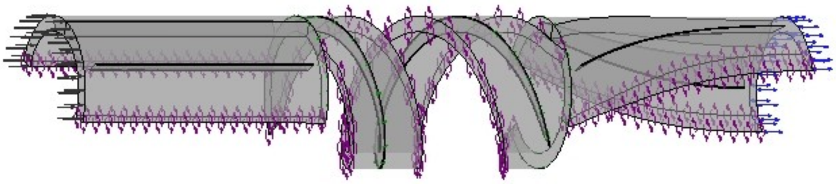

Figure 5.5: Example of a CFD domain considered during the optimization (view in CFX-Pre)

two sections for the inlet guide vane, two sections for the outlet guide vane and one section for the rotor. At the end, the whole CFD domain looks like Fig. 5.5.

A velocity inlet with a prescribed volume flow rate 0.0417 L/s is considered. This is half of the target flow rate of 5 L/min [7], since the CFD simulation considers only a half-pump. ”Opening” boundary condition are chosen to avoid back flow at the beginning of the simulation. A General Grid Interface (GGI) model is used for coupling rotor and guide vanes.

Figure 5.6 shows the hydraulic efficiency obtained by CFD as a function of timesteps. For this specific design, efficiency starts showing periodic features already after six rotations. How many rotations are needed before reaching this stage, depends on the particular design, in particular on the axial velocity c_0 (which is related to cross section area) and also on blade angle β. In the present study, the total simulation duration is systematically set to a total of nine rotations (i.e., 540 time steps). Within this duration, all designs have reached periodicity in practice.

Figure 5.6: Efficiency vs. timestep for a selected design

The simulation of one design takes about 4 hours on a PC with Intel core i5-2500 processor at 3.3 GHz. The number of timesteps needed before observing a periodic solution for pressure head and efficiency, is decided primarily by c_0. For a fixed flow rate, c_0 is directly connected to the cross section area of the pump. As an alternative to a fixed number of impeller rotations, as done in the present study, Eq. (5.3) could be used to control the number of timesteps of a simulation for a specific design, in order to avoid wasting computational capacity in case of early convergence, and to avoid stopping too early for designs that need a longer simulation time. However, for this purpose, the constants a_1, a_2 and a_3 should first be determined empirically.

$$N_{time\ step} = a_1 + a_2 \left(\frac{c_0}{c_{0ini}} \right)^{a_3} \tag{5.3}$$

Finally, another possibility is to use a CEL code in order to check and analyze the evolution of the pressure head in time, and to stop the simulation when periodic oscillations are observed.

5.1.3.4 Matlab

Matlab is used for two tasks:

- Coding the equations from pump design theory listed in Section 4.2. The corresponding code is given in Appendix C.

- Post-processing the ".res" result file to get efficiency, pressure head and hemolysis values.

5.2 Results

Using the hardware discussed previously, the total duration of the optimization was almost exactly five months. At the end, 220 different designs have been evaluated during the optimization process following the procedure discussed previously. The first design computed during the optimization loop had a low hydraulic efficiency of less than 49%. At the end, the very best design shows an efficiency of 65.3%, corresponding to a relative improvement by 25%. This value is still relatively poor compared to those obtained for other applications, for instance large-size centrifugal water pumps. But it must be kept in mind that the considered application is very specific; the dimensions of the device must be kept small, and the prescribed values for flow rate and pressure head are not typical of those associated with a single-stage axial pump. The best set of design parameters obtained by DTB-CFD-O is presented in Table 5.3. The corresponding geometry is shown in Fig. 5.7.

K_{-1}	K_4	β_0	d/D	η_o	N_q	ξ
0.0634	0.7715	18.45	0.721	0.9196	88.85	0.03135

Table 5.3: Set of parameter values for the best design

The resulting fields of instantaneous pressure, velocity magnitude and turbulent kinetic energy for the best design are presented in Figs. 5.8 to 5.10 using volume rendering.

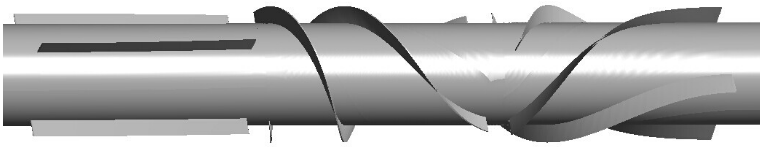

Figure 5.7: Geometry of the best design

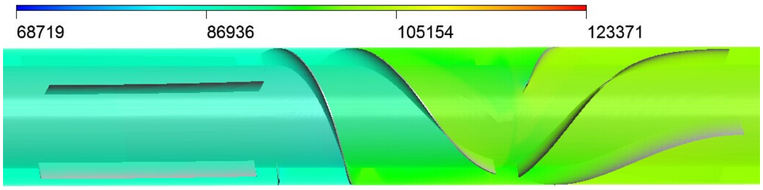

Figure 5.8: Volume rendering of pressure in Pa for the best design

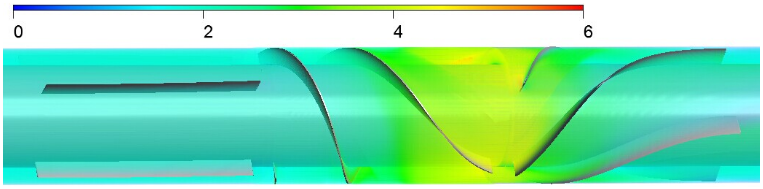

Figure 5.9: Volume rendering of velocity magnitude in m/s for the best design

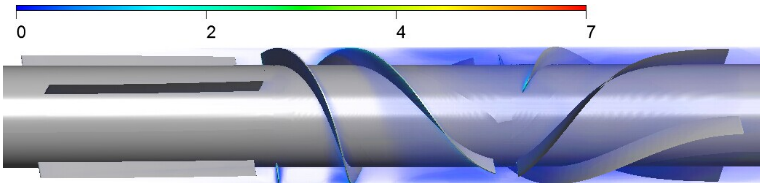

Figure 5.10: Volume rendering of turbulent kinetic energy in m^2/s^2 for the best design

A parallel plot combining input variables and objective (hydraulic efficiency) is shown in Fig. 5.11. In such a plot, commonly used for optimization based on EA, each dashed polyline represents one different design, including along the horizontal axis all the seven real-valued design variables simultaneously. The lower and upper bound values of the parameters found in the optimization are shown individually in the parallel plot for each parameter (seven left vertical axes). When looking at the ranges covered, it is clear that the 220 designs computed by CFD correspond to widely differing technical solutions. The optimal configuration is shown as a thick line.

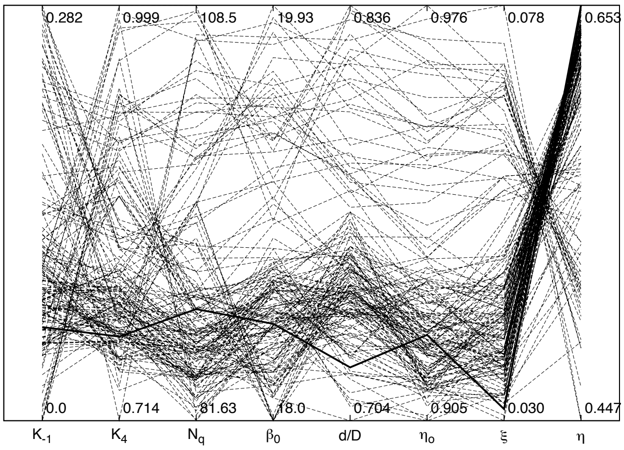

Figure 5.11: Input variables of the optimization and pump efficiency represented using parallel coordinates. Each dashed line is associated with a different design and connects the values of the optimization parameters (7 vertical axes on the left) and the objective function (hydraulic efficiency, last vertical axis on the right).

5.3 Discussion

5.3.1 Range of Input Variables

It is first observed that the optimal values of most design variables, and in particular of ξ are close to the pre-defined minimal values for these parameters. Even if they do not lie on the boundary, it might be helpful to reduce further the minimally allowed values for those parameters in future optimization studies.

5.3.2 Correlation between variables

Figure 5.12 represents the correlations observed during the optimization process for all the variable pairs. Following observations can be drawn from this figure:

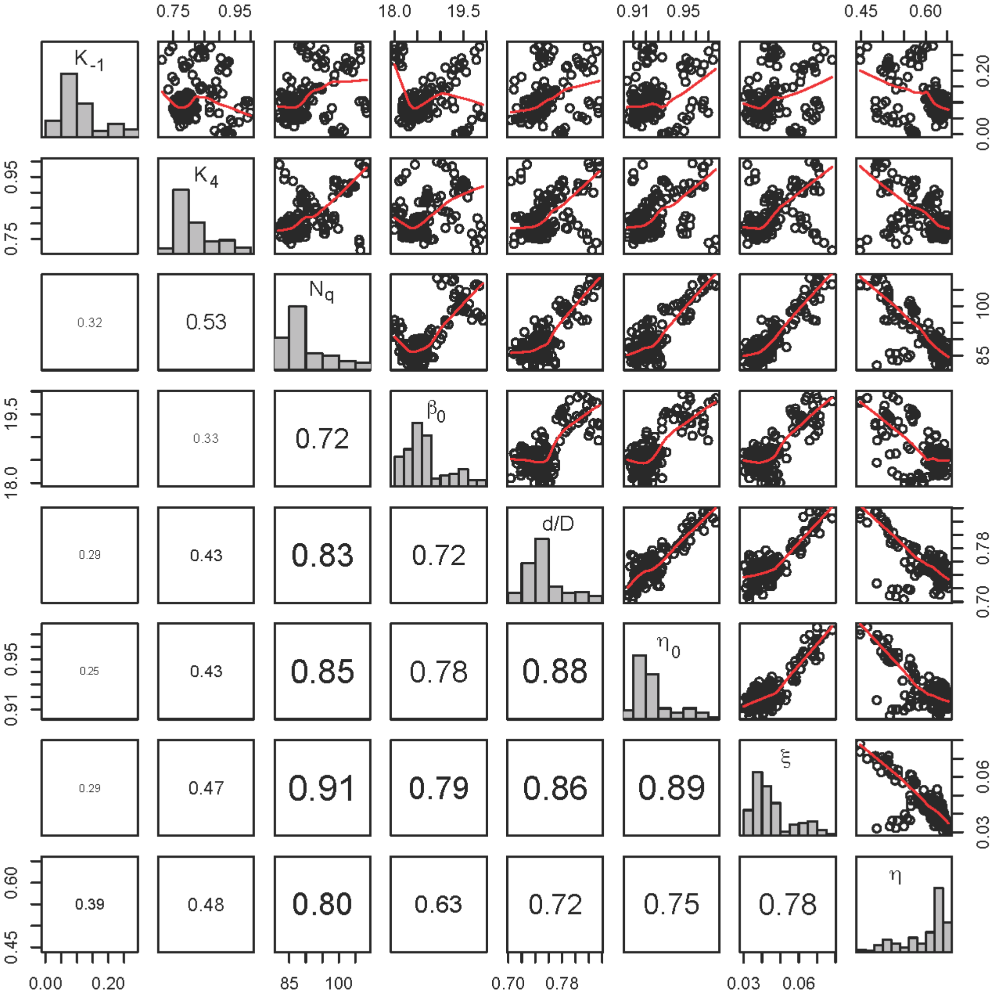

Figure 5.12: Scatter-plot matrix showing the correlation between the input variables. The number represents the correlation between two input variables (along the corresponding column and row, see diagonal for the variable name)

1) The objective (efficiency) is most sensitive to a change in specific speed N_q, and in a second step to tip clearance ξ. As shown in Fig. 5.13, the efficiency increases significantly when reducing the tip clearance within the range prescribed for this variable. On the other hand, the efficiency depends only very little on K_{-1} and K_4.

2) A relatively strong correlation exists between d/D and N_q, with a value of 0.83. However, this value is not sufficient to assume directly a one-to-one correlation between d/D and N_q based on design theory. Both parameters must therefore be kept in the optimization.

3) A very strong correlation exists between ξ and N_q, with a value of 0.91. This might indicate that, in further studies, ξ could be uniquely related to N_q in DTB-CFD-O for an Archimedes screw pump. However, the corresponding relation could not be derived yet. Up to that point, ξ should be kept as well as a design variable of the optimization.

5.3.3 Adding hemolysis as an additional objective

The last purpose of this project was to involve hemolysis as a second, concurrent objective within the optimization. In order to develop high-quality blood pumps, it is in fact absolutely necessary to *simultaneously* 1) maximize hydraulic efficiency, as discussed up to now, but also 2) minimize hemolysis (damage of red blood cells, RBC). It is very well possible that

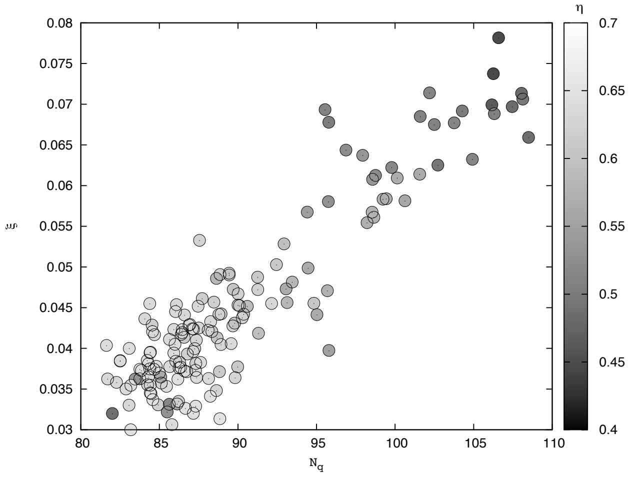

Figure 5.13: η vs. ξ and N_q. Bubble grey level represents the efficiency η.

both objectives might evolve in opposite directions. In fact, the developed optimization procedure would be readily useable for such a concurrent optimization with two (or even more) objectives. Configurations involving two concurrent objectives have been successfully considered in numerous other projects of our group, e.g. [118]. The only real problem, which proved, however, to be considerable, is the availability of a model suitable for CFD and allowing an accurate prediction of hemolysis in such a complex, unsteady flow, as discussed extensively in Chapter 2.

The concurrent optimization involving both objectives is computationally extremely challenging. Computation is still ongoing and results will be attainable in several months, constituting the subject of a dedicated publication. In order to get a preliminary idea of this more complex optimization procedure, the model proposed in [80] has been used to quantify hemolysis for the optimal pump design. Following [80], hemolysis is quantified through an indirect quantity, the modified hemolysis H_L, which is first computed using a transport equation reading:

$$\begin{aligned}\frac{\partial H_L}{\partial t} + \mathbf{v}.\nabla H_L \quad &= \\ &(3.63\times 10^{-7})^{(1/0.785)}\tau^{(2.416/0.785)}(1-H_L) \qquad (5.4)\end{aligned}$$

For this approach, the results in terms of overall hemolysis are finally collected along pathlines using a mass flow-rate-average along the domain outlet (outflow boundary condition of the CFD):

$$\frac{\triangle H_b}{H_b} = \frac{\sum_{\text{outlet cells}} {H_L}^{0.785}\dot{m}_{\text{cell}}}{\sum_{\text{outlet cells}} \dot{m}_{\text{cell}}} \qquad (5.5)$$

Equations (5.4) and (5.5) can be coded using either CFX's User's Fortran or CEL (CFX Expression Language). For the previously obtained optimal design, the model of [80] has been implemented and tested. The result of this simulation is shown in Fig. 5.14. As expected, starting from zero-level (the red blood cells enter the numerical domain without any previous hemolysis), the level of relative hemolysis $\triangle H_b/H_b$ (proportion of hemoglobin leakage outside of the RBC compared to the total initial hemoglobin content) increases rapidly after entering the rotor. Afterwards, it remains at a relatively constant level, with larger values found in regions with a high shear rate. Based on this first simulation, the concurrent optimization involving hemolysis as a second objective is expected to consume approximately 3 times more computing time compared to the single-objective optimization. Using the same hardware and number of processors, this would require around 9 months. In principle, this extremely long computing time can be associated with a shorter user-waiting time by relying heavily on parallel computations. Nevertheless, this remains a very challenging numerical problem. The additional computational cost is due within each CFD evaluation to the additional transport equations that must be solved, to the larger number of sub-iterations needed for each time step, and to the smaller time-steps needed for a stable integration. Additionally, the optimization process must also evaluate more designs in order to obtain a sufficient population of the Pareto front in this higher-dimensional domain.

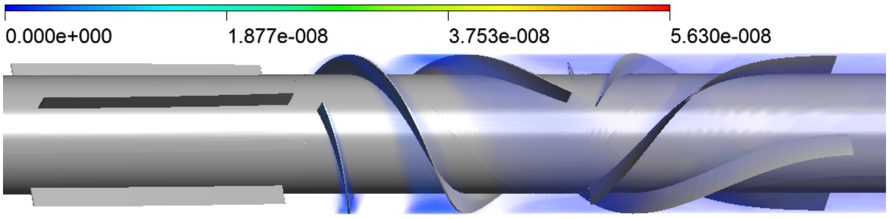

Figure 5.14: Volume rendering of hemolysis level $\triangle H_b/H_b$, as predicted by the model documented in [80].

Figure 5.15 shows that, when computing nine rotations of the pump, the value obtained for hemolysis has fully converged and can therefore be used to evaluate the designs. As already observed in this case for hydraulic efficiency, the pressure head converges to a periodic solution after five impeller rotations (Fig. 5.16).

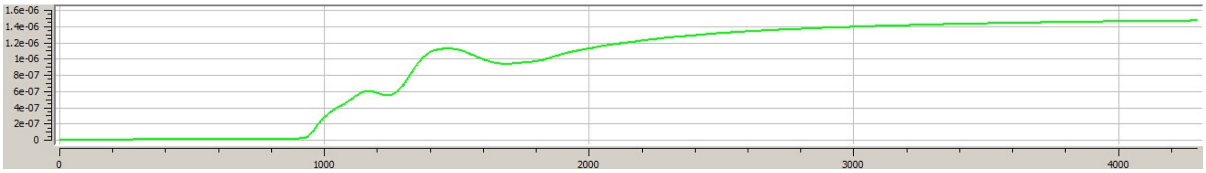

Figure 5.15: Plot of mass-averaged value of hemolysis $\triangle H_b/H_b$ at outlet, as a function of timestep

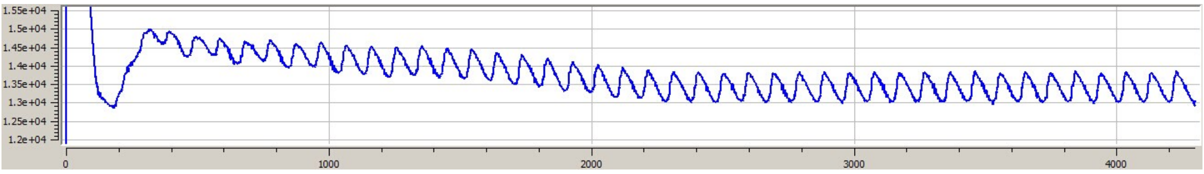

Figure 5.16: Plot of pressure head as a function of timestep

5.4 Conclusions

An automatic optimization process allowing the development of improved rotary blood pumps has been developed and described in this chapter. By combining numerous different tools in a suitable manner, and accepting long simulation times (three months for the first case presented here), considerable progress can be achieved. In particular, the hydraulic efficiency of the pump has been improved by 25% compared to the initial design. Another major finding is that the proposed integration of design theory into the optimization process is indeed possible.

Therefore, design-theory-based CFD-O can indeed be used to fight against the well-known "curse of dimensionality" by reducing the number of independent design variables involved in the optimization. A blind optimization would not have been possible at all for the considered configuration, involving a three-dimensional unsteady flow in a complex geometry.

By using more computer resources, a superior design could probably be achieved, since only 220 different designs have already been evaluated. For this purpose, heavily relying on parallelization is necessary, both for the optimization process (several evaluations running in parallel) and for the CFD evaluations (each CFD simulation being carried out in parallel). This aggressive two-level-parallelization is progressively becoming standard within our group when considering CFD-O.

Further improvements would increase the generality of the optimization procedure. In particular, allowing a non-linear change of $\tan\beta$ between rotor inlet and outlet appears to be a promising extension of the considered approach.

Finally, taking into account hemolysis in the simulation is essential for practical purposes and appears to be possible. However, it requires the availability of a suitable model, with an acceptable accuracy and a good generality.

Chapter 6

Tesla Pump as a Possible Blood Pump

As explained in the introduction, the pump proposed by Nikola Tesla is very unusual but might be advantageous to transport blood, since a low level of hemolysis is expected. In the scientific literature, incompatible statements and contradictory observations can be found, in particular concerning the hydraulic efficiency of this system, from almost 100% to fast nothing. For this reason, several student works considering this issue [10, 123, 124] have taken place in our group during my Ph.D. This chapter summarizes the most important findings obtained during supervision of these studies.

6.1 Theoretical Discussion and Literature Review

In a Tesla pump, the fluid is accelerated by the shear imposed onto it by rotating planes. The average velocity magnitude increases as the fluid passes through the chamber between two planes. The general velocity direction and streamlines in a well-designed system involving only two planes is depicted in Fig. 6.1.

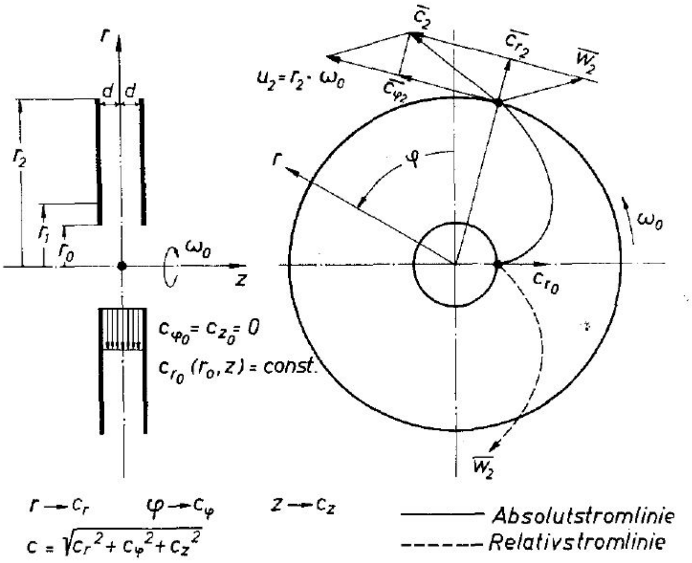

Figure 6.1: Typical velocity and pathlines between two plates [125]

Using the standard design proposed by Tesla, the geometry of a Tesla pump can be parametrized by using only four geometrical variables (see later Fig. 6.8):

1. The gap distance between two planes, h;

2. The inlet radius of the planes, R_i.
3. The outlet radius of the planes, R_a.
4. The gap distance/clearance between the first and last plane and the shell, h_w.

The values of these four parameters have a large influence on the performance of a Tesla pump. It was found in [126] that the highest efficiency value is achieved when the flow state between the plates is laminar. To ensure a laminar flow between plates, a prerequisite is that the gap distance h should not be too large, since the laminar layer (which is close to the wall) has only a limited thickness. The development of the boundary layer of fluid over a simple fixed plane is depicted in Fig. 6.2, and the thickness of it can be estimated by Eq. (6.1).

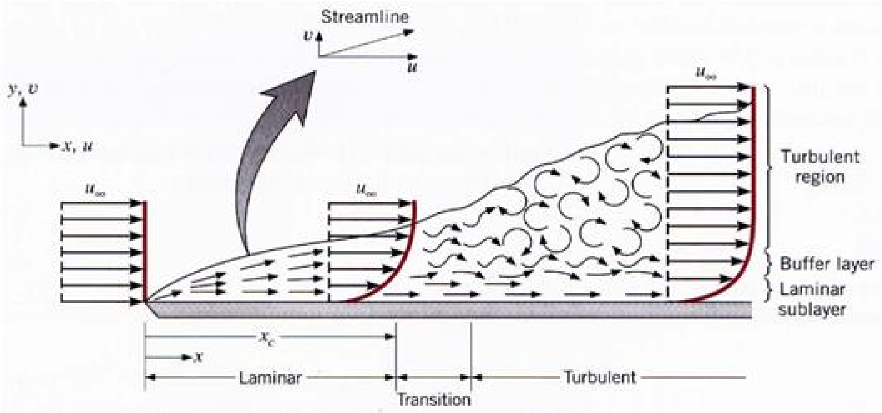

Figure 6.2: Change from laminar to turbulent boundary layer [127]

$$\delta \propto \sqrt{\frac{\nu x}{U_\infty}} \tag{6.1}$$

In a rotating plane system, the evolution of the laminar boundary is more complex. The relative radial velocity between fluid and planes decreases as radius increases, as shown in Figs. 6.3 and (later) 6.9. Simultaneously, the relative tangential velocity also decreases as radius increases, as shown in Fig. 6.10. It was again found in [126] that the thickness of the laminar boundary layer in a rotating plane system is given by Eq. (6.2) as a proportionality rule and does not depend on the radius:

$$\delta \propto \sqrt{\frac{\nu}{\omega_0}} \tag{6.2}$$

Equation 6.2 can be connected to the Ekman number Ek, which characterizes the shape of the velocity profile in a boundary layer [128]:

$$\mathrm{Ek} = \frac{d}{2\delta} = \frac{d}{2}\sqrt{\frac{\omega_0}{\nu}} \tag{6.3}$$

In Eq. (6.2), ω_0 refers to the rotation speed, ν refers to dynamic viscosity of fluid, d refers to the gap distance (in our notation, $d = h$).

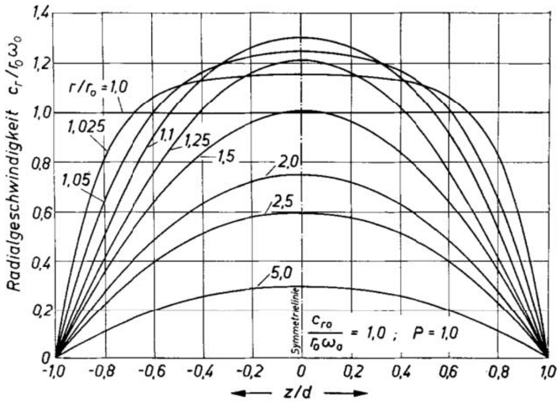

Figure 6.3: Radial velocity profile at different radial positions[125]

The choice of h is often constrained by material properties or construction tolerance. From the point of view of turbomachinery, it must be kept small enough in order to avoid possible back-flow or flow stagnation in the middle region between the disks, as illustrated in Figs. 6.4 and 6.5.

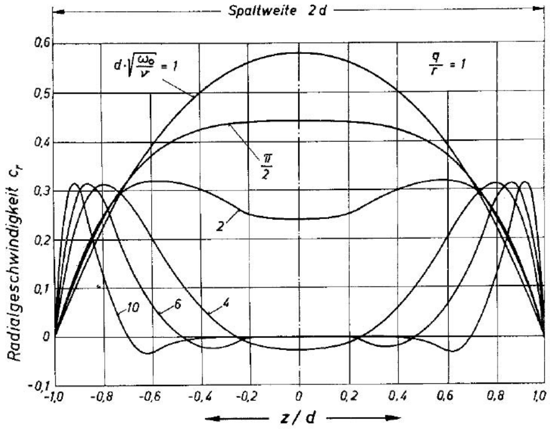

Figure 6.4: Radial velocity profile for different Ekman numbers [125]

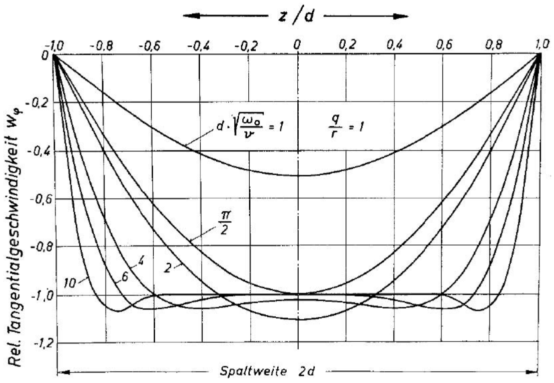

Figure 6.5: Tangential velocity profile for different Ekman numbers [125]

On the other hand, h cannot be extremely small, since this would increase the weight of the system and, more importantly, would decrease the squeeze coefficient and lead to unacceptable frictional losses.

A smaller R_i is advantageous from a constructive point of view. However, a larger R_i may lead to a smoother change in flow direction between the inlet pipe and the entrance between the disks. Hence, some intermediate value of R_i is probably the best choice.

A small value of R_a helps reducing the structural size and weight of the pump, but at the risk of not being able to transfer enough energy to the fluid. On the other hand, a larger R_a leads to structural difficulties, and might be associated to a transition to turbulence between the disks, as exemplified in Fig. 6.6.

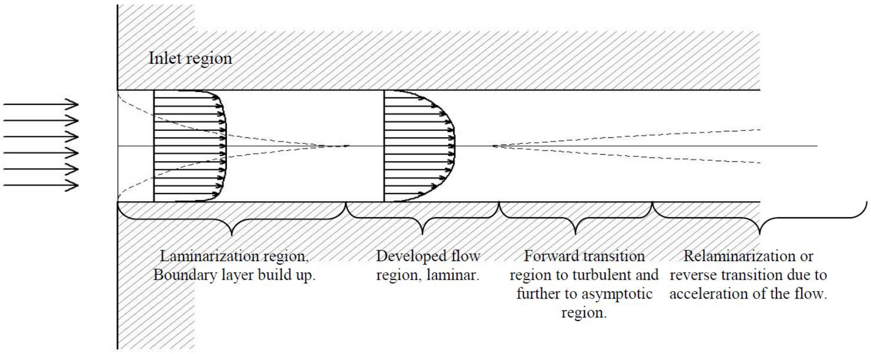

Figure 6.6: Evolution of the velocity profile between two rotating planes [129]

A smaller values of h_w leads to a larger shear rate in the first and last gap, and larger torque resistance on the shaft; it might also lead to an increased hemolysis. On the other hand, a large value of h_w usually leads to a large back-flow region, as shown later in Fig. 6.9.

In another publication [130], the hydraulic losses occurring in a Tesla pump are connected to four main factors:

1. The abrupt change in flow direction at the entrance;
2. The energy dissipation by viscous friction within the fluid between the disks;
3. The turbulent, spiraling vortex structure generated at the outer radial end of the disks;
4. The transition from laminar flow to turbulent flow in the chamber and in the spiral casing.

Concerning those four points:

- A solution to 1) is considered in this chapter;
- 2) appears to be inevitable, but should be relatively small in a laminar flow, compared to standard pumps involving a turbulent flow. The reduction of friction losses is discussed in connection with the first optimization in the next section;
- As discussed above, problem 3) may be reduced or avoided by reducing h and R_a;
- Since the spiral casing is not considered in these first projects, problem 4) is left for future works and might indeed be an important issue.

As explained previously, four design variables h, R_i, R_a and h_w are sufficient to fully describe the geometry of a standard Tesla pump. CFD-O is used in the rest of this chapter to find out the best combination of the values of these four variables.

6.2 Design Optimization for a Tesla pump

Building on top of previous experience [123, 124], two advanced optimization steps are discussed in [10] concerning a Tesla pump. The detailed settings and a thorough description of the results can be found in [10], and are not repeated here in the interest of space. Only the important findings are described and discussed, opening the door for further studies.

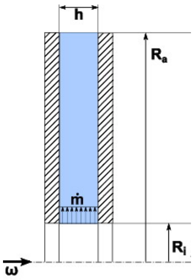

Figure 6.7: Simpler geometry considered for CFD-O of a Tesla pump [10]

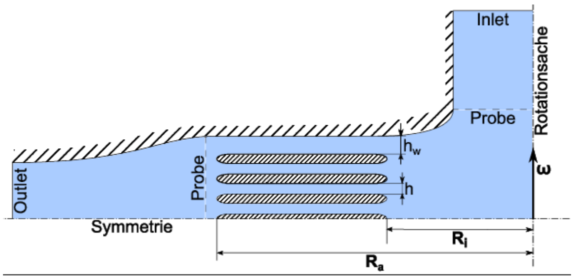

Figure 6.8: Complex geometry considered for CFD-O of a Tesla pump [10]

The first, simple optimization (geometry shown in Fig. 6.7) aims at finding out the highest transport potential (i.e., hydraulic efficiency) for a fluid enclosed between two rotating planes. In this optimization, only hydraulic loss is considered (Point 2 above), all the other three causes for loss are ignored. The maximal efficiency finally obtained is 84.2%, a relatively high value. It is found for fully laminar flow conditions. In that case, the observed loss corresponds simply to the energy dissipation introduced by laminar viscous friction within the fluid.

The second, far more advanced optimization (geometry shown in Fig. 6.8) is for a realistic Tesla pump involving seven plates, a shell case and an inlet with a change in flow direction; this is indeed a complete Tesla pump. A large transition/decelerating chamber between the rotor chamber and the outlet is attached to the geometry, in order to minimize the influence of the outlet boundary in the CFD on the main flow within the pump. Since this is a purely numerical component, the hydraulic losses computed in this transition chamber are removed from the total losses. In the optimization, the SST turbulence model has finally been used. All types of hydraulic losses are considered in the optimization, apart from the loss in the spiral casing chamber (Point 4), since it is difficult to include the geometry of a spiral chamber in an automatic optimization involving mesh grid morphing. The maximal efficiency achieved is now 52.4%. This value is, of course, much lower than the one obtained for the simple (but purely theoretical) design. But it must be kept in mind that this is only a first attempt of CFD-O for a Tesla pump; there is certainly a large improvement potential remaining. Additionally, the value of 52.4% can be compared to the values obtained in Chapter 5 for a far more complex CFD-O: from 49% up to 65.3%; the range is very similar.

Finally, the high efficiency of the optimal design from the first optimization shows that a Tesla pump has a large potential for further design improvement, and might be indeed a good candidate for the design of a pump with a good efficiency. If hemolysis levels are low, such a solution might indeed be a breakthrough to transport blood. The large difference observed between the two optimization setups implies that the hydraulic losses associated to Points 1) and 3) are quite large (about 30%). Therefore, design modifications should be considered to minimize the influence of these two types of losses.

One solution to minimize the hydraulic loss of type 1) is to use non-flat plates. A possible design and method are discussed in Section 6.3.

The hydraulic losses of type 1) and 3) are accompanied by high volumetric losses. A large back-flow region is observed in the first gap (h_w-region), as shown in Fig. 6.9. Using an appropriate sealing at the entrance of the planes, these volumetric losses could be noticeably reduced, thus increasing again the efficiency.

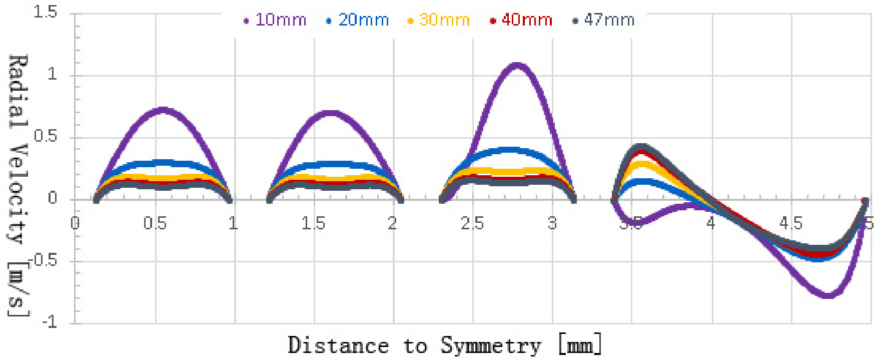

Figure 6.9: Obtained radial velocity profile [10]

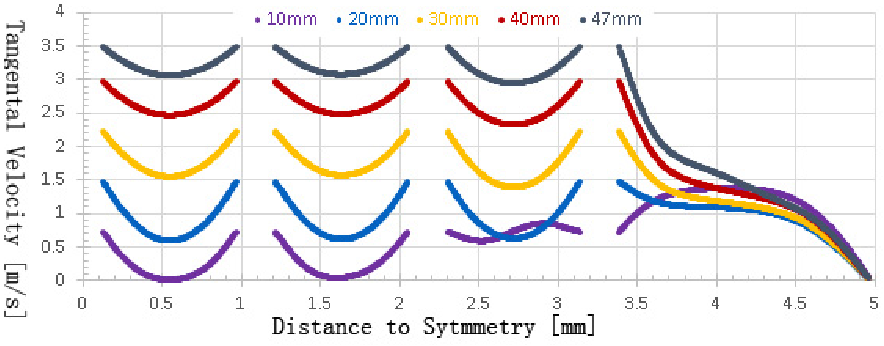

Figure 6.10: Obtained tangential velocity profile [10]

Looking at Fig. 6.11, it may be observed that the group of solutions with the highest efficiency (Pareto front) is associated with the minimal inlet radius R_i prescribed in the optimization. There are two possible reasons: a) using a smaller inner hole at the entrance helps reducing the swirl in the neck region (Fig. 6.12), thus reducing also the level of back-flow; b) the prescribed range for R_i has not been chosen properly, and should include even lower values.

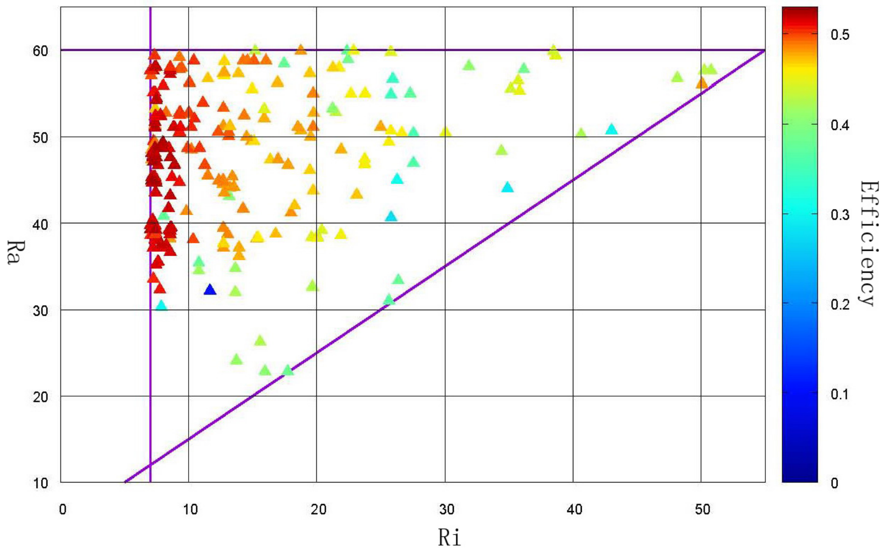

Figure 6.11: Efficiency vs. design variables R_a and R_i in mm [10]

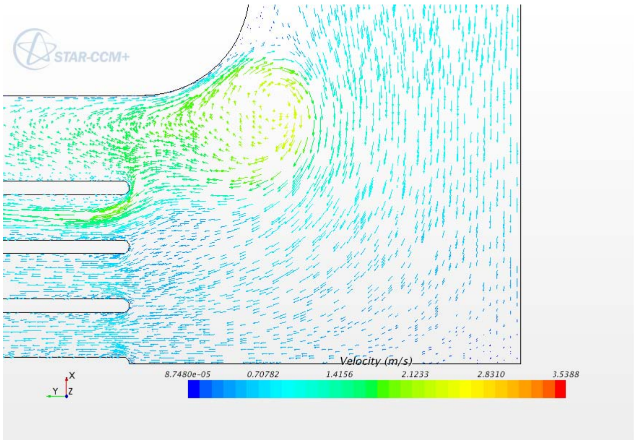

Figure 6.12: Velocity vectors in the neck region [10]

Another interesting observation from Fig. 6.13 is that efficiency is highly dependent on h. One explanation is that, since the number of planes and the total flow rate are fixed in the optimization, the flow rate in each gap is fixed as well. Hence, h completely decides the type and profile of radial velocity between the disks, which is an essential feature to get a high efficiency. However, if the number of planes could be varied in the optimization, a noticeably smaller value for h in combination with a slightly smaller value of R_a should be even better from a theoretical point of view, since a smaller h facilitates the tangential acceleration of fluid and leads to a flatter tangential velocity profile. Such a mixed integer/real-valued optimization is, however, a very difficult task to carry out in automatic mode.

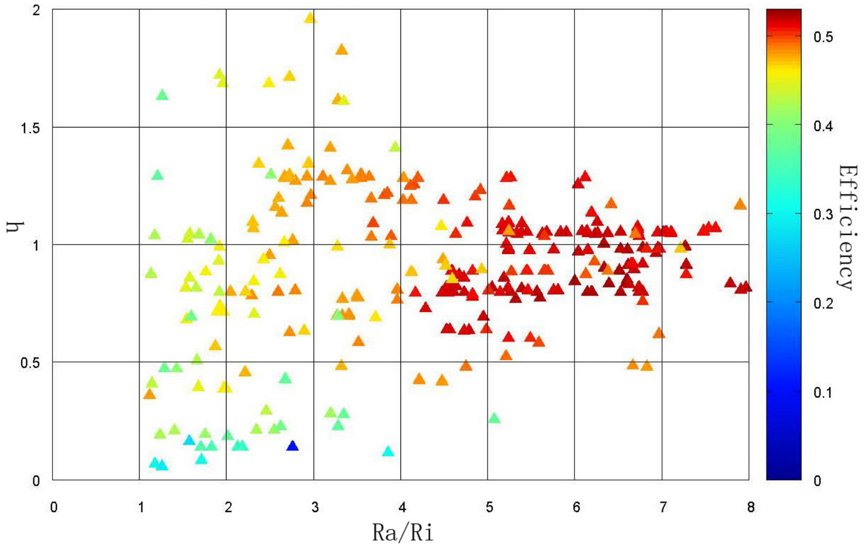

Figure 6.13: Efficiency vs. design variables h (in mm) and R_a/R_i [10]

6.3 Further Improvements

Non-flat plates (Fig. 6.14) are expected to produce a smoother change in flow direction at the inlet, together with a flatter velocity profile farther from the rotation axis. The major difficulty for considering this point in a CFD-O lies in the geometrical complexity of this design, which requires typically many more geometrical input variables compared to a traditional design. Following the method derived, implemented and tested in Chapters 4 and 5, an approach is proposed to reduce the number of design (geometrical) variables to a minimal level, at the end with only four input variables: d_{10}, b_{10}, d_1 and h_w in the simplest case. This method relies again on the ideas underlying DTB-CFD-O of Chapter 4.

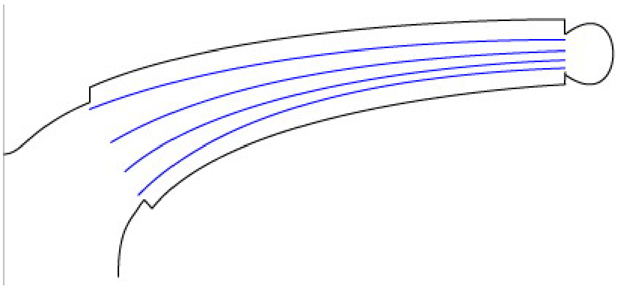

Figure 6.14: Possible Tesla pump with non-flat plates

The outer diameter of the plates, d_{10}, and the height of the trailing edge, b_{10}, are the first two design variables. The diameter d_1 of the middle point (Point 1 in Fig. 6.15) of the entrance edge is taken as the third design variable describing the geometry.

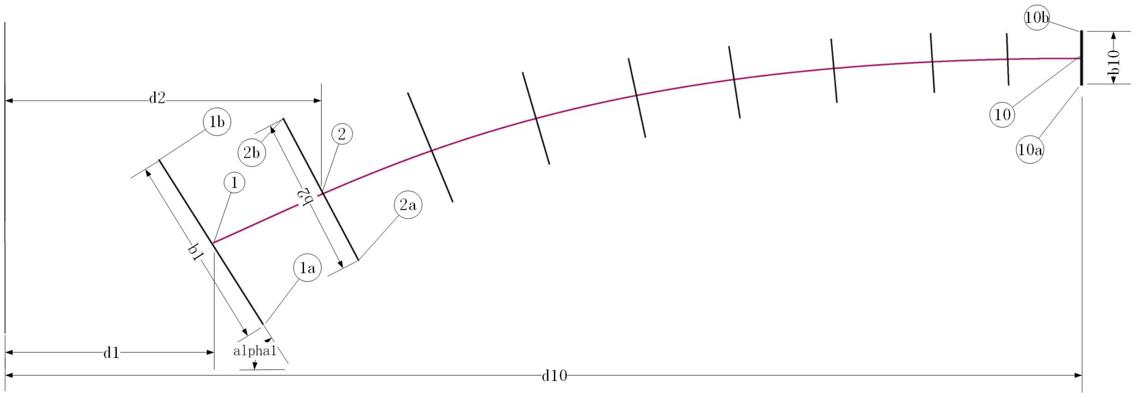

Figure 6.15: Skeleton of the structure of a Tesla-pump with non-flat plates, including a possible parametrization of the geometry for CFD-O

Then, the height of the entrance edge b_1 can be determined by Eq. (6.4), which is based on the assumption of an identical cross-section area of the flow passage along the radial direction.

$$b_1 d_1 = b_{10} d_{10} = b_2 d_2 = b_3 d_3 = ... \tag{6.4}$$

Then, d_2 is computed as one ninth of the difference between d_{10} and d_1: $d_2 = d_1 + 0.1111(d_{10} - d_1)$. At that point, b_2 is determined similarly to b_1 by Eq. (6.4).

Point 1b (the beginning point of the top plate) is located at a fixed position. Then, the position of Point 1a (the beginning point of the bottom plate) can be calculated by:

$$x_{1a} = d_1 + (d_1 - x_{1b}) \tag{6.5}$$

$$y_{1a} = y_{1b} - \sqrt{b_1^2 - 4(d_1 - x_{1b})^2} \tag{6.6}$$

The middle line (the red line in Fig. 6.15) between Point 1 and Point 10 is generated by using a fixed starting slope, gradually reducing this slope to 0. All the edges of the cross-sections (except the first one) are perpendicular to it.

Finally, the positions of all points (1-10a, 1-10b) on the top plate and the bottom plate are all known. The middle plates can be discretized by equidistant points on the cross-section edges. For simplicity, it is proposed to take a constant clearance h_w as the fourth and last design variable. Then, the whole geometry of the pump is described with four parameters, but without inlet pipe and spiral casing. Adding these two important components in the optimization will certainly lead to an optimization with almost 10 design parameters, that will be left for future projects.

Chapter 7

Conclusions and Perspectives

7.1 Conclusions

7.1.1 Numerical Hemolysis Prediction Models Need Improvement

Different numerical hemolysis prediction models have been reviewed, partly validated and compared in this dissertation. Most existing models are only derived from the simple power law equation, which is based on macroscopic measurements of hemolysis followed by curve fitting, without any consideration of the real properties of blood. Eulerian formulations of existing models have been introduced and tested during this PhD. All these models, including the new approach, show specific advantages and drawbacks, and there is unfortunately no clear guidelines concerning applicability or limitation of those models. An even worse difficulty is the lack of well-documented experimental data suitable for a final check or improvement of those models under realistic conditions!

Based on a first simple validation, one simple Lagrangian power-law model (Model C) performs best, followed closely by a much more complex Lagrangian stain-tensor-based model (Model E). Considering that Eulerian models are much more suitable for coupling with CFD simulation (an Eulerian model with scalar transport equation is directly compatible with industrial CFD tools), corresponding formulations have been derived, leading to the Eulerian versions of Model C and E. Unfortunately, the model with the highest potential in principle, the Eulerian version of Model E, can not be implemented yet into any existing CFD solvers (including OpenFOAM), due to the structure of the resulting equations. For this reason, most presented results have been obtained with the Eulerian version of method C, though this model did not perform well in all tests.

One advantage of model C is that, by modifying the values of a and b in Eqs.(2.33)-(2.34), the model sensitivity to peak shear stress and average shear stress can be separately adjusted and balanced. This feature makes model C a good candidate for further optimization(s) based on parameter fitting, aiming at better prediction of trends but also of absolute values from relevant experiments, such as those obtained in a blood pump when varying the rotation speed and flow-rate in a well-instrumented experiment: such data are missing yet, but will hopefully be released by the FDA in the next months.

Though model C is highly flexible, it is quite simple. In contrary to this, the nature of blood and the processes underlying hemolysis are extremely complex. A direct physical modeling of the microscopic nature of hemolysis is not possible in CFD.

The need for further experiments under well-defined, reproducible and well-documented conditions is in urgent demand. Although this does not necessarily mean that a predictive model for hemolysis should describe all the microscopic mechanisms, a more complex model has obviously a larger chance to be more universally valid and more accurate than the current ones.

7.1.2 DTB-CFD-O is Feasible

An extended automatic optimization method for a blood pump has been developed and applied in this Thesis to a a screw-type axial-flow pump. By combining pump design theory with many numerical tools in a suitable manner, considerable progress can be achieved. The major finding is that the proposed integration of design theory into the design process is indeed useful. Therefore, design-theory-based Optimization based on Computational Fluid Dynamics (DTB-CFD-O) can indeed be used to fight against the well-known ”curse of dimensionality”, by reducing the number of independent parameters involved in the optimization. A blind optimization was not possible before for the considered configuration, involving a three-dimensional unsteady flow in a complex geometry, due to the tremendous computational cost.

Current results are nevertheless still constrained by the performance of the employed hardware and the availability of software licenses. By using more computer resources, an even better design could probably be achieved, since only 220 different designs have been evaluated yet. For this purpose, heavily relying on parallelization is necessary, both for the optimization process (several evaluations running in parallel) and for the CFD evaluations (each CFD simulation being carried out in parallel).

Some correlations between the design variables have been found during the optimization. These findings, though still preliminary, may be helpful to speed-up further by extending design theory, thus reducing the number of input variables for future optimizations.

Increasing further the complexity of the optimization, i.e., involving more design variables in order to obtain a more detailed description of the pump, highly depends on the availability of corresponding computational facilities; there is theoretically no other obstacle to this process. It is expected that a full 3-dimensional optimization with unsteady flow of a real, commercial geometry will be possible before end of the current decade. If an open-source tool like OpenFOAM can be used in a robust manner for CFD, and provided that high-quality open-source tools become available for geometry parametrization and complex meshing, DTB-CFD-O will have a broad range of applications.

7.1.3 The Tesla Blood Pump Deserves Further Investigation

The optimization of the simple design involving only two rotating planes shows that this type of rotor has a potential to reach a sufficient hydraulic efficiency. Considering the lower shear levels found in the system, a Tesla pump might then be a very good candidate for blood transport.

Unfortunately, up to now, no comprehensive design theory has been developed for a Tesla pump. Most existing designs show a much lower efficiency than a standard pump, owning to the different types of hydraulic losses mentioned in Section 6.1. The proper development of a design method for advanced Tesla pumps, involving non-flat disks, is of major importance. This will require much mathematical description and corresponding experimental work.

In parallel to this work, CFD-O remains suitable for optimization, even before getting a complete design theory. In fact, the results of design theory and of CFD-O will be mutually beneficial to each other. It is expected that the results of CFD-O for advanced Tesla pumps allowing for non-conventional designs will be very promising.

7.2 Perspectives

7.2.1 Numerical Hemolysis Prediction: A Strain-scalar-based Model

Although the Eulerian version of Arora's tensor-based model might be the best solution for accurate numerical hemolysis predictions, a strain-scalar-based Eulerian model is more likely to fit industrial applications in an acceptable computing time, for instance using ANSYS for CFD.

Such an Eulerian strain-scalar based hemolysis model should include equations to describe properly the two most important issues:

- the relationship between shear stress and membrane tension (Eq. 7.1), where s refers to local membrane tension, τ refers to local shear stress;
- and the relationship between membrane tension and hemolysis (Eq. 7.2), where H_t refers to local hemolysis rate.

$$\frac{ds}{dt} = F_1(\tau, s) \tag{7.1}$$

$$\frac{dH_t}{dt} = F_2(s, H_t, t) \tag{7.2}$$

These equations are expected to be derived from a combination of extensive experimental studies and theoretical work. If possible, the following aspects could be considered when formulating the equations. When taking into account hemolysis history, Eq. (7.1) will read:

$$\frac{ds}{dt} = F_1'(\tau, s, H_t) \tag{7.3}$$

Taking into account membrane hardening h (though it is not clear yet if this aspect is important for blood pumps), an additional transport equation must be introduced:

$$\frac{dh}{dt} = F_0(\tau, s) \tag{7.4}$$

Then, the new function F_1 will look like:

$$\frac{ds}{dt} = F_1''(\tau, s, H_t, h) \tag{7.5}$$

The hemolysis equation F_2, however, should also possibly be affected by membrane hardening, leading to:

$$\frac{\partial H_t}{\partial t} = F_2''(s, H_t, h) \tag{7.6}$$

After getting an explicit formulation for these equations, an optimization based on parameter fitting may be carried out. But this requires of course the availability of high-quality experimental results...

7.2.2 More Flexible Coding Platform

Although it is unclear, which hemolysis model will be retained at the end, it is highly probable that this model will involve complex equations and complex terms within each equation, due to the complexity of the process. Unfortunately, all commonly used CFD solvers, such as Fluent, CFX, or even OpenFOAM, are currently not flexible enough to support such equations.

One possible solution is to include a real-time communication between the CFD solver and outer mathematical tools, such as Matlab, Maple, or own routines. Another solution involves an in-depth modification of the CFD-solver, which is only possible for open-source solvers, such as OpenFOAM.

7.2.3 Meshing

Though Ansys® BladeGen und TurboGrid are powerful and adequate tools for automatic meshing when optimizing turbomachines, other possibilities also deserve investigation. One possibility is to carry out a two-stage optimization. The first stage is a ”coarse” optimization, with a low computational cost, in which a design ”close to the best design” is found, generating new geometries and new meshes for each individual. In the second stage, the design, and thus the geometry and the mesh, will not be varied much any more. Therefore, morphing becomes a convenient alternative. Mesh morphing without re-meshing and without topology change is then very efficient. Such a task may even be carried out by already existing commercial tools, such as Sculptor®, or by built-in add-ons in CFD codes.

One advantage of a topology-keeping morph lies in the fact that node and cell numberings are kept. It is then extremely easy to project the data from an existing result file to the new mesh. Hence, the new simulation for the new design can be restarted from the previous solution, saving much computational time.

7.2.4 Design-theory-based Optimizer Algorithm

Current DTB-CFD-O only considers design theory to interconnect design and geometrical variables, but is not included into the evaluation process. Further development of DTB-CFD-O may consider the possibility of a ”design-based optimizer”, which would integrate design theory into the operators of the evolutionary algorithm itself. For instance, the fitness of a design individual would not only be estimated by its objective values, but simultaneously also by other factors, derived from design theory.

Bibliography

[1] E. Birks, "The comparative use of ventricular assist devices: Differences between Europe and the United States," *Texas Heart Institute Journal*, vol. 37(5), pp. 585–587, 2010.

[2] J. Kirklin, D. Naftel, R. Kormos, L. Stevenson, F. Pagani, M. Miller, K. Ulisney, T. Baldwin, and J. Young, "Second INTERMACS Annual Report: More than 1000 primary left ventricular assist device implants," *Journal of Heart and Lung Transplantation*, vol. 29(1), pp. 1–10, 2010.

[3] A. collective, "Ventricular assist devices - global pipeline analysis, competitive landscape and market forecasts to 2017," Market Report, GlobalData, Dublin, 2011.

[4] K. Watanabe, S. Ichikawa, T. Asai, T. Motomura, A. Hata, S. Ito, and Y. Nose, "Centrifugal blood pump with a hydraulically-levitated impeller for a permanently implantable biventricular assist device," *Artificial Organs*, vol. 28(6), pp. 556–563, 2004.

[5] Y. Kang, M. Kim, K. Son, C. Lim, H. Son, S. Yoon, H. Kwon, and S. Yang, "Experimental investigation of pulsatility effect on the deformability and hemolysis of blood cells," *Artificial Organs*, vol. 34(4), pp. E103–E109, 2010.

[6] Y. Sawa, E. Tatsumi, A. Funakubo, T. Horiuchi, K. Iwasaki, A. Kishida, and H. Watanabe, "Journal of Artificial Organs 2008: The year in review," *Journal of Artificial Organs*, vol. 12(1), pp. 1–7, 2009.

[7] H. Hoshi, T. Shinshi, and S. Takatani, "Third-generation blood pumps with mechanical noncontact magnetic bearings," *Artificial Organs*, vol. 30(5), pp. 324–338, 2006.

[8] N. Tesla, *Fluid Propulsion.* Patent US 1061142, 1913.

[9] C. Jhun, R. Newswanger, J. Cysyk, B. Lukic, W. Weiss, and G. Rosenberg, "Tesla-based blood pump and its applications," *Journal of Medical Devices*, vol. 7(4), p. 040917, 2013.

[10] S. Engel, "Optimizing the hydraulic efficiency of a Tesla pump," Master's Thesis, "Otto von Guericke" University of Magdeburg, LSS-M05/14, 2014.

[11] L. Goubergrits, "Numerical modeling of blood damage: current status, challenges and future prospects," *Expert Rev. Med. Devices*, vol. 3(5), pp. 527–531, 2006.

[12] M. Giersiepen, L. Wurzinge, R. Opitz, and H. Reul, "Estimation of shear stress-related blood damage in heart valve prostheses–in vitro comparison of 25 aortic valves," *Artificial Organs*, vol. 5, pp. 300–306, 1990.

[13] D. Arora, *Computational hemodynamics: Hemolysis and viscoelasticity.* Dissertation, Rice University, 2006.

[14] D. Thévenin and G. Janiga, *Optimization and Computational Fluid Dynamics*. Springer, 2009.

[15] G. Janiga, *Flow Optimization using Computational Fluid Dynamics*. Habilitation Thesis, University of Magdeburg, 2011.

[16] M. Mohamed, *Design Optimization of Savonius and Wells Turbines*. Dissertation, "Otto von Guericke" University of Magdeburg, 2011.

[17] P. Blackshear and G. Blackshear, *Handbook of Bioengineering*, ch. Mechanical hemolysis. (R. Skalak and S. Chien, Eds.) McGraw Hill, NY, USA, 1987.

[18] J. Yee and H. Mei, "Cell-membrane and rheological mechanism: dynamic osmotic hemolysis of human erthrocytes and repair of ghosts, as studied by resistive pulse spectroscopy," *Biorheology*, vol. 15, pp. 321–339, 1978.

[19] G. Kesmarky, P. Kenyeres, M. Pabai, and K. Toth, "Plasma viscosity: a forgotten variable," *Clin. Hemorheol. Microcirc.*, vol. 39(1-4), pp. 243–246, 2008.

[20] G. Thurston, "Viscoelasticity of human blood," *Biophysical Journal*, vol. 12, pp. 1205–1217, 1972.

[21] S. Chien, "Shear dependence of effective cell volume as determinant of blood viscosity," *Science*, vol. 168, p. 22, 1970.

[22] A. Leuprecht and K. Perktold, "Numerical studies of viscoelastic blood flow behaviour in large arteries," in *Proceedings of 4th International Symposium on Computer Methods in Biomechanics and Biomedical Engineering*, (Lisbon, Portugal), pp. 737–742, 1999.

[23] J. Stoltz, M. Singh, and P. Riha, *Hemorheology in Practice*. Amsterdam: IOS Press, 1999.

[24] N. Antonova, "On some mathematical models in hemorheology," *Biotechnology and Biotechnological Equipment*, vol. 26, pp. 3286–3291, 2012.

[25] H. Schmid-Schoenbein and R. Wells, "Fluid drop-like transition of erythrocytes under shear," *Science*, vol. 165, pp. 288–291, 1969.

[26] R. Hochmuth, "Properties of red blood cells," in *Handbook of Bioengineering* (R. Skalak and S. Chine, eds.), ch. 12.1-12.7, New York: McGraw-Hill, 1987.

[27] A. Walter, H. Rehage, and H. Leonhard, "Shear-induced deformations of polyamide microcapsules," *Colloid Polym. Sci.*, vol. 278, pp. 169–175, 2000.

[28] P. Bronkhorst, E. Nijhof, and J. Sixma, "Parametrization of the deformation curve as a tool for standardization and interpretation of ektacytometric measurements," *Clinical Hemorheology*, vol. 15(6), pp. 803–816, 1995.

[29] M. Condon, J. Kim, E. Deitch, G. Machiedo, and Z. Spolarics, "Appearance of an erythrocyte population with decreased deformability and hemoglobin content following sepsis," *Am J Physiol Heart Circ Physiol*, vol. 284(H), pp. 2177–2184, 2003.

[30] P. Kenyeres, M. Rabai, A. Toth, G. Kesmarky, Z. Marton, T. Alexy, and K. Toth, "Reviewing data reduction methods for ekacytometry," *Clinical Hemorheology and Microcirculation*, vol. 47, pp. 143–150, 2011.

[31] O. Baskurt and H. Meiselman, “Analyzing shear stress-elongation index curves: Comparison of two approaches to simplify data presentation,” *Clinical Hemorheology and Microcirculation*, vol. 31, pp. 23–30, 2004.

[32] O. Baskurt, M. Hardeman, M. Uyuklu, P. Ulker, M. Cengiz, N. Nemeth, S. Shin, T. Alexy, and H. Meiselman, “Parameterization of red blood cell elongation index - shear stress curves obtained by ektacytometry,” *Scandinavian Journal of Clinical and Laboratory Investigation*, vol. 69(7), pp. 777–788, 2009.

[33] S. Ookawara, A. Yano, K. Ogawa, and K. Taniguchi, “Estimate of red cell deformability and plasma viscosity based on flow curve,” *Bioengineering, Food and Natural Products*, vol. 47(1), pp. 230–239, 2001.

[34] N. Watanabe, D. Sakota, K. Ohuchi, and S. Takatani, “Deformability of red blood cells and its relation to blood trauma in rotary blood pumps,” *Artificial Organs*, vol. 31(5), pp. 352–358, 2007.

[35] N. Watanabe, Y. Arakawa, A. Sou, H. Kataoka, K. Ohuchi, T. Fujimoto, and S. Takatani, “Deformability of human red blood cells exposed to a uniform shear stress as measured by a cyclically reversing shear flow generator,” *Physiological Measurement*, vol. 28, pp. 531–545, 2007.

[36] P. Maffettone and M. Minale, “Equation of change for elliposoidal drops in viscous flow,” *J. Non-Newtonian Fluid Mech.*, vol. 78, pp. 227–241, 1998.

[37] R. Hochmuth, P. Worthy, and E. Evans, “Red cell extensional recovery and the determination of membrane viscosity,” *Biophys J.*, vol. 26, pp. 101–114, 1979.

[38] Y. Yoon, J. Kotar, G. Yoon, and P. Cicuta, “The nonlinear mechanical response of the red blood cell,” *Phys. Biol.*, vol. 5(3), p. 036007, 2008.

[39] T. Fischer, M. Stoehr-Liesen, and H. Schmid-Schoenbein, “The red cell as a fluid droplet: tank-tread-like motion of the human erythrocyte membrane in shear flow,” *Science*, vol. 202, p. 894, 1978.

[40] S. Keller and R. Skalak, “Motion of a tank-treading ellipsoidal particle in a shear flow,” *J. Fluid Mech.*, vol. 120, pp. 27–47, 1982.

[41] R. Tran-Son-Tay, S. Sutera, G. Zahalak, and P. Rao, “Membrane stress and internal pressure in a red blood cell freely suspended in a shear flow,” *Biophys. J.*, vol. 51, pp. 915–924, 1987.

[42] P. Olla, “The role of tank-treading motions in the transverse migration of a spheroidal vesicle in a shear flow,” *J. Phys. A: Math. Gen.*, vol. 30, pp. 317–329, 1997.

[43] P. Olla, “The lift on a tank-treading ellipsoidal cell in a shear flow,” *J. Phys. 2 France*, vol. 7, pp. 1533–1540, 1997.

[44] S. Feng, R. Skalak, and S. Chien, “Velocity distribution on the membrane of a tank-treading red blood cell,” *Bulletin of Mathematical Biology*, vol. 51(4), pp. 449–465, 1989.

[45] T. Fischer, “On the energy dissipaton in a tank-treading human red blood cell,” *Biophys. J.*, vol. 32, pp. 863–868, 1980.

[46] H. Noguchi and G. Gompper, “Fluid vesicles with viscous membranes in shear flow,” *Physical Review Letters*, vol. 93, pp. 258102(1–4), 2004.

[47] H. Noguchi and G. Gompper, “Swinging and tumbling of fluid vesicles in shear flow,” *Physical Review Letters*, vol. 98, pp. 128103(1–4), 2007.

[48] Y. Sui and Y. Chew, “Dynamic motion of red blood cells in simple shear flow,” *Physics of Fluids*, vol. 20, pp. 112106(1–10), 2008.

[49] A. Yazdani, R. Kalluri, and P. Bagchi, “Tank-treading and tumbling frequencies of capsules and red blood cells,” *Physical Review*, vol. E(83), pp. 046305(1–12), 2001.

[50] H. Noguchi, “Swinging and synchronized rotations of red blood cell in simple shear flow,” *Physical Review E*, vol. 80, pp. 021902(1–8), 2009.

[51] H. Noguchi, “Dynamic modes of red blood cells in oscillatory shear flow,” *Physical Review E*, vol. 81, pp. 061920(1–9), 2010.

[52] K. Tsubota and S. Wada, “Effect of the natural state of an elastic cellular membrane on tank-treading and tumbling motions of a single red blood cell,” *Physical Review E*, vol. 81, pp. 011910(1–10), 2010.

[53] R. Rand, “Mechanical properties of the red cell membrane: Viscoelastic breakdown of the membrane,” *Biophys J.*, vol. 4, pp. 303–316, 1964.

[54] G. Arwatz and A. Smits, “A viscoelastic model of shear-induced hemolysis in laminar flow,” *Biorheology*, vol. 50, pp. 45–55, 2013.

[55] E. Evans, R. Wauch, and L. Melnik, “Elastic area compressibility modulus of red cell membrane,” *Biophysical Journal*, vol. 16, pp. 585–595, 1976.

[56] M. Nakamura and S. Wada, “Does fluid shear stress represent the degree of a red blood cell deformation?,” in *3rd ECCOMAS Thematic Conference on Computational Vision and Medical Image Processing*, (Olhao, Algarve; Portugal), 2011.

[57] T. Mizuno, T. Tsukiya, Y. Taenaka, E. Tatsumi, T. Nishinaka., H. Ohinishi, M. Oshikawa, K. Sato, K. Shioya, Y. Takewa, and H. Takano, “Ultrastructural alterations in red blood cell membranes exposed to shear stress,” *ASAIO Journal*, vol. 48, pp. 668–670, 2002.

[58] M. Kameneva, A. Uendar, J. Antaki, M. Watach, J. Calhoon, and H. Borovetz, “Decrease in red blood cell deformability caused by hypothermia, hemodilution, and mechanical stress: Factors related to cardiopulmonary bypass,” *ASAIO Journal*, vol. 45, pp. 307–310, 1999.

[59] S. Lee, K. Ahn, S. Lee, K. Sun, P. Goedhart, and M. Hardeman, “Shear induced damage of red blood cells monitored by the decrease of their deformability,” *Korea-Australia Rheology Journal*, vol. 16(3), pp. 141–146, 2004.

[60] S. Lee, M. Kameneva, J. Dobbe, M. Hardeman, K. Ahn, and S. Lee, “Strain hardening of red blood cells by accumulated cyclic supraphysiological stress,” *Artificial Organs*, vol. 31(1), pp. 80–86, 2007.

[61] N. Yokoyama, D. Sakota, E. Nagaoka, and S. Takatani, “Alterations in red blood cell volume and hemoglobin concentration, viscoelastic properties, and mechanical fragility caused by continuous flow pumping in calves,” *Artificial Organs*, vol. 35(8), pp. 791–799, 2011.

[62] M. Zeitz and P. Sens, “Reversibility of red blood cell deformation,” *Physical Review*, vol. E85, pp. 051904(1–9), 2012.

[63] A. Srivastav, X. Grandchamp, G. Coupier, and T. Podgorski, “Shear-induced diffusion in a red blood cell suspension,” *Computer methods in Biomechanics and Biomedical Engineering*, vol. 15(S1), pp. 34–35, 2012.

[64] M. Tan, D. Le, and K. Chiam, “Hydrodynamic diffusion of a suspension of elastic capsules in bounded simple shear flow,” *Soft Matter*, vol. 8, pp. 2243–2251, 2012.

[65] T. Krüger, *Computer Simulation Study of Collective Phenomena in Dense Suspensions of Red Blood Cells under Shear.* Dissertation, Bochum University, 2012.

[66] L. Leverett, J. Hellums, C. Alfrby, and E. Lynch, “Red blood cell damage by shear stress,” *Biophysical Journal*, vol. 12, p. 272, 1972.

[67] S. Hashimoto, “Erythrocyte destruction under periodically fluctuating shear rate: Comparative study with constant shear rate,” *Artificial Organs*, vol. 13(5), pp. 458–463, 1989.

[68] C. Pozrikidis, “Numerical simulation of the flow-induced deformation of red blood cell,” *Annals of Biomedical Engineering*, vol. 31, pp. 1194–1205, 2003.

[69] M. Dupin, I. Halliday, C. Care, L. Alboul, and L. Munn, “Modeling the flow of dense suspensions of deformable particles in three dimensions,” *Physical Review*, vol. E75, pp. 066707(1–17), 2007.

[70] Y. Liu, L. Zhang, X. Wang, and W. Liu, “Coupling of Navier-Stokes equations with protein molecular dynamics and its application to hemodynamics,” *International Journal for Numerical Methods in Fluids*, vol. 46, pp. 1237–1252, 2004.

[71] S. Bhavsar, R. Graefe, S. Fabbri, E. Schkommodau, D. Baykut, R. Pfluger, and U. Steinseifer, “Hydraulic and hemodynamic performance of an innovative fully implantable hollow rotor LVAD,” in *Proc. 20th Congress of the International Society of Rotary Blood Pump*, (Istanbul, Turkey), 2012.

[72] M. Taskin, K. Fraser, T. Zhang, C. Wu, B. Griffith, and Z. Wu, “Evaluation of eulerian and lagrangian models for hemolysis estimation,” *ASAIO Journal*, vol. 58, pp. 363–372, 2012.

[73] A. Arvand, M. Hormes, and H. Reul, “A validated computational fluid dynamics model to estimate hemolysis in a rotary blood pump,” *Artificial Organs*, vol. 29(7), pp. 531–540, 2005.

[74] M. Pinotti and E. Rosa, “Computational prediction of hemolysis in a centrifugal ventricular assist device,” *Artificial Organs*, vol. 19, pp. 267–273, 1995.

[75] C. Bludszuweit, “Model for a general mechanical blood damage prediction,” *Artificial Organs*, vol. 19, pp. 583–589, 1995.

[76] L. Wurzinge, R. Opitz, and H. Schmid-Schoenbein, “Platelet and coagulation parameters following milli-second exposure to laminar shear stress,” *Thromb. Haemost.*, vol. 54, pp. 381–386, 1985.

[77] L. Wurzinge, R. Opitz, and H. Eckstein, “Mechanical blood trauma: an overview,” *Angeiologie*, vol. 38, pp. 81–97, 1986.

[78] D. A. M. Behr and M. Pasquali, “Hemolysis estimation in a centrifugal blood pump using a tensor-based measure,” *Artificial Organs*, vol. 30, no. 7, pp. 539–547, 2006.

[79] D. Wachter and P. Verdonck, “Numerical calculation of hemolysis levels in peripheral hemodialysis cannulas,” *Artificial Organs*, vol. 26(7), pp. 576–582, 2002.

[80] D. Lacasse, A. Garon, and D. Pelletier, “Mechanical hemolysis in blood flow: user-independent predictions with the solution of a partial differential equation,” *Computer Methods in Biomechanics and Biomedical Engineering*, vol. 10(1), pp. 1–12, 2007.

[81] J. Joshi, C. Elias, and M. Patole, “Role of hydrodynamic shear in the cultivation of animal, plant and microbial cells,” *The Chemical Engineering Journal*, vol. 62, pp. 121–141, 1996.

[82] Y. Chisti, “Hydrodynamic damage to animal cells,” *Critical Reviews in Biotechnology*, vol. 21, pp. 67–110, 2001.

[83] R. Nerem, *Structure and Function of the Circulation 2*, ch. Arterial fluid dynamics and interactions with vessel walls. Plenum Press, NY, USA, 1981.

[84] M. Sharp and F. Mohammad, “Scaling of hemolysis in needles and catheters,” *Annals of Biomedical Engineering*, vol. 26, pp. 788–797, 1998.

[85] A. Garon and M. Farinas, “Fast three-dimensional numerical hemolysis approximation,” *Artificial Organs*, vol. 28(11), pp. 1016–1025, 2004.

[86] F. Salazar, L. Rojas, and J. Antaki, “Numerical study of turbulence models in the computation of blood flow in cannulas,” in *Proceedings of FEDSM2008*, (Jacksonville, FL, USA), ASME, 2008.

[87] M. Farinas, A. Garon, D. Lacasse, and D. N’dri, “Asymptotically consistent numerical approximation of hemolysis,” *Transactions of ASME*, vol. 128, pp. 688–696, 2006.

[88] L. Goubergrits and K. Affeld, “Numerical estimation of blood damage in artificial organs,” *Artificial Organs*, vol. 28(5), pp. 499–507, 2004.

[89] A. Bellofiore and N. Quinlan, “High-resolution measurement of the unsteady velocity field to evaluate blood damage induced by a mechanical heart valve,” *Annals of Biomedical Engineering*, vol. 39(9), pp. 2417–2429, 2011.

[90] M. Nobili, J. Sheriff, U. Morbiducci, A. Redaelli, and D. Bluestein, “Platelet activation due to hemodynamic shear stresses: damage accumulation model and comparison to in vitro measurements,” *ASAIO Journal*, vol. 54(1), pp. 64–72, 2008.

[91] L. Gu and W. Smith, “Evaluation of computational models for hemolysis estimation,” *ASAIO Journal*, vol. 51, pp. 202–207, 2005.

[92] Y. Chen and M. Sharp, “A strain-based flow-induced hemolysis prediction model calibrated by in vitro erythrocyte deformation measurements,” *Artificial Organs*, vol. 35(2), pp. 145–156, 2010.

[93] Y. Chen and T. K. M. Sharp, “Testing of models of flow-induced hemolysis in blood flow through hypodermic needles,” *Artificial Organs*, vol. 37(2), pp. 256–266, 2013.

[94] P. Hariharan, M. Giarra, V. Reddy, S. Day, K. Manning, S. Deutsch, S. Stewart, M. Berman, G. Burgreen, E. Paterson, and R. Malinauskas, “Multi-laboratory particle image velocimetry analysis of the FDA benchmark nozzle model to support validation of computational fluid dynamics simulations,” *Journal of Biomechanical Engineering*, vol. 133, 2011.

[95] G. Janiga, “Large-eddy simulation of the FDA benchmark nozzle for a Reynolds number of 6500,” *Computers in Biology and Medicine*, vol. 47, pp. 113–119, 2014.

[96] S. Sandy, H. Prasanna, M. Matthew, B. Michael, and M. Richard, “Turbulence modeling as a source of error in FDA’s ”Critical Path” interlaboratory computational study of flow in a nozzle model,” tech. rep., Food & Drug Administration, Rockville MD, USA, 2010.

[97] ANSYS Co. Ltd, *Fluent Theory Guide 14.0*, Oct, 2012.

[98] “Encyclopaedia britannica.” http://www.britannica.com/EBchecked/topic/46117/axial-flow-centrifugal-pump.

[99] M. Volk, *Pump Characteristics and Applications, 2nd edition.* Taylor and Francis Group, 2005.

[100] P. Epple, F. Durst, and A. Delgado, “A theoretical derivation of the Cordier diagram for turbomachines,” *Journal of Mechanical Engineering Science IMechE*, vol. 225, pp. 354–368, 2011.

[101] 查森, 叶片泵原理及水里设计. 江苏工学院出版社, 1987.

[102] H. Schulz, *Die Pumpen.* Springer-Verlag, 1977.

[103] M. Behbahani, M. Behr, M. Hormes, U. Steinseifer, D. Arora, O. Coronado, and M. Pasquali, “A review of computational fluid dynamics analysis of blood pumps,” *European Journal of Applied Mathematics*, vol. 20, pp. 363–397, 2009.

[104] H. Yu, “Numerical investigation of a rotating system using OpenFOAM,” Master Thesis, ”Otto von Guericke” University of Magdeburg, LSS-M02/09, 2009.

[105] M. Taskin, T. Zhang, B. Gellman, A. Fleischli, K. Dasse, B. Griffith, and Z. Wu, “Computational characterization of flow and hemolytic performance of the ultramag blood pump for circulatory support,” *Artificial Organs*, vol. 34(12), pp. 1099–1113, 2010.

[106] K. Fraser, M. Taskin, B. Griffith, and Z. Wu, “The use of computational fluid dynamics in the development of ventricular assist devices,” *Medical Engineering and Physics*, vol. 33, pp. 263–280, 2011.

[107] X. Song, A. Throckmorton, H. Wood, P. Allaire, and D. Olsen, "Transient and qasisteady computational fluid dynamics study of a left ventricular assist device," *ASAIO Journal*, vol. 50, pp. 410–417, 2004.

[108] G. Burgreen, J. Antaki, Z. Wu, and A. Holmes, "Computational fluid dynamics as a development tool for rotary blood pump," *Artificial Organs*, vol. 25(5), pp. 336–340, 2001.

[109] S. Kim, Y. Choi, and K. Lee, "Design optimization of mixed-flow pump impellers and diffusers in a fixed meridional shape," in *The 10th Asian International Conference on Fluid Machinery*, NY, USA, 2010.

[110] J. Kim, K. Oh, K. Pyun, C. Kim, Y. Choi, and J. Yoon, "Design optimization of a centrifugal pump impeller and volute using computational fluid dynamics," in *26th IAHR Symposium on Hydraulic Machinery and Systems*, IOP Publishing, 2012.

[111] Y. Miyazoe, T. Sawairi, K. Ito, Y. Konishi, T. Yamane, M. Nishida, T. Masuzawa, K. Takiura, and Y. Taenaka, "Computational fluid dynamic analyses to establish design process of centrifugal blood pump," *Artificial Organs*, vol. 22(5), pp. 381–385, 1998.

[112] G. Burgreen and O. Baysal, "Three-dimensional aerodynamic shape optimization using discrete sensitivity analysis," *AIAA Journal*, vol. 34(9), p. 1770, 1996.

[113] K. Singh, J. Newman, and O. Baysal, "Dynamic unstructured method for flows past multiple objects in relative motion," *AIAA Journal*, vol. 33(4), pp. 641–649, 1995.

[114] G. Burgreen, J. Antaki, and K. Butler, "CFD-based design optimization of the outlet stator of a rotodynamic cardiac assist device," *AIAA Journal*, pp. 818–824, 1998.

[115] L. Zhu, X. Zhang, and Z. Yao, "Shape optimization of the diffuser blade of an axial blood pump by computational fluid dynamics," *Artificial Organs*, vol. 34(3), pp. 185–192, 2010.

[116] S. Derakhshan, M. Pourmahdavi, E. Abdolahnejad, A. Reihani, and A. Ojaghi, "Numerical shape optimization of a centrifugal pump impeller using artificial bee colony algorithm," *Computers and Fluids*, vol. 81, pp. 145–151, 2013.

[117] J. F. Gülich, *Kreiselpumpen.* Springer, 2004.

[118] L. Daróczy, G. Janiga, and D. Thévenin, "Systematic analysis of the heat exchanger arrangement problem using multi-objective genetic optimization," *Energy*, vol. 65, pp. 364–373, 2014.

[119] M. Mohamed, G. Janiga, E. Pap, and D. Thévenin, "Optimization of Savonius turbines using an obstacle shielding the returning blade," *Renewable Energy*, vol. 35, pp. 1512–1513, 2010.

[120] M. Mohamed, G. Janiga, E. Pap, and D. Thévenin, "Multi-objective optimization of the airfoil shape of Wells turbine used for wave energy conversion," *Energy*, vol. 36(1), pp. 438–446, 2011.

[121] J. Meyer, L. Daróczy, and D. Thévenin, "Optimizing the external geometry of a pickup tube for a Pitot-tube-jet pump," in *4th International Conference on Engineering Optimization*, (Lisbon), 2014.

[122] K. Yahyazade, "Numerical simulation of turbulent flows in nozzle and in rotating configurations using the open-source software OpenFOAM," Master Thesis, "Otto von Guericke" University of Magdeburg, LSS-M02/12, 2013.

[123] G. Blech, "Tesla pumps for blood flows," Studienarbeit, "Otto von Guericke" University of Magdeburg, LSS-S05/10, 2011.

[124] B. Yan, "Suitability of Tesla pumps for blood flows," Master Thesis, "Otto von Guericke" University of Magdeburg, LSS-M01/12, 2013.

[125] M. Köhler, *Die Strömung durch das Spaltelement einer Reibungspumpe.* Dissertation, TU Karlsruhe, 1969.

[126] M. Crawford and W. Rice, "Calculated design data for the multiple-disk pump using incompressible fluid," *Trans. ASME*, pp. 274–282, 1974.

[127] "Mathematical engineering - Luft und Raumfahrttechnik," 2014. http://me-lrt.de/warme-stoff-transport-grenzschichten-temperature-geschwindigkeit.

[128] M. Breiter and K. Pohlhausen, *Laminar flow between two parallel rotating disks.* Aeronautical Research Laboratory, Office of Aerospace Research U.S.A.F., Wright-Patterson Air Force Base, Ohio, 1962.

[129] A. Ladino, "Numerical simulation of the flow field in a friction-type turbine," Master Thesis, Technische Universität Wien, 2004.

[130] D. Nendl, "Eine theoretische Betrachtung der Tesla-Reibungspumpe," *VDI Forschungsheft*, vol. 527, pp. S.29–36, 1973.

APPENDIX A

Flow Field Contours Required by FDA for Blood Nozzle (see Section 3.1)

Figures A.1 to A.5 show contours of velocity magnitude.

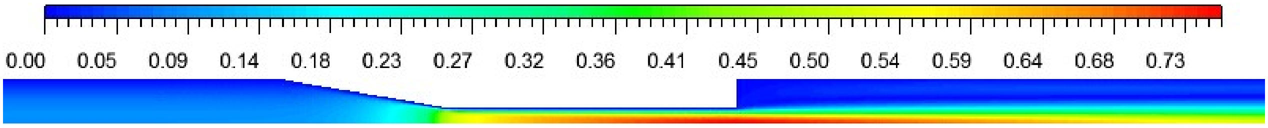

Figure A.1: Velocity magnitude for Re=500, Reynolds Stress Model, Stress-ω

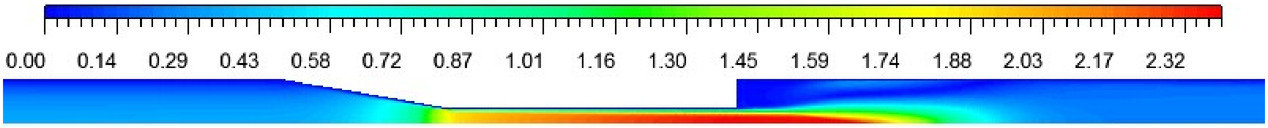

Figure A.2: Velocity magnitude for Re=2000, Reynolds Stress model, Quadratic-Pressure-Strain

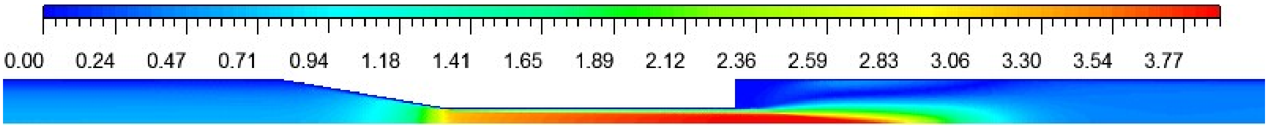

Figure A.3: Velocity magnitude for Re=3500, Reynolds Stress model, Quadratic-Pressure-Strain

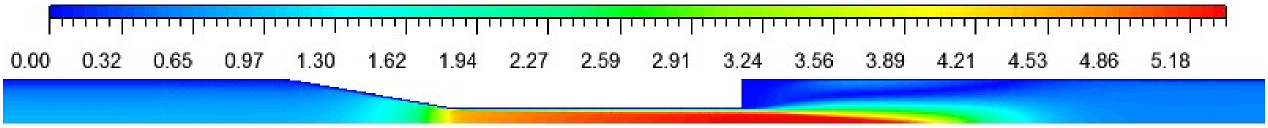

Figure A.4: Velocity magnitude for Re=5000, Reynolds Stress model, Quadratic-Pressure-Strain

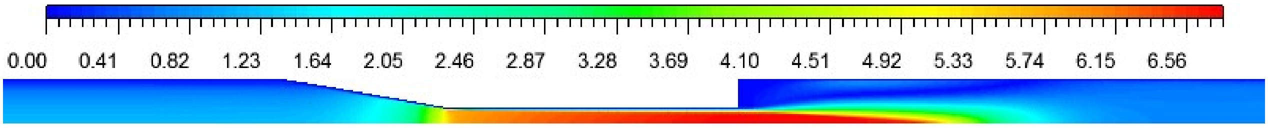

Figure A.5: Velocity magnitude for Re=6500, Reynolds Stress model, Quadratic-Pressure-Strain

Figures A.6 to A.10 show contours of turbulence kinetic energy, k.

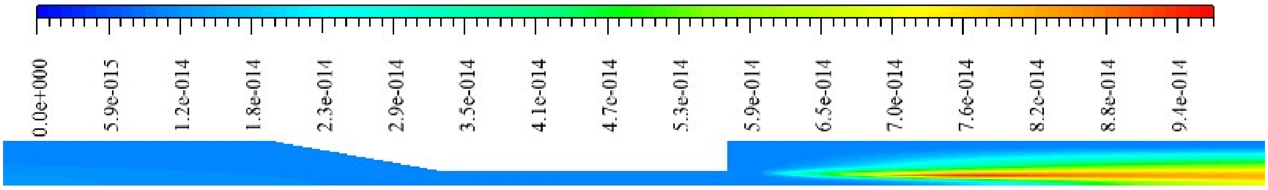

Figure A.6: Turbulence energy k for Re=500, Reynolds Stress model, Stress-ω

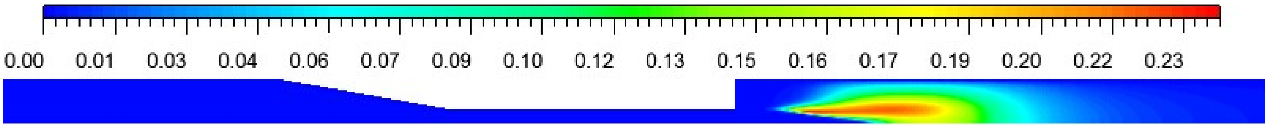

Figure A.7: Turbulence energy k for Re=2000, Reynolds Stress model, Quadratic-Pressure-Strain

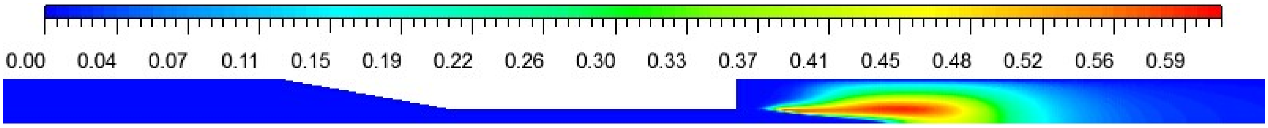

Figure A.8: Turbulence energy k for Re=3500, Reynolds Stress model, Quadratic-Pressure-Strain

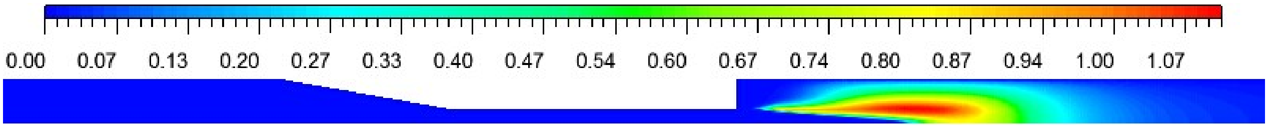

Figure A.9: Turbulence energy k for Re=5000, Reynolds Stress model, Quadratic-Pressure-Strain

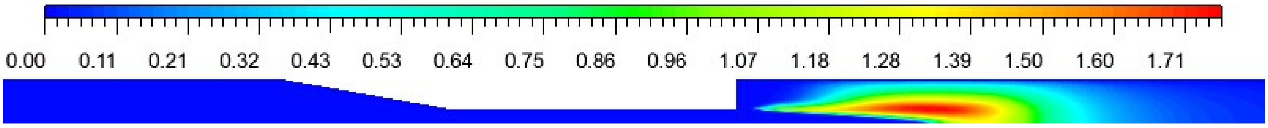

Figure A.10: Turbulence energy k for Re=6500, Reynolds Stress model, Quadratic-Pressure-Strain

Appendix B

Flow Field Contours Required by FDA for Blood Pump (see Section 3.2)

As required by the FDA, selected variable contours are also represented on following cross-sections:

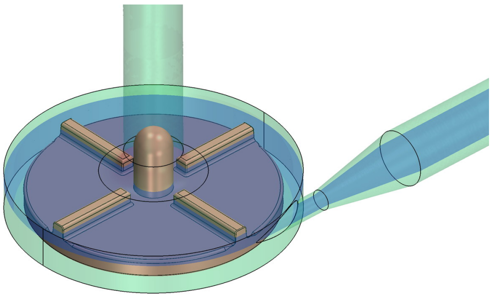

Blade passage plane

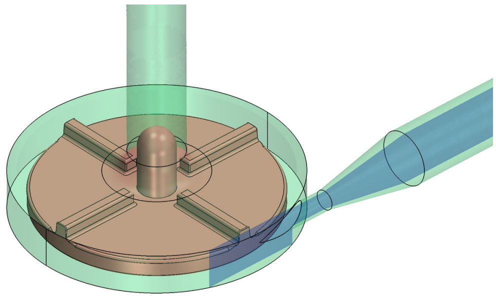

zx outlet plane

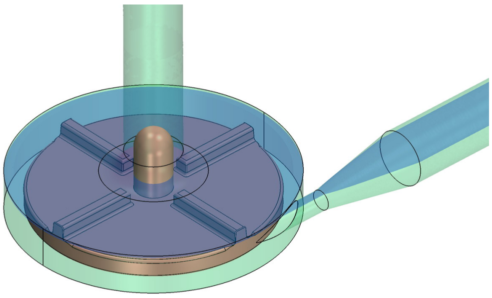

Upper gap

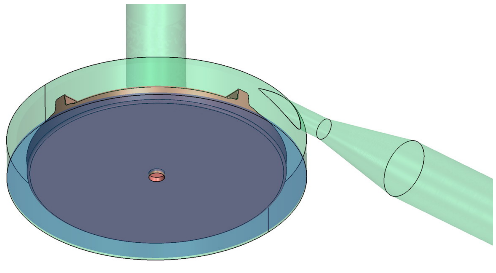

Lower gap

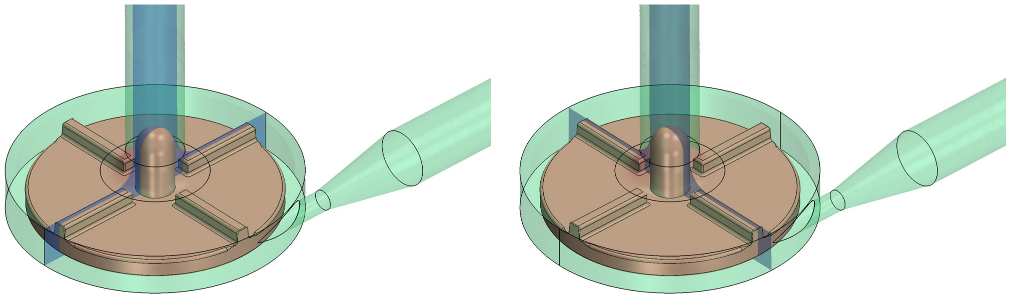

xz inlet plane

yz inlet plane

Figure B.1: FDA-defined cross-sections for plotting (see https://fdacfd.nci.nih.gov/)

Figures B.2 to B.7 are pressure contours at blade passage plane.

Figure B.2: Pressure at blade passage plane, 2.5L/min, 2500rpm

Figure B.3: Pressure at blade passage plane, 2.5L/min, 3500rpm

Figure B.4: Pressure at blade passage plane, 4.5L/min, 3500rpm

Figure B.5: Pressure at blade passage plane, 6.0L/min, 2500rpm

Figure B.6: Pressure at blade passage plane, 6.0L/min, 3500rpm

Figure B.7: Pressure at blade passage plane, 7.0L/min, 3500rpm

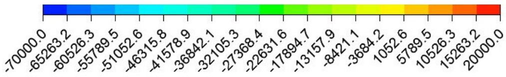

Figure B.8: Color map for Figures B.2 to B.7, Pa

Figures B.9 to B.14 show velocity contours at blade passage plane.

Figure B.9: Velocity at blade passage plane, 2.5 L/min, 2500 rpm

Figure B.10: Velocity at blade passage plane, 2.5 L/min, 3500 rpm

Figure B.11: Velocity at blade passage plane, 4.5 L/min, 3500 rpm

Figure B.12: Velocity at blade passage plane, 6.0 L/min, 2500 rpm

Figure B.13: Velocity at blade passage plane, 6.0 L/min, 3500 rpm

Figure B.14: Velocity at blade passage plane, 7.0 L/min, 3500 rpm

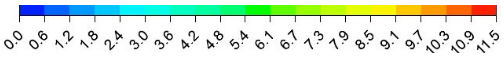

Figure B.15: Color map for Figures. B.9 to B.14, m/s

Figures B.16 to B.21 show eddy viscosity contours at blade passage plane.

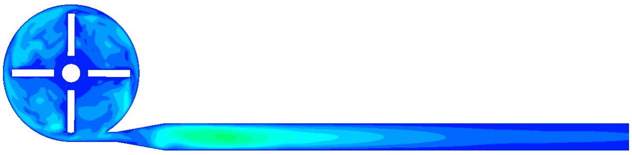

Figure B.16: Eddy viscosity at blade passage plane, 2.5 L/min, 2500 rpm

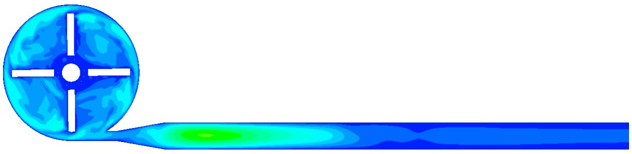

Figure B.17: Eddy viscosity at blade passage plane, 2.5 L/min, 3500 rpm

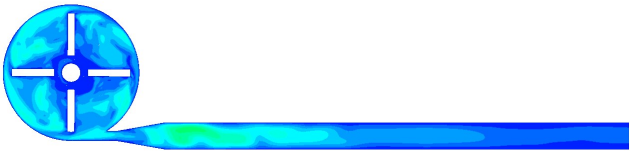

Figure B.18: Eddy viscosity at blade passage plane, 4.5 L/min, 3500 rpm

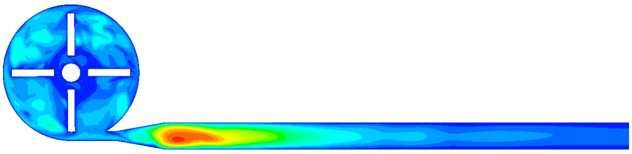

Figure B.19: Eddy viscosity at blade passage plane, 6.0 L/min, 2500 rpm

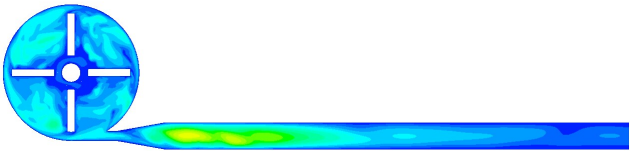

Figure B.20: Eddy viscosity at blade passage plane, 6.0 L/min, 3500 rpm

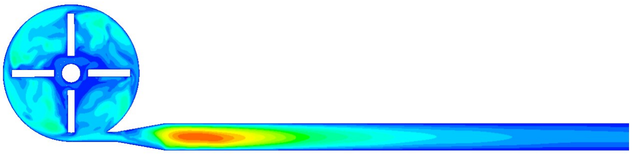

Figure B.21: Eddy viscosity at blade passage plane, 7.0 L/min, 3500 rpm

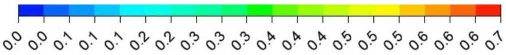

Figure B.22: Color map for Figures B.16 to B.21, in Pa.s

Figures B.23 to B.28 show pressure contours at zx-outlet plane.

Figure B.23: Pressure at zx outlet plane, 2.5 L/min, 2500 rpm

Figure B.24: Pressure at zx outlet plane, 2.5 L/min, 3500 rpm

Figure B.25: Pressure at zx outlet plane, 4.5 L/min, 3500 rpm

Figure B.26: Pressure at zx outlet plane, 6.0 L/min, 2500 rpm

Figure B.27: Pressure at zx outlet plane, 6.0 L/min, 3500 rpm

Figure B.28: Pressure at zx outlet plane, 7.0 L/min, 3500 rpm

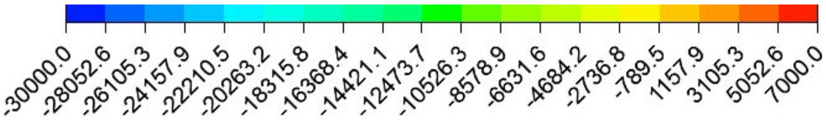

Figure B.29: Color map for Figures B.23 to B.28, Pa

Figures B.30 to B.35 show velocity contours at *zx* outlet plane.

Figure B.30: Velocity at *zx* outlet plane, 2.5 L/min, 2500 rpm

Figure B.31: Velocity at *zx* outlet plane, 2.5 L/min, 3500 rpm

Figure B.32: Velocity at *zx* outlet plane, 4.5 L/min, 3500 rpm

Figure B.33: Velocity at *zx* outlet plane, 6.0 L/min, 2500 rpm

Figure B.34: Velocity at *zx* outlet plane, 6.0 L/min, 3500 rpm

Figure B.35: Velocity at *zx* outlet plane, 7.0 L/min, 3500 rpm

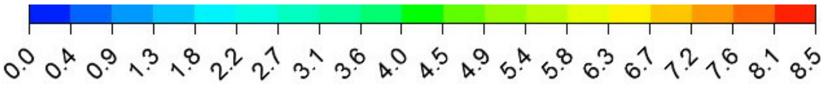

Figure B.36: Color map for Figures B.30 to B.35, m/s

Figures B.37 to B.42 show eddy viscosity contours at *zx* outlet plane.

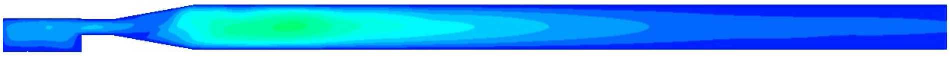

Figure B.37: Eddy viscosity at *zx* outlet plane, 2.5 L/min, 2500 rpm

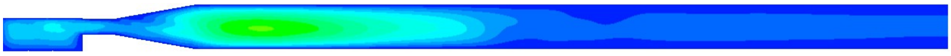

Figure B.38: Eddy viscosity at *zx* outlet plane, 2.5 L/min, 3500 rpm

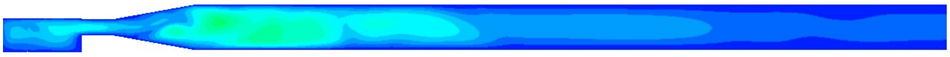

Figure B.39: Eddy viscosity at *zx* outlet plane, 4.5 L/min, 3500 rpm

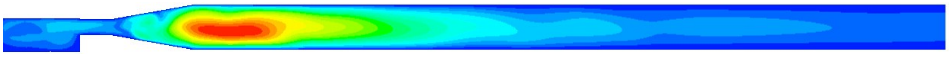

Figure B.40: Eddy viscosity at *zx* outlet plane, 6.0 L/min, 2500 rpm

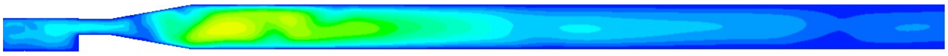

Figure B.41: Eddy viscosity at *zx* outlet plane, 6.0 L/min, 3500 rpm

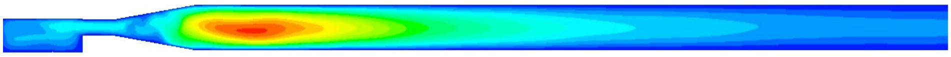

Figure B.42: Eddy viscosity at *zx* outlet plane, 7.0 L/min, 3500 rpm

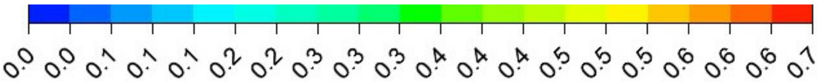

Figure B.43: Color map for Figures B.37 to B.42, Pa.s

Figures B.44 to B.55 show selected contours for the flow conditions of 6 L/min and 3500 rpm:

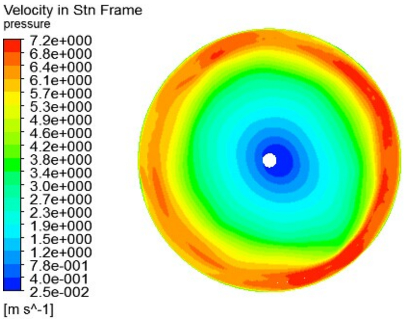

Figure B.44: Velocity at 6 L/min and 3500 rpm, lower gap

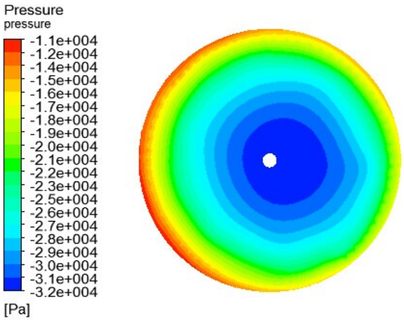

Figure B.45: Pressure at 6 L/min and 3500 rpm, lower gap

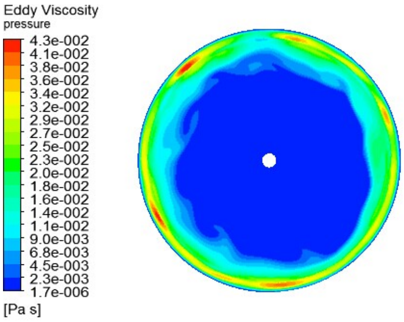

Figure B.46: Eddy viscosity at 6 L/min and 3500 rpm, lower gap

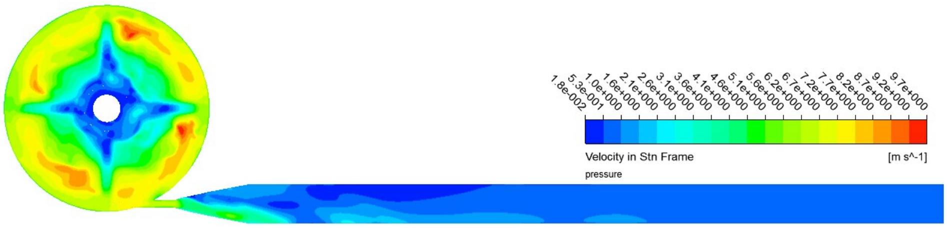

Figure B.47: Velocity at 6 L/min and 3500 rpm, upper gap

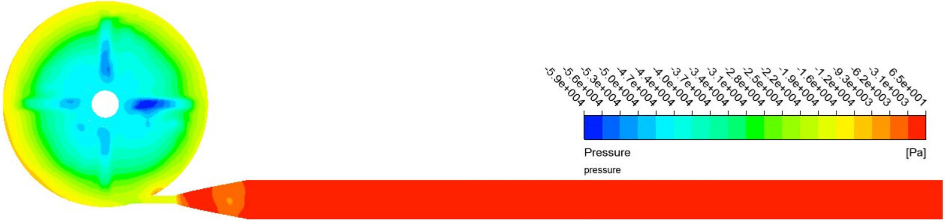

Figure B.48: Pressure at 6 L/min and 3500 rpm, upper gap

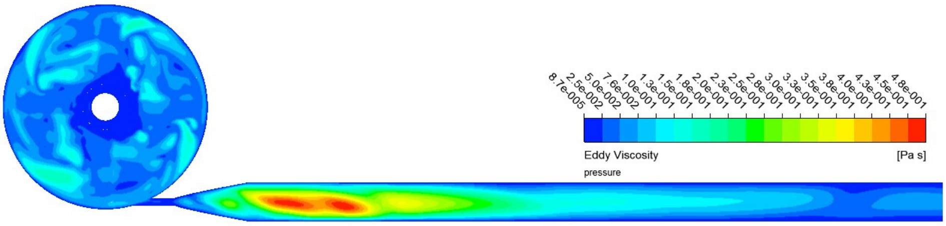

Figure B.49: Eddy viscosity at 6 L/min and 3500 rpm, upper gap

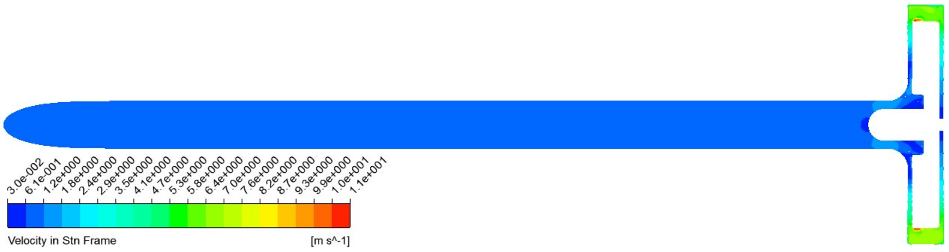

Figure B.50: Velocity at 6 L/min and 3500 rpm, yz inlet plane

Figure B.51: Pressure at 6 L/min and 3500 rpm, yz inlet plane

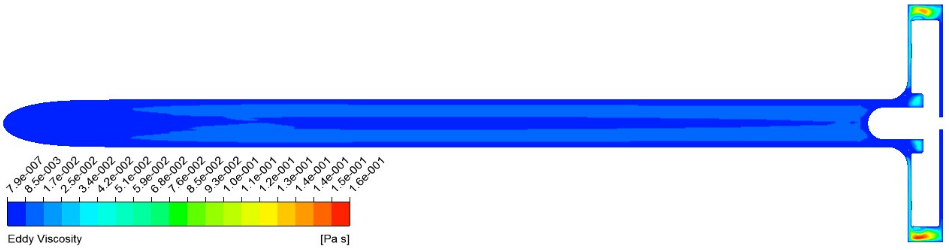

Figure B.52: Eddy viscosity at 6 L/min and 3500 rpm, yz inlet plane

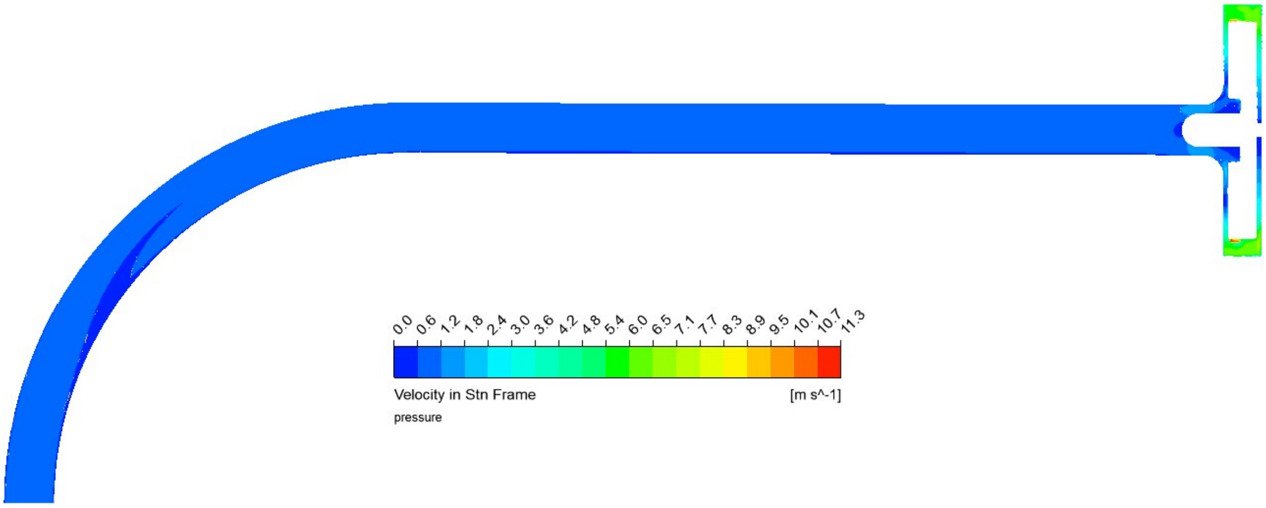

Figure B.53: Velocity at 6 L/min and 3500 rpm, zx inlet plane

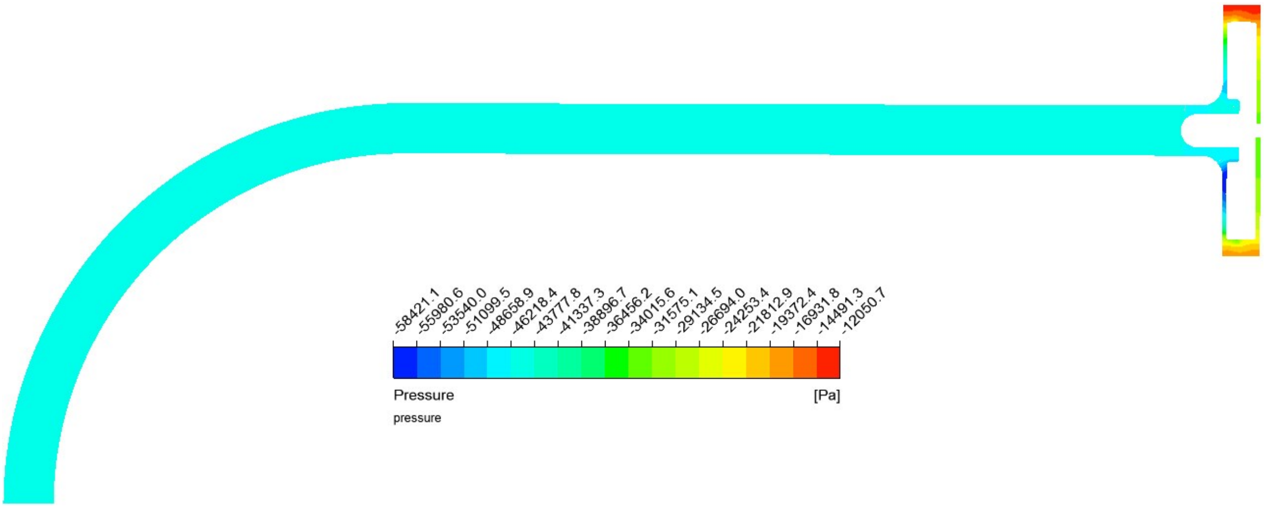

Figure B.54: Pressure at 6 L/min and 3500 rpm, zx inlet plane

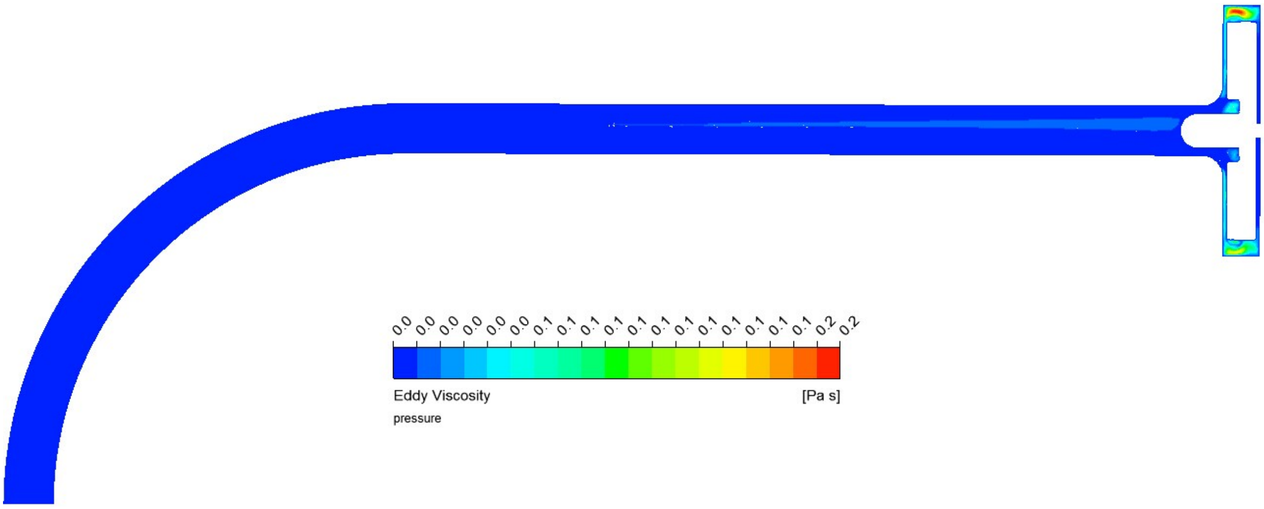

Figure B.55: Eddy viscosity at 6 L/min and 3500 rpm, zx inlet plane

Appendix C

Matlab Code for Pump Design Theory of a Screw-type Axial-flow Pump

```
clear all;
cA =0; % axial velocity
z=2; % axial length of rotor
phi1=0.9;  % squeeze coefficient at blade beginning
beta0=20*pi/180; % average inlet blade angle
dD=0.8; %shaft/shell diameter ratio
D0=0; % equivalent inlet diameter
D=0; %shell diameter
d=0;  %shaft diameter
u1n=0; %peripheral velocity at shaft
u1x=0; %peripheral velocity at blade top
beta1x=0; %blade angle at blade top
beta1n=0; %blade angle at shaft
delta=0.001; %thickness of blade
eta=0.001; % tip clearance
u2x=0; %peripheral velocity at shaft
u2n=0;%peripheral velocity at shaft
phi2=0.85; % squeeze coefficient at blade axial end
c2=5; % axial velocity at blade axial end
alpha2=40*pi/180; % average flow angle at blade axial end
Y=13.3; %pressure head
beta2=0; %average blade angle at blade axial end
Q=0.0000833; %flow rate
Nq=110; %specific speed
Nqy=3*Nq/1000;
n=Nqy*Y^0.75/Q^0.5; %rotating speed
Duration=0; % simulation duration
timeStep=0;
beta11x=0; %blade angle at blade top 1/4 axial position
beta12x=0; %2/4
beta13x=0; %3/4
beta11n=0; %blade angle at shaft 1/4 axial position
beta12n=0; %2/4
beta13n=0; %3/4
```

```
alpham1x=0; %blade angle at end of front guide vane
alpham1n=0; %blade angle at end of front guide vane

% solving at rotor inlet, equations see chapter 3
for ii=1:1000
    cA=(4*pi*(tan(beta0))^2*phi1*Q*n^2/(1-dD^2))^0.3333;
    D0=(4*Q/pi/cA)^0.5;
    D=D0/(1-dD^2)^0.5;
    d=dD*D;
    u1n=pi*n*d;
    u1x=pi*n*D;
    phi=1-z*delta/sin(beta0)/pi/((D^2+d^2)/2)^0.5;
    if abs(phi-phi1)<0.0001
        break;
    end
    phi1=phi;
end

    beta1x=atan(tan(pi/2-beta0)*D/((D^2+d^2)/2)^0.5);
    beta1n=atan(tan(pi/2-beta0)*d/((D^2+d^2)/2)^0.5);

c0=cA*phi1;
uM=((u1n^2+u1x^2)/2)^0.5; %medium peripheral velocity

%solving at rotor outlet, equations see chapter 3
for ii=1:1000
     c2=Y/eta/cos(alpha2)*2/uM;
     alpha2=asin(c0/phi2/c2);
     phi=1-2*z*delta/pi/(d+D)/sin(alpha2);
     if abs(phi-phi2)<0.0001
        break;
     end
    phi2=phi;
end
%beta2 at middle spanwise position
beta2=atan(c0/phi2/(uM-c2*cos(alpha2)));

beta0=pi/2-beta0; % beta0 is beta1
beta2=pi/2-beta2;

%calc beta2x-2n from middle spanwise position
beta2n=atan(d/(((D^2+d^2)/2)^0.5)*tan(beta2));
beta2x=atan(D/(((D^2+d^2)/2)^0.5)*tan(beta2));
%linear interpolation for 3 axial positions
beta11x=atan(tan(beta1x)+(tan(beta2x)-tan(beta1x))*0.25);
beta12x=atan(tan(beta1x)+(tan(beta2x)-tan(beta1x))*0.5);
beta13x=atan(tan(beta1x)+(tan(beta2x)-tan(beta1x))*0.75);
beta11n=atan(tan(beta1n)+(tan(beta2n)-tan(beta1n))*0.25);
beta12n=atan(tan(beta1n)+(tan(beta2n)-tan(beta1n))*0.5);
```

```
beta13n=atan(tan(beta1n)+(tan(beta2n)-tan(beta1n))*0.75);

alpha4x=-atan(tan(alpha2)*D/((D^2+d^2)/2)^0.5*AO)*180/pi;
alpha4n=-atan(tan(alpha2)*d/((D^2+d^2)/2)^0.5*AO)*180/pi;
%alpha minus 1
alpham1x=-atan(tan(pi/2-beta0)*D/((D^2+d^2)/2)^0.5*AI)*180/pi;
alpham1n=-atan(tan(pi/2-beta0)*d/((D^2+d^2)/2)^0.5*AI)*180/pi;

% radian to angle
beta2x=beta2x*180/pi;
beta2n=beta2n*180/pi;
beta1x=beta1x*180/pi;
beta1n=beta1n*180/pi;
beta11x=beta11x*180/pi;
beta11n=beta11n*180/pi;
beta12x=beta12x*180/pi;
beta12n=beta12n*180/pi;
beta13x=beta13x*180/pi;
beta13n=beta13n*180/pi;

D=D/2; % change to radius for further calculation
d=d/2;
timeStep=1/n/60; % solver time step size in s
Duration=timeStep*540; % total simulation time
n=n*2*pi; % change rotating speed to angle for modeFrontier
```

Appendix D

UDF Code for Hemolysis models in Fluent

```
#include "udf.h"
//source for the "dose"
DEFINE_SOURCE(D_source, c, t, dS, eqn)
{
        real source;
//tau_x_x
        C_UDMI(c,t,0) = 0.0035 *  C_U_G(c,t)[0];
//tau_x_y
        C_UDMI(c,t,1) = 0.0035 * C_U_G(c,t)[1];
//tau_y_x
        C_UDMI(c,t,2) = 0.0035 * C_V_G(c,t)[0];
//tau_y_y
        C_UDMI(c,t,3) = 0.0035 *  C_V_G(c,t)[1];

//shear stress scalar,equation see chapter 2
        C_UDMI(c,t,4) = pow( 0.1667* (pow(C_UDMI(c,t,0),2.0)
                +pow(C_UDMI(c,t,3),2.0))-0.3333*C_UDMI(c,t,0)
                *C_UDMI(c,t,3)+(pow(C_UDMI(c,t,1),2.0)
                +pow(C_UDMI(c,t,2),2.0)), 0.5);
//source term
        source = ABS(pow(C_UDMI(c,t,4),4.0));
        dS[eqn] = 0;
        return source;
}

//source for deltaHb/Hb,equation see chapter 2
DEFINE_SOURCE(HL_source, c, t, dS, eqn)
{
        real source;

        source = (3.31e-7) * 1/pow(ABS(C_UDSI(c,t,0)),0.23)
                 * pow(C_UDMI(c,t,4),4.0) ;
        dS[eqn] = 0;
        return source;}
```

APPENDIX E

User's Fortran Code for Hemolysis models in CFX

```
#include "cfx5ext.h"
! source for the "dose"
dllexport(user_source)
! system variables, no change
      SUBROUTINE USER_SOURCE (
     & NLOC,NRET,NARG,RET,ARGS,CRESLT,CZ,DZ,IZ,LZ,RZ)

      INTEGER NLOC,NRET,NARG
      CHARACTER CRESLT*(*)
      REAL RET(NLOC,NRET), ARGS(NLOC,NARG)
      INTEGER IZ(*)
      CHARACTER CZ(*)*(1)
      DOUBLE PRECISION DZ(*)
      LOGICAL LZ(*)
      REAL RZ(*)

      INTEGER LENACT
      EXTERNAL LENACT

!one variable need value from the system
#include "stack_point.h"
       __stack_point__ pGRAD_V !pointer to gradient of velocity
!get velocity gradient, WW is the name of the domain
      CALL USER_GETVAR ('WW.Velocity.Gradient', CRESLT, pGRAD_V,
     & CZ,DZ,IZ,LZ,RZ)
! call the subfunction
      CALL USER_SOURCE_CAL (RET(1,1), RZ(pGRAD_V), NLOC)
!end of the run
      END
!individually defined subfunction, with 1 input variable: grad_v
      SUBROUTINE USER_SOURCE_CAL (SOURCE, GRAD_V, NLOC)
!
      INTEGER NLOC !mesh size
      REAL GRAD_V(3,NLOC,3) ! !a 3x3 tensor for velocity gradient
```

```
      REAL SOURCE(NLOC), tau(NLOC), tau11(NLOC), tau12(NLOC),
     & tau13(NLOC), tau22(NLOC), tau23(NLOC), tau33(NLOC)
      INTEGER ILOC
! calculate shear stress
      DO ILOC = 1, NLOC
       tau11(ILOC) = 0.0035 * GRAD_V(1,ILOC,1)
       tau12(ILOC) = 0.00175 * (GRAD_V(1,ILOC,2) + GRAD_V(2,ILOC,1))
       tau13(ILOC) = 0.00175 * (GRAD_V(3,ILOC,1) + GRAD_V(3,ILOC,1))
       tau22(ILOC) = 0.0035 * GRAD_V(2,ILOC,2)
       tau23(ILOC) = 0.00175 * (GRAD_V(2,ILOC,3) + GRAD_V(3,ILOC,2))
       tau33(ILOC) = 0.0035* GRAD_V(3,ILOC,3)
       tau(ILOC) = (0.1667*(tau11(ILOC)**2 + tau22(ILOC)**2 +
     & tau33(ILOC)**2) +
     & 0.3333*(tau11(ILOC)*tau22(ILOC) + tau11(ILOC)*tau33(ILOC) +
     & tau22(ILOC)*tau33(ILOC)) + 0.3333*
     & (tau12(ILOC)**2 + tau23(ILOC)**2 + tau13(ILOC)**2))**0.5
!calculate source for the "dose"
      SOURCE(ILOC) = tau(ILOC)**4.0

      END

#include "cfx5ext.h"
dllexport(user_source2)
      SUBROUTINE USER_SOURCE (
     & NLOC,NRET,NARG,RET,ARGS,CRESLT,CZ,DZ,IZ,LZ,RZ)

      INTEGER NLOC,NRET,NARG
      CHARACTER CRESLT*(*)
      REAL RET(NLOC,NRET), ARGS(NLOC,NARG)
      INTEGER IZ(*)
      CHARACTER CZ(*)*(1)
      DOUBLE PRECISION DZ(*)
      LOGICAL LZ(*)
      REAL RZ(*)

      INTEGER LENACT
      EXTERNAL LENACT
!2 variables need value from the system
#include "stack_point.h"
       __stack_point__ pGRAD_V
       __stack_point__ p_D
!get values from system
      CALL USER_GETVAR ('WW.Velocity.Gradient', CRESLT, pGRAD_V,
     & CZ,DZ,IZ,LZ,RZ) ! velocity gradient
      CALL USER_GETVAR ('WW.HL', CRESLT, p_D,
     & CZ,DZ,IZ,LZ,RZ) ! the "dose" which is calculated from the other
!source code
!call subfunction
```

```
      CALL USER_SOURCE_CAL (RET(1,1), RZ(pGRAD_V), RZ(p_D), NLOC)

      END

!subfunction with 2 input variables
      SUBROUTINE USER_SOURCE_CAL (SOURCE, GRAD_V, D, NLOC)

      INTEGER NLOC
      REAL GRAD_V(3,NLOC,3)
      REAL D(NLOC)  ! the scalar for "dose"

      REAL SOURCE(NLOC), tau(NLOC), tau11(NLOC), tau12(NLOC),
     & tau13(NLOC), tau22(NLOC), tau23(NLOC), tau33(NLOC)
      INTEGER ILOC
 !calculate shear stress: tau
      DO ILOC = 1, NLOC
       tau11(ILOC) = 0.0035 * GRAD_V(1,ILOC,1)
       tau12(ILOC) = 0.00175 * (GRAD_V(1,ILOC,2) + GRAD_V(2,ILOC,1))
       tau13(ILOC) = 0.00175 * (GRAD_V(3,ILOC,1) + GRAD_V(3,ILOC,1))
       tau22(ILOC) = 0.0035 * GRAD_V(2,ILOC,2)
       tau23(ILOC) = 0.00175 * (GRAD_V(2,ILOC,3) + GRAD_V(3,ILOC,2))
       tau33(ILOC) = 0.0035* GRAD_V(3,ILOC,3)
       tau(ILOC) = (0.1667*(tau11(ILOC)**2 + tau22(ILOC)**2 +
     & tau33(ILOC)**2) +
     & 0.3333*(tau11(ILOC)*tau22(ILOC) + tau11(ILOC)*tau33(ILOC) +
     & tau22(ILOC)*tau33(ILOC)) + 0.3333*
     & (tau12(ILOC)**2 + tau23(ILOC)**2 + tau13(ILOC)**2))**0.5
!calculate source
      SOURCE(ILOC) =  0.000000331*D(ILOC)**(-0.23) * tau(ILOC)**4.0

      END
```